

Magnus Borstad Lilledahl

Detection of vulnerable atherosclerotic plaque

Thesis for the degree philosophiae doctor

Trondheim, January 2007

Norwegian University of Science and Technology
Faculty of Information Technology,
Mathematics and Electrical Engineering
Department of Electronics and Telecommunications

NTNU

Norwegian University of Science and Technology

Thesis for the degree philosophiae doctor

Faculty of Information Technology,
Mathematics and Electrical Engineering
Department of Electronics and Telecommunications

© Magnus Borstad Lilledahl

ISBN 978-82-471-0489-7 (printed version)
ISBN 978-82-471-0492-7 (electronic version)
ISSN 1503-8181

Doctoral theses at NTNU, 2007:23

Printed by NTNU-trykk

Preface

Perhaps the most valuable result of all education is the ability to make yourself do the thing you have to do, when it ought to be done, whether you like it or not; it is the first lesson that ought to be learned; and however early a man's training begins, it is probably the last lesson that he learns thoroughly.

Thomas H. Huxley, English biologist (1825 - 1895)

The work which comprise this thesis was done at the Norwegian University of Science and Technology in Trondheim, Norway, from January 2003 to November 2006 under the supervision of professor Lars Othar Svaasand.

As I climbed the steep hill toward the Gløshaugen campus early one morning in November 2002, I was imbued by a spirit of academia. The towers of the main building reminded me of famous classical institutions like Yale, Oxford and Johns Hopkins University: Brilliant professors in tweed jackets, libraries filled with dusty books, profound discussion in dimly lit halls and secret high-tech laboratories. Unfortunately, the feeling of grand academic architecture was vaporized as I rounded the corner of the main building and witnessed the architectural wasteland that lay behind. However, during my interview with professor, and later advisor, Lars Othar Svaasand the associations to classic academia returned. As he scratched his beard and lectured on nonlinear optical phenomena with sparkling eyes, I thought that NTNU could be a good place to study. Through countless discussions in the library (ehh...maybe coffee room is more exact) he has given me physical insights in a wide array of physical phenomena that made me realize that I knew close to nothing, but also moved me infinitely further away from the ignorance that was mine when I began the pursuit of a PhD degree.

Several people have made these four years a gratifying experience. Lise Lyngsnes Randeberg provided invaluable support on many occasions, especially during my first fumbling year when I had no signs to point me in the right direction.

The cross-disciplinary nature of this work has been very rewarding. I would like to thank all the people at St. Olav's Hospital and especially Olav Anton Haugen for providing medical insight, tissue samples and hunting advice.

Also, a great thanks to Eivind Larsen and Bertil Nistad who, through uncountable coffee breaks, have inspired a great interest in the the field of extracurricular applied physics. Andreas Winnem and the people in SMIDA must be mentioned for providing a social life where little existed before.

I have very much enjoyed working with professors Odd Gutteberg, Trond Ytterdal, Morten Olavsbråten and Helge Engan in my mandatory teaching hours, making it less of a hassle than it could be.

Thanks to all my students that have slaved for me and shown that students are still hard working and enthusiastic, just like they were in my time.

To my girlfriend Kari, family, and friends in Oslo: I could not have accomplished this without you....or yes, actually I could, but the process would probably have been all the less pleasurable.

And to everybody else I have worked with, it has been a great time, but unfortunately you did not quite make it to be mentioned in the preface :-P

Abstract

Heart attacks are the cause for the majority of deaths in the industrialized world. The underlying cause of most of these deaths is the rupture of vulnerable plaque. As of this day, no widely accepted clinical tool exists for detecting plaques that are prone to rupture, although several techniques are being investigated. This thesis gives an overview of detection modalities that have been proposed for detecting vulnerable plaque with special emphasis on three methods, diffuse reflection spectroscopy, thermography and multiphoton microscopy.

Outline of thesis

Introduction

This chapter gives an outline of the thesis and a list of the included papers. The author's contributions to the various published works are specified and a brief description of the papers is given. The papers are listed chronologically. All the papers are related to the detection and characterization of vulnerable plaques. The work has centered around several topics within this field, namely diffuse reflection spectroscopy, thermography, multiphoton spectroscopy and fluorescence spectroscopy. In addition, a list of other publications completed during the PhD period, but not related to vulnerable plaque, is included.

Outline

Chapter 2 reviews the basic physiology of atherosclerosis and the features that are relevant for vulnerable plaque detection. Then a review of technologies that are in use for characterization of cardiovascular disease is presented. Not only those modalities that measure individual plaques, but also techniques for measuring their effects, i.e. indirect measures of atherosclerosis are included. The modalities are grouped according to the level of physiological detail they measure: Systemic parameters, heart function, vessel anatomy and vessel wall anatomy. More details are included in those fields where active research has been conducted.

List of papers

- **Characterization of atherosclerotic plaque by reflection spectroscopy and thermography: A comparison**

Magnus B. Lilledahl, Olav A. Haugen, Lise L. Randeberg and Lars O. Svaasand.

Proceedings of SPIE, vol. 5686, 415-425 (2005)

Absorption spectra of pure substances likely to dominate near infrared absorption spectra in arteries were measured. These basis spectra

were used in a diffusion type model to determine the expected shape of measured spectra. Samples of human aorta were examined spectroscopically and a measure of the lipid content based on the spectra is presented. No correlation between the size of the plaques and the spectra was found.

Simple models of heat distribution in a plaque were developed to determine temperature increases in plaques due to higher metabolism. The expected temperature at the surface was found to be less than 0.05° . This value was in agreement with thermographic, in-vivo measurements performed in rabbit aortas.

Contributions: Conducting spectroscopic measurements and analysis of data with existing models. Development of lipid-index. Mathematical analysis of thermal distributions in plaque.

- **The effect of a thin bloodlayer on fluorescence spectroscopy**
Magnus B. Lilledahl, Marianne Barkost, Mari W. Gran, Olav A. Haugen and Lars O. Svaasand
Proceedings of SPIE, vol. 6078, 60782J-1 (2006)

Fluorescence from samples of human aorta were excited using a light emitting diode and the fluorescence was collected with a fiber optic probe. The level of fluorescence could detect calcifications but the differentiation between fibrous and lipid rich plaque was poor. Fluorescent tissue phantoms of fluorescein and agar with a surface layer of blood was investigated to determine the effect of the interfering blood. When a random layer of blood was added to the spectra from the aorta samples the different tissue states could no longer be determined accurately.

Contributions: Spectral measurements of aorta. Analysis of spectral data and the effect of the added blood layer.

- **Reflection spectroscopy of atherosclerotic plaque**
Magnus B. Lilledahl, Olav A. Haugen, Marianne Barkost and Lars O. Svaasand.
Journal of Biomedical Optics 11(2), 0210051-0210057 (2006)

A series of reflectance spectra were collected from human aorta with varying degrees of atherosclerosis. The spectra were collected both with an optical fiber probe and an integrating sphere. The reflected spectra were compared to histology and it was found that near infrared spectroscopy could be used to detect lipids in plaques with good sensitivity and specificity.

Contributions: Experimental work and development of method of analysis.

- **An analytic and numerical study of intravascular thermography of vulnerable plaque**

Magnus B. Lilledahl, Eivind L. P. Larsen and Lars O. Svaasand
Physics in medicine and biology.

52 (2007), 961-979

An estimate of the upper limit of heat generation that could be expected in a plaque was developed from physiological considerations. This value was used in numerical and analytic models of the heat distribution in a plaque to calculate a limit on the temperature increase that could be expected in a plaque due to inflammation. It was found that the an upper limit on the temperature due to a plaque was 0.1°C. Possible explanations for higher values reported in the literature is presented.

Contributions: Numerical analysis and analytic model development in cooperation with Lars O. Svaasand.

- **Characterization of vulnerable plaques by multiphoton microscopy**

Magnus B. Lilledahl, Olav A. Haugen, Catharina Davies and Lars O. Svaasand

Journal of Biomedical Optics **Conditionally accepted.**

Multiphoton microscopy could be used to image the connective fibers that constitute the fibrous plaque, which again could be used to determine its mechanical strength. Samples of human aorta were imaged in a microscope coupled to a Ti:Sapphire laser to excite second harmonic generation and two-photon excited fluorescence. It was found that individual collagen fibers and elastic fibers could be seen down to a depth of about 100 μm .

Contributions: Collection of microscopy images and analysis.

Other publications

This section includes publications which do not fall under the subject of this thesis and is thus not included, but was completed during the Ph.D period.

- **Subcutaneous transport of extravascular blood**

Lise L. Randeberg, Eivind L. P. Larsen, Magnus B Lilledahl, Rune Haaverstad, Olav A. Haugen, Bjorn Skallerud and Lars O. Svaasand.
Proceedings of SPIE, vol. 6078 (2006), 607808-9

Models of fluid transport in tissue was developed based on measurements of fluorescein transport in a porcine model.

Contributions: Assisted in the experimental work.

- **Skin changes following minor trauma**

Lise L. Randeberg, Andreas M. Winnem, Neil E. Langlois, Eivind L. P. Larsen, Magnus B. Lilledahl, Rune Haaverstad, Bjørn Skallerud, Olav A. Haugen and Lars O. Svaasand.

Spectroscopic and histological investigation of blunt trauma in a porcine model was investigated. It was found that reflection spectroscopy could be used to characterize age and type of trauma.

Contributions: Assisted in the experimental work.

Contents

Preface	i
Abstract	iii
Outline of thesis	viii
Table of contents	x
1 Introduction	1
1.1 Motivation	1
2 Atherosclerosis	3
2.1 Introduction	3
2.2 Normal vessel anatomy	3
2.3 Physiology of atherosclerotic lesions	4
2.3.1 Histological classification	4
2.3.2 Lesion initiation and development	7
2.4 Vulnerable plaque	8
2.5 Vulnerable patient	8
2.6 Detection features	9
2.7 Treatment	10
3 Detection modalities	11
3.1 Introduction	11
3.2 Systemic parameters	12
3.2.1 Traditional risk factors	12
3.2.2 Biomarkers	12
3.3 Heart function	13
3.3.1 Electrocardiography	13
3.3.2 Echocardiography	14
3.3.3 Nuclear imaging	15
3.4 Vessel anatomy	18
3.4.1 Coronary Angiography	18
3.4.2 Magnetic Resonance Imaging	19

3.4.3	Computed tomography	21
3.4.4	Ultrasonography	23
3.4.5	Ankle-Brachial pressure index	23
3.5	Vessel wall anatomy, composition and function	23
3.5.1	Intravascular ultrasound	23
3.5.2	Thermography	26
3.5.3	Optical coherence tomography	29
3.5.4	Multiphoton microscopy	31
3.5.5	Optical spectroscopy	34
3.5.6	Angioscopy	43
4	Conclusions	45
4.1	Conclusions	45
5	Future work	47
5.1	Future Work	47

Chapter 1

Introduction

1.1 Motivation

Only two things are infinite, the universe and human stupidity, and I'm not sure about the former.

Albert Einstein, US (German-born) physicist (1879 - 1955)

Cardiovascular disease places an enormous medical and economic burden on society, being the cause of the majority of deaths in the western world. Most of these deaths are caused by the rupture of atherosclerotic plaques in the coronary arteries. A lot is known about lifestyle habits that accelerate the development of atherosclerotic plaque, yet it seems as if the general population is unwilling to heed the advice and change their detrimental habits. Hence, the medical personnel are left with the option of treating patients after the development of the disease. It is established that the majority of acute coronary events are caused by the rupture or erosion of so-called vulnerable plaque (defined as plaques prone to causing atherothrombosis). Two thirds of all coronary deaths are caused by plaque rupture with the remaining being due to plaque erosion[60]. However, equipment for detecting these types of plaques are still in the research laboratories. This leaves us in the worrisome situation where we both know the risk factors of atherosclerotic development, and when the plaques begin to put the patient at risk, yet neither of the problems can be addressed. The first due to the lack of knowledge and will-power in the population and the second due to the lack of technology for the clinical personnel. The goal of this thesis is to provide a contribution for solving the second issue.

There are two important aspects that motivates this work. One is to develop a sensor that can detect a vulnerable plaque and indicate for the clinician the appropriate treatment. However, the treatment for vulnerable plaque is not fully developed. The other goal is to design a sensor that can characterize plaques and can be used to monitor their development to

better understand the disease process and monitor the effect of medication. Even though clinical tools in the end must rely on proven clinical effects, a better understanding of the physiological process can aid the development of appropriate treatments.

Chapter 2

Atherosclerosis

Now there are more overweight people in America than average-weight people. So overweight people are now average. Which means you've met your New Year's resolution.

Jay Leno, US talk-show host

2.1 Introduction

Atherosclerosis (from the greek *athere* -porridge, gruel and *sklerosis* - hardening) is believed to be the underlying cause for the majority of cardiovascular disease (CVD)[72]. The early stages of atherosclerosis (described below) can be seen in virtually everybody from the first decade of life. These early stages are reversible, but can, due to certain conditions, develop into a life-threatening condition. In the early stages the changes in the vessel wall occur at localized areas called *plaques*, as they are often elevated from the surrounding vessel wall. In advanced stages of the disease the whole vessel can be affected, and no normal areas can be found. The exact development of atherosclerotic plaques is still an area of active research, but numerous risk factors have been determined, e.g. high cholesterol levels, smoking, family history of CVD, high blood pressure, obesity, sedentary lifestyle, stress and many more. In the following a brief description of the disease and properties that are relevant for new detection modalities are presented.

2.2 Normal vessel anatomy

In all arteries in the body, three distinct regions can be defined. These are called the *tunica intima*, *tunica media* and *tunica adventitia* (see figure 2.1). The tunica intima consists of a continuous endothelium facing the lumen, resting on a basement membrane. The endothelium is a continuous layer of endothelial cells which serves as the signaling pathway between the vessel

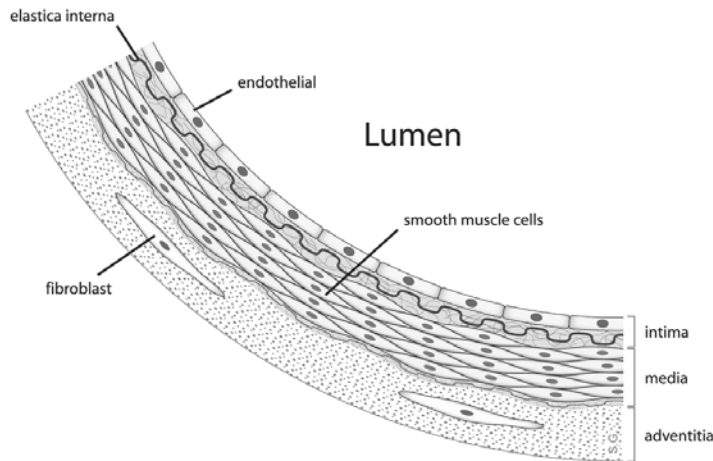


Figure 2.1: The figure shows schematically the structure of a muscular artery where the major structural features are illustrated. (Courtesy of Stijn A.I. Ghesquiere[118]).

and cytokines circulating in the blood. Under the endothelium is the subendothelium which consists of fibroelastic tissue and a few scattered muscle cells. Between the tunica intima and the tunica media is the internal elastic lamina, which is a thick layer of elastic fibers. The tunica media differs slightly in elastic arteries (the aorta and its major branches) and muscular arteries (all other arteries). In elastic arteries the tunica media consists primarily of elastic membranes separated by ground substance, while in muscular arteries the media consists of layers of muscle cells with connective tissue in between. The elastic arteries are responsible for maintaining blood pressure during diastole while muscular arteries can contract or dilate according to the oxygen demand of the tissue distal to the vessel. The outermost layer, the tunica adventitia consists of loose connective tissue, fat cells and blood vessels. The blood vessels in the adventitia are called the vasa vasorum, literally meaning the vasculature of the vessel. An external elastic lamina can sometimes be seen between the media and adventitia.

2.3 Physiology of atherosclerotic lesions

2.3.1 Histological classification

The following classification of atherosclerotic plaques is based on a series of consensus documents issued by the American Heart Association (AHA) [87, 89, 88]. The motivation for this classification was based on histological

studies that indicate that each type of plaque is temporarily or permanently stable. Refer to figure 2.2.

Type I-III lesions are often called early lesions. These lesions show no disruption of intimal structure and there is no effect on the media or adventitia. They are considered to be reversible changes.

- Type I: Initial lesion
 - Increase in number of macrophages.
 - Appearance of macrophages filled with lipid droplets.
- Type II: Fatty streak
 - Grossly visible.
 - Layers of macrophage foam cells, increased number of macrophages.
 - Lipid droplets within intimal smooth muscle cells.
 - Minimal extracellular lipids.
- Type III: Intermediate lesion
 - All of type II characteristics.
 - Pools of extracellular lipids.

Type IV-VI lesions are often called advanced lesions. These lesions show intimal disorganization and are often symptomatic. They predispose to sudden lesion progression and are not reversible.

- Type IV: Atheroma
 - Lipid core of extracellular lipid.
 - Intimal disorganization.
 - No fibrous (collagenous) cap.
- Type V: Fibrous
 - Thick layers of fibrous tissue.
 - Type Va if presence of lipid core (fibroatheroma).
 - Type Vb if calcified.
 - Type Vc if no lipid accumulation.
- Type VI: Complicated lesions.
 - Type IV or V with additional fissure (VIa), hematoma (VIb) or thrombus (VIc).

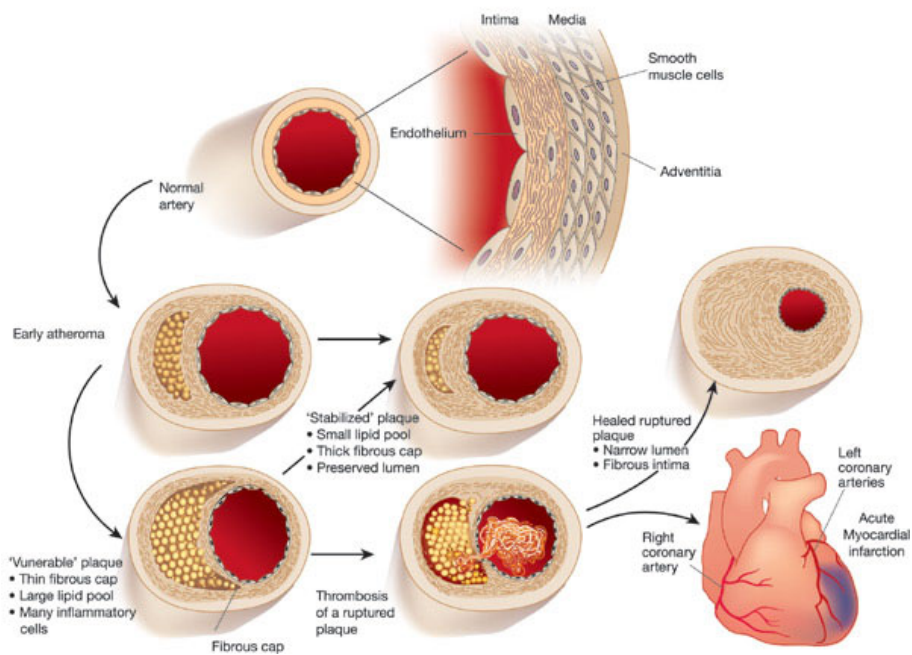


Figure 2.2: Illustration of the development of atherosclerosis within the artery. (Reprinted by permission from Macmillan Publishers Ltd: Nature[54], copyright 2002.)

Virmani et al. have published a paper suggesting some changes to this classification based on what they view as certain shortcomings[112]. First, the classification is based on postmortem histological studies, and thus the chronological progression suggested by the roman numbering is uncertain and should be avoided. Furthermore, later studies have shown that not only plaque rupture is associated with thrombosis but also plaque erosion, and, less frequently, calcified nodules. Since thromboses, erosions, rupture etc. occur over various plaque morphologies, they should not be classified as separate plaque types but rather to be used as adjectives to describe different states of the same plaque type. The plaque types proposed by this Virmani et al. was,

- Intimal thickening
- Intimal xanthoma (fatty streak)
- Pathological intimal thickening
- Fibrous cap atheroma
- Thin cap fibroatheroma
- Calcified nodule
- Fibrocalcific plaque

The first two plaque types are considered normal and reversible and are thus not atherosclerotic.

2.3.2 Lesion initiation and development

The exact process that initiates atherosclerotic plaques and cause them to develop into advanced lesions is not known in detail. The problem is that practically all information about plaques is from retrospective pathological studies.

It is believed that plaque development is initiated by lipoproteins being absorbed in the intima due to high concentrations circulating in the plasma. Plaques often appear at branches and bifurcations of the artery indicating that hemodynamics play a role. Perhaps increased turbulence and reduced shear stress increase the likelihood of molecules adsorbing to the endothelium. A small damage to the endothelium has also been proposed as the starting point for atherosclerotic plaques. The absorbed lipids are oxidized in the plaque which triggers an immune response that recruits monocytes. Atherosclerosis is therefore characterized as an inflammatory disease. The monocytes digest the lipids and turn into macrophages. The process which then makes the plaque develop into an advanced lesion instead of regressing is not known, but it is believed to be a complicated process with many mediators being involved[65].

2.4 Vulnerable plaque

The definition of vulnerable plaque is a functional one and not based on anatomic appearance. This is due to the fact that many types of plaques can cause obstructive thrombosis in the coronary arteries, and as of yet there exists very few prospective studies that have determined which plaques are most likely to develop thrombosis. Therefore the title of this thesis could perhaps have been *determining* the vulnerable plaque rather than *detecting*. The first task of new detection modalities that are being developed (described in chapter 3) is to prospectively determine what actually characterizes a vulnerable plaque. Only when this information has been confirmed can the development of the ideal detection technique begin.

A vulnerable plaque is therefore defined as a plaque at increased risk of thrombosis and lesion progression[113]. Retrospective studies have shown that ruptured plaques seem to be the cause of most thrombi, though also intimal erosions also cause thrombosis[34]. These studies have indicated that most ruptured plaques are so called thin-cap fibroatheromas with macrophage infiltration. These types of plaques would be classified as a type IV or V in the AHA classification. Other types of plaques that have been associated with thrombosis is proteoglycan rich plaques and plaques with calcified nodules[72]. Mauriallo et al. found that inflammation is increased four-fold (by counting inflammatory cells in histological sections) in patients having suffered a myocardial infarction, compared to controls[63], and that inflammation was also present in stable plaques and non-culprit coronary segments. Vulnerable plaques were found to only have a 30% increased in inflammatory cells compared to stable plaques. This study thus indicates that the role of inflammation in atherosclerosis is primarily systemic.

One prospective study with angiography has shown that glistening yellow plaques have an increased risk of developing thrombosis[75]. This yellow color could be due to lipophilic carotenoids being absorbed in lipid rich plaques[8]. The plaques were hypothesized to be thin-cap fibroatheromas.

A reason for the lack of prospective studies has been limitations in available imaging techniques for individual plaques. With the advent of the modalities described herein, this obstacle will now be cleared. The information that is most relevant clinically has yet to be determined and must also be seen in light of cost, time, and available treatment.

2.5 Vulnerable patient

Vulnerable patient is a term coined for patients that are at increased risk of experiencing an acute coronary event[72]. Vulnerable patients are defined not only by the presence of vulnerable plaques, but also blood that is prone to thrombosis (vulnerable blood) and a myocardium that is prone to fatal

arrhythmias (vulnerable myocardium). Diabetes is one condition that can lead to vulnerable blood, and many other serum markers have also been associated with a thrombosis prone blood[72]. A vulnerable myocardium can be caused by ventricular hypertrophy and electrical instabilities in the heart.

2.6 Detection features

It has been shown that the majority of plaques that cause acute coronary events are not hemodynamically significant and are not visible during angiography. This does not, however, mean that the plaques are small but rather that they exhibit positive remodeling (i.e. not stenotic)[38]. This has been shown both by histological and intravascular studies[36]. Stenotic plaques also cause acute events but are often symptomatic (angina) before the occurrence of a myocardial infarction. Some also included plaques with greater than 90% stenosis as vulnerable[72], the present work will however use the definition of a plaque prone to thrombosis by plaque rupture or erosion. The important features that is believed to characterize vulnerable plaques are: A large lipid core, a thin fibrous cap covering the lipid core, and the presence of macrophages. One study reported that 95% of ruptured plaques had a cap thickness less than $64 \mu\text{m}$ (mean $23 \mu\text{m}$) and therefore put $65 \mu\text{m}$ as a limit of vulnerability[16]. Further prospective studies are needed to confirm these findings and this is now possible with the new image modalities described herein.

Another important feature of atherosclerosis is that it is a diffuse disease that affects the entire arterial tree. Burke et al. reported 1.22 ± 1.44 additional vulnerable plaques in men who died suddenly of coronary disease[16]. This raises the important issue of whether it is helpful to find individual atherosclerotic plaques since there are several of them. Treating all of them individually might not be a cost effective solution. It might be better to assess the global burden of the disease and then use systemic medication. The global extent of atherosclerosis can be determined noninvasively by imaging larger and more accessible arteries than the coronary arteries.

As opposed some forms of cancer (cervical and breast), there exists no current screening for cardiovascular disease, even though the latter is the cause of more deaths. The SHAPE report calls for screening for atherosclerosis beyond traditional risk factor assessment like the Framingham risk (see section 3.2.2)[71]. They propose that the traditional assessments are expanded for selected moderate risk patients, with noninvasive assessments of coronary calcium score by computed tomography (section 3.4.3) or measurement of carotid intima-media thickness by ultrasonography (section 3.4.4).

2.7 Treatment

The treatments that are proposed for vulnerable plaques are mainly lifestyle changes and pharmacological medication e.g. statins, lipid-lowering drugs, anti-thrombotic medication, beta-blockers, nitrates and hypertensive-drugs. Treatment will depend on risk assessment and age. At increasing age long term side effects are not so important, but the body might respond poorly to strong medication. Since medications are mostly systemic, the question again arises of whether characterization of individual plaques in coronary arteries is valuable. Perhaps a general plaque burden can be assessed from more easily accessible vessels?

With high throughput genomic and proteomic studies with micro arrays the actual expressions of mRNA and proteins in plaques can be determined. This might lead to drugs that more directly interfere with the processes that cause plaques to develop.

Stenting has been proposed as focal treatment of plaques. However, it has been shown that if there is one vulnerable plaque there are usually more. Drug-eluting stens have been very successful in avoiding restenosis problems. Whether stenting of several non-stenotic plaques due to risk of plaque rupture is clinically favorable is uncertain and must be investigated. It is also uncertain to what degree the stenting will make the plaques less prone to thrombosis. It might reduce the risk of rupture, but as already mentioned endothelial erosion can also cause thrombosis and it is not clear what effect stenting would have on this process.

Chapter 3

Detection modalities

3.1 Introduction

This chapter organizes detection modalities of atherosclerosis according to the level of spatial physiological detail they deliver. The parameter measured can be systemic, that is, a property of the whole body. By zooming in, usually including imaging, the modality can look at the function of the myocardium, trying to determine whether it is affected by atherosclerosis or if a myocardial infarction has already occurred. By including even more detail the function of the arteries themselves can be assessed, which usually amounts to determining the anatomy of the lumen. This is usually done with an imaging modality but indirect methods also exist (e.g. ankle-brachial pressure index). Finally, with even better resolution, one can resolve structures within the vessel wall, i.e. try to characterize the plaque itself and the structures that renders it vulnerable to rupture or erosion.

A discussion of existing technological diagnostic tools that are used in the monitoring of cardiovascular disease are included in addition to emerging technologies. The chapter aims for completeness in the types of detection modalities included, even though only outlines and important results for each technique are given. The rationale behind including existing technology is that new detection modalities that characterize individual plaques must be able to show improved clinical information or cost- or time-effectiveness compared to existing methods. If thickness of the fibrous cap of a plaque is not a better predictor of clinical outcome than family history of cardiovascular disease, the former is not likely to be a cost-effective diagnostic modality. More details are included in those sections where active research has been done (i.e. diffuse reflection spectroscopy, thermography and multiphoton microscopy).

Important parameters when evaluating modalities are time, cost, radiation dose, side effects, invasiveness and of course the clinical information that can be collected. Clinically, the value of a detection modality is given

by its ability to determine the appropriate treatment in a time and cost efficient way. The treatment is prescribed from the risk of something bad happening, determined by the diagnostic modality, compared to the cost and side-effects of the treatment. If a pill that cures atherosclerosis is free and without side-effects there is no need for diagnosis. Just take your pill. Also, if the most aggressive treatment is already applied based on one risk assessment method, there is no need to further stratify the risk. There is nothing more you can do. If the most aggressive lipid lowering drug and statin therapy is prescribed, based on a Framingham risk score, there is no need for complicated invasive catheter-based assessment of coronary plaques.

However, for research purposes the technological tools play a different role. Many of the detection modalities described herein can have great value in gaining a better understanding of atherosclerosis and how risk factors are related, even though they will not make it into a clinical tool.

3.2 Systemic parameters

3.2.1 Traditional risk factors

There are certain risk factors that are easily and quickly measured and provide a risk value for the chance of developing cardiovascular disease. These are primarily obesity, high blood pressure, family history of CVD, smoking and diabetes. Based on these results, patients can be signed up for more detailed assessment that can either lower or increase the assumed risk of a cardiovascular event.

3.2.2 Biomarkers

Constituents of the serum can provide additional risk assessment over the traditional methods. Most notably are low and high density lipoprotein (LDL and HDL), and total cholesterol level. But there are other markers that have also been associated with CVD, the best known being C-reactive protein (CRP). The concentration of CRP in the blood is a marker of the overall state of inflammation in the body. It is well known that inflammation plays an important role in the progress of atherosclerosis and elevated CRP levels have been associated with increased risk of myocardial infarction. However, whether CRP is the cause or an effect of plaque rupture is unknown[65]. There is a vast array of proteins, both pro-inflammatory and anti-inflammatory that have been associated with atherosclerosis[65, 6]. With high throughput micro-array techniques, both for genomic and proteomic analysis, detailed knowledge about which proteins or genes have increased expression in atherosclerosis and vulnerable plaques is increasing. If these markers have corresponding concentrations in the blood, the risk of a ruptured plaque could perhaps be well assessed by a blood sample[42, 62].

The Framingham risk score combines traditional risk factors and biomarkers (cholesterol levels, blood pressure, diabetes, smoking and age) into a value estimating the 10 year risk of developing cardiovascular disease[117], and is used to prescribe an appropriate lipid lowering therapy. However, the risk estimates based on the Framingham study have been shown not to be accurate for all populations[102]. Another problem with the Framingham risk score is that the risk factors are present in almost everybody in some populations so that it is unable to really yield any additional risk stratification of the population. Also, this risk assessment programs provide no information about the short term risk for developing an acute coronary event[73].

3.3 Heart function

3.3.1 Electrocardiography

As the autorhythmic muscle fibers depolarize throughout the heart they set up electric potentials. By attaching electrodes to the chest (usually six) and the limbs, these potentials can be measured. Different combinations of these electrodes give information about the potential in different directions across the heart. From these signals it is possible to determine enlarged myocardium, conduction problems, arrhythmias, damaged regions and current heart attacks. For atherosclerosis the relevance of electrocardiography (EKG) is to detect stenosis (which cause reduced blood flow to the myocardium) and detection of past and current heart attacks. Within the framework of the vulnerable patient, it is an important tool for characterizing a vulnerable myocardium.

The electrocardiogram is usually described by a P-wave, a T-wave and a QRS complex. By different changes in the shape of these waves, a diagnosis of the heart can be given. For example, a flatter T-wave indicates insufficient oxygen supply that might be due to stenosis of an atherosclerotic plaque. Even though the electrocardiogram is normal at rest, a stress test can find that the heart is not receiving enough oxygen under exercise and might have a small stenosis. Since it says something about the state of the vessel, this modality might also belong to the section on modalities characterizing vessel anatomy (section 3.4). A branch of EKG is *high resolution EKG*. This is basically a method to improve the signal to noise ratio by averaging several signals thereby making very low signals called late potentials visible. The late potentials have been shown to be indicative of the prognosis after a heart attack[11].

3.3.2 Echocardiography

Echocardiography (ECG)¹ uses ultrasound to produce images of the heart. Ultrasound images are produced by sending mechanical waves into the tissue. When these waves encounter a change in acoustic impedance, the wave will be partially reflected. By measuring the time from the emitted wave to the reflected signal (about 10-100 μ s) the position of the object causing the reflectance can be determined. The radial resolution (parallel to the beam), Δx_r , is thus dependent on the width of the pulse, τ , which again is dependent on the bandwidth B

$$\Delta x_r = \frac{c\tau}{2} = \frac{c}{2B}, \quad (3.1)$$

where c is the speed of sound in the medium (about 1540 m/s for most soft tissue). The lateral resolution of the image, Δx_l , is dependent on the focusing of the beam and is described by

$$\Delta x_l = \lambda \frac{F}{D}, \quad (3.2)$$

where λ is the wavelength and F and D are the focal length and aperture, respectively. Frequencies used in biomedical imaging range from 2-30 MHz. This gives a theoretical maximum resolution in the radial direction of 20 – 400 μ m. Increasing frequency improves resolution but decreases penetration depth (rule of thumb is 0.5 dB per cm per MHz at center frequency). The resolution can also be improved by using the nonlinear part of the generated signal (usually the second harmonic).

The transducer for ECG consists of a piezoelectric ceramic with an electrode on each side. Piezoelectric materials contract or expand as a function of the applied electric field and also generate an electric field as a function of externally applied pressure. The same piezoelectric material is thus used as both detector and transducer. Focusing is achieved either by a curvature of the ceramic or an array of transducers where a phase change between the transducers cause the beam to be focused. This focusing, by adding a phase to the signals, can be used both for transmitting and detection.

Another type of ultrasound transducer is the *capacitive micromachined ultrasound transducer* (CMUT). This transducer consists of micromachined membrane with an electrode on top. By applying a time varying voltage between the electrode and the substrated the membrane can be made to oscillate and thereby generate the ultrasound signal. The small size of the membranes allow for higher frequencies than what is achievable by ceramic transducers, thereby improving the resolution. These capacitors are usually fabricated in arrays and their small size make them ideal for intravascular ultrasound (IVUS, see section 3.5.1).

¹Note that ECG is echocardiography and EKG is electrocardiography (from the german elektrokardiogram).

ECG is used to image the myocardium and heart valves. When used as an image modality for the heart, it can quantify heart function parameters like ejection fraction (fraction of blood emptied from ventricle during systole) and cardiac output (volume of blood emptied into the aorta per minute). Abnormalities in the contraction of the myocardium can be seen in ECG images. Such abnormalities seen at rest indicate a diseased myocardium, possibly due to a myocardial infarction. If the movement is normal during rest but abnormal during a stress test (induced either by exercise or drug administration), insufficient blood supply, possibly due to stenotic arteries, is indicated. Imaging of the heart is performed either through the chest (transthoracic) or through the esophagus (transesophageal, requires light sedation and is considered an invasive technique).

With doppler ultrasound, blood flow direction and velocity in the chambers of the heart can be determined. This is especially useful to investigate blood flow across heart valves and to determine septal defects.

Contrast enhancement techniques with gas-filled microbubbles exist. These microbubbles are 1-4 μm in diameter and can thus easily pass through the capillaries. The shell is made of varying materials (albumin, galactose, lipid polymers) and the gas core can consist of varying gases like air, perfluorocarbon and nitrogen. These gas bubbles have a very strong echogenicity, due to the large difference in acoustic impedance between blood and gas, and can better outline the myocardium for a more accurate determination of heart wall movement and ejection fractions. Clinical research has also been done of myocardial perfusion measurement (*myocardial contrast echocardiography*). The microbubbles are then destroyed by the ultrasound beam, and the speed of replenishment of the bubbles in the ultrasound beam is quantified, and used as a measure of perfusion in the myocardium[52]. Targeted contrast agents consist of various receptors in the body that are attached to the shell of the microbubble. Molecules can be attached to the microbubbles to make targeted contrast agents but the high velocity of the blood gives low absorption rates.

3.3.3 Nuclear imaging

Nuclear imaging methods are not used for imaging of anatomical structures on the size of vessels due to their low resolution, but rather provide information about the function of the organ in question. It is therefore not part of the arsenal of vulnerable detection techniques. A description of the technique is included here for completeness and because it is an important tool in the management of cardiovascular disease. In addition, the results of positron emission tomography (PET) on myocardial perfusion and metabolism are relevant for the thermography technique described in section 3.5.2.

Nuclear imaging is based on the emission of gamma-rays from radioac-

tive atoms injected into the body. These radioactive materials are usually incorporated into a molecule that enters into specific biological reactions. Also pure radioactive materials are preferentially taken up in some tissue types (e.g. ^{131}I in the thyroid gland). This radioactive, biologically active molecule is often called a *tracer*.

Gamma-rays can interact with matter in several ways. One is the *photoelectric effect* where a photon is absorbed and a high energy electron is ejected from an inner orbital of an atom. The path of the electron will be bent as it passes nearby nuclei, thereby emitting radiation (*brehmsstrahlung*). This emitted radiation can be in the ultraviolet or visible range (*scintillation*) and can be detected by standard photodetectors. Another process is *Compton scattering* where a high energy photon is scattered by interaction with an electron. This scattering can be elastic if the interaction is with a tightly bound electron, or inelastic if the interaction is with a weakly bound electron that gains enough energy to ionize the atom. Lastly, when a high energy photon comes near a nucleus, it can be converted to an electron/positron pair, so-called *pair production*.

The detectors of gamma rays are called *gamma cameras* and basically consist of three parts. First, a collimator, which is a metallic grid, only passes rays within a small solid angle. The gamma rays then hit a scintillation detector (usually made of NaI) that converts the gamma rays to visible light, which again is detected by photomultiplier tubes.

Single photon emission computed tomography (SPECT) measures gamma rays emitted from radiopharmaceuticals. The gamma rays are recorded by a gamma camera which can be used to compute a one dimensional profile of the concentration of the radiopharmaceuticals. By rotating the camera around the body, a two dimensional structure can be computed, in the same manner as for x-ray computed tomography (CT). Several cameras can be included to reduce the acquisition time. The resolution of the method is about 3-6 mm. As opposed to PET, this resolution is not based on fundamental limitations in the technique but because of low signal to noise ratio, requiring large area detectors for adequate signals. With better scintillation detectors or perhaps gamma-ray sensitive semiconductors it could be possible to improve the resolution of this technique.

SPECT is a slow imaging modality, generating an image takes 15-30 minutes (due to the low signal generation). Therefore, gating with an ECG signal is necessary to reduce motion artifacts from a beating heart. SPECT can measure parameters like perfusion, heart wall thickness, contractility and left ventricular ejection fraction. In *myocardial perfusion imaging* (MPI), an image of the myocardium is collected both under stress and under rest and regions of low perfusion can be determined, indicating diseased myocardium.

Positron emission tomography (PET) uses other nucleotides which emit positrons by the decay of a proton,

$$p^+ \rightarrow n + e^+. \quad (3.3)$$

The nucleotides used in PET (e.g. ^{13}C , ^{13}N , ^{15}O) are substituted for their non-radioactive counterparts in biological molecules without changing their chemical properties (generally not the case for radiopharmaceuticals used in SPECT). These radioactive nucleotides are made by in-house cyclotrons that bombard specific materials with protons. Various biological substances are then synthesized using these radioactive nucleotides. A problem overcome by in-house production is that some of the nucleotides have very short half-lives (on the order of minutes).

The positrons that are emitted are slowed down through interaction with the material. When they interact with the electrons they are almost at rest, and since the electrons are bound to an atom the kinetic energy is very low and linear momentum is close to zero[7]. The electron and positron can also combine into an atomic structure called positronium, such that the kinetic energy and linear momentum is zero. When the positron and electron annihilates, two photons of 0.511 MeV are produced which is equal to the rest mass of the electron (and positron). Since the linear momentum is zero before the annihilation, the photons must move in exactly opposite directions. If the electron and positron annihilate at higher kinetic energies, the emitted photons will not travel along a straight line and will be rejected by the coincidence circuit of the PET detector. This effect is used in the measurement of electron momenta in solids[32].

The PET detector system consists of a ring of detectors positioned around the body (usually a row of ring-detectors to expand the field of view). These detectors are connected to a coincidence circuit that determines whether the detected gamma rays were generated by the same positron, by measuring the time difference between two detected photons (which is very small, it takes a photon about 1 ns to cross the PET scanner tube). From this, the system can determine whether there is a radioactive molecule along the line of sight between the two detectors. The line can be drawn between any detectors that are within each other's line of sight (such that each detector has a fan shaped field of view). By recording the signal along many lines a 2D plane of the concentrations of these nucleotides can be determined by data processing similar to the one used in CT. PET currently gives better resolution than SPECT, but is more expensive and its cost-effectiveness in cardiology has not been proven[6]. However, the resolution of PET is fundamentally limited by the length that the positron travels before it annihilates. This length varies from 2 mm (^{18}F) to 16 mm (^{82}Rb) and the resolution can not be improved beyond this.

In cardiology, PET is used to measure perfusion and metabolism in the myocardium. The perfusion measurements are usually performed with $^{13}\text{NH}_3$ or ^{82}Rb . Because these have fairly short half-lives, rest- and stress-

tests can be performed at relatively short intervals. Metabolism in the myocardium can be assessed by 18-fluorodeoxyglucose, which enters into the glucose metabolism. These images can be used to diagnose several conditions in the myocardium, e.g. ischemia, viability after myocardial infarction and dilated myopathy.

SPECT and PET provides a complimentary imaging to the other modalities described herein, in that they describe heart function rather than the plaque burden as is done by for example coronary calcium score determined by computed tomography (CT). In this sense it provides information about short term risk compared to long term risk determined by CT[6]. SPECT and PET can detect subclinical disease with a stress-test to assess the degree of stenosis in the coronary artery. However, highly specific radiolabeled molecular markers that bind specifically to atherosclerotic lesions are developed, thereby making imaging of the degree of atherosclerosis possible with nuclear imaging techniques. Some of the processes in atherosclerotic plaques where specific tracers have been developed are monocyte recruitment, lipoprotein phagocytosis, matrix breakdown and apoptosis. In addition FDG-18 has been used to detect macrophage activity[25]. However, the limited resolution of nuclear imaging probably limits this technique to larger vessels than the coronary arteries.

3.4 Vessel anatomy

3.4.1 Coronary Angiography

Coronary angiography is the most common imaging modality in cardiovascular disease. A catheter is advanced to the ostia of the coronary arteries where an x-ray contrast medium is released, at which time the collection of X-ray images is commenced. This procedure is repeated for several angles between the x-ray machine and the body. The resulting image shows the location of the x-ray contrast medium, that is, it shows the lumen of the coronary arteries. These images can then be used to determine the degree of stenosis. The information can be used to guide interventions like coronary angioplasty, stenting and coronary bypass surgery.

Coronary angiography yields little information on the degree of atherosclerosis and cannot determine the vulnerability of a plaque. Most thrombi occur over mildly stenotic plaque which are difficult to detect with angiography due to positive remodeling. Also, no reduction in stenosis due to statin therapy was found with angiography even though the treatment had a profound effect on clinical outcome[24].

3.4.2 Magnetic Resonance Imaging

Spin is a fundamental property of particles and exists in two different states, up and down. When a particle is placed in a magnetic field, the energy of these states separate, forming a two level system. The energy difference between the states are given by the gyromagnetic ratio γ , which is an intrinsic property of a particle,

$$\Delta E = h\gamma B = h\nu, \quad (3.4)$$

where ν is the frequency of a photon with the corresponding energy, and B is the applied magnetic field. h is Planck's constant. For biomedical applications, the most important particle with non-zero net spin is the hydrogen nucleus resulting in ν in the range of 15-80 MHz for commonly used B -fields in biomedical imaging. At equilibrium the ratio of population in the two states are given by a Boltzman distribution, with slightly fewer occupying the higher states at room temperature, resulting in a net magnetization.

By applying a gradient along the body, a narrow band radio frequency (RF) signal can be used to interact with only a thin slice of the body where the energy difference of the two spin states correspond to the energy of the photons in the RF signal. By applying such a pulse the population of spins can be saturated or even inverted by absorption of RF photons. When the RF beam is turned off the population will decay back to equilibrium through spin-lattice interactions. The time of this relaxation is described by a parameter T_1 , that varies from tissue to tissue.

If a spin (or the magnetization) experiences a perpendicular magnetic field, it will start to precess. This precession moves at a frequency called the Larmor frequency which is equal to the frequency of the RF signal that is used to interact with the spins. By applying a magnetic field perpendicular to the magnetization (actually done with an RF pulse which is seen as a static field due to the precession), the magnetization can be moved down to the transverse plane (90°). When the RF pulse is turned off, the magnetization will precess due to the original magnetic field. However, due to so-called spin-spin interactions the individual spins will experience slightly different fields and precess at slightly different frequencies. Thus, the spins will dephase and the magnetization will decay. The parameter that describes this dephasing is called the spin-spin relaxation time and is denoted by T_2 . This parameter is also dependent on the tissue type.

The actual measurement is done by RF receiver coils that measure the strength and precession of the magnetization and can extract T_1 and T_2 by complicated signal processing algorithms. In addition the density of hydrogen nuclei can be extracted from these measurements.

In addition to the gradient field defining a thin slice of tissue with which the RF signals interact, other gradient fields are applied during the measurement process that impose different precession speed and phase to the

magnetization at different positions within the slice. By the appropriate filtering, the signal from a single voxel (volume element) can be found, and can be used to generate a three dimensional image of the tissue.

Within the field of cardiology, MRI has two applications, one is to characterize the vessel wall by standard imaging procedures and the other is to measure blood flow. One common pulse sequence used in MRI is the spin-echo sequence. Here, the magnetization is rotated 90° and allowed to dephase slightly before a 180° rotation is applied. This in effect causes those spins that precess faster to be moved behind those that precess slower. The spins will therefore rephase causing a so called spin-echo. Since the blood is moving the spins will have moved during the pulse sequence and no echo is generated. This makes the blood vessels appear black in images and can be visualized with good contrast (so called *black-blood imaging*). By applying the two pulses at different slices one can determine where the echo reappears and how far the blood has moved, thereby determining the blood flow (*time of flight imaging*). Similar effect can be achieved with *phase contrast imaging* where gradients with opposite signs are applied. If the object is stationary the signals will cancel, but if the object has moved, a non-zero signal will be generated. MRI is hampered by relatively long acquisition times(45 minutes[24]) to achieve sufficient quality images, especially problematic for moving organs like the heart[6].

The resolution of current MRI scanners (at 1.5 T) is about $300 \mu\text{m}$ within a slice and 2-5 mm between slices[121]. This is too large to image, with detail, the walls of the coronary arteries, but it has been used to image the walls of the carotid arteries and the aorta. By combining several contrast mechanisms in MRI (e.g. T_1 , T_2 and proton density) it has been shown that plaque components like fibrous cap, lipid core, calcification, hemorrhage and vessel area can be determined. This was done by comparing MRI images of the carotid arteries, to histological sections acquired from endarterectomy samples[82, 20]. Resolution can be improved by stronger magnetic fields. One study with 3 T fields found improved signal-to-noise and contrast-to-noise in the images[48]. In the coronary arteries MRI found thicker vessel walls in patients with cardiovascular disease compared to healthy patients, indicating that plaques with positive remodeling can be found by MRI[47]. However, for details in the vessel wall structure, the resolution is not yet good enough for the coronary arteries[67].

Clinically MRI has shown the ability to prospectively assess risk of cerebrovascular events[95]. This could perhaps also be used as a global assessment of the degree of vulnerability of the plaques and prospectively assess the risk of cardiovascular events. MRI has also been used to show the effect of treatment by statins by imaging plaques in larger arteries[22, 23].

Contrast agents

Paramagnetic contrast agents have been used to enhance imaging of blood since it reduces the T_1 parameter compared to the surrounding tissue. A study with gadolinium found that vessel wall volume changed by almost 30% compared to the same vessel with noncontrast imaging, possibly due to improvement in resolution[77].

Gadolinium has also been shown to have preferential uptake in extracellular matrix and could be used as a molecular marker for fibrous cap detection[116]. Gadolinium can also be labeled with LDL, HDL, fibrin and tissue factor to be preferentially absorbed in various tissues.

Ultrasmall paramagnetic iron oxide (USPIO) have been shown to be preferentially absorbed in macrophages[106]. Since inflammation is an important factor for plaque vulnerability, USPIO could perhaps be used as a molecular marker that can improve the detection and imaging of vulnerable plaques.

3.4.3 Computed tomography

Computed tomography (CT) images the x-ray attenuation in small volumes within the body. This is achieved by measuring the attenuation at various different angles. By a mathematical reconstruction technique called backscatter projection, or more properly by the Radon transform, the x-ray attenuation in a single volume element (voxel) can be calculated and three dimensional images of the x-ray absorption can be generated.

The source of x-rays in CT-scanners is a cathode ray tube. Electrons that are released from a hot filament are accelerated across an electrical field in a vacuum tube. The electrons hit a metal disc where they excite tightly bound electrons. As an electron decays back, it emits an x-ray photon. X-rays are also produced as bremsstrahlung when electrons are accelerated (bent) by nuclei. One of the challenges for x-ray sources is to produce very steady x-ray fluxes so that small contrast changes in the image is not obscured. Furthermore the resolution depends on the aperture of source, but there is a trade off between signal strength and resolution that is limited by the heating of the x-ray source material.

Several classes of CT scanners exist, for example electron beam tomography (EBT), helical computed tomography (HCT) and multislice computed tomography (MSCT). Usually the source moves in a ring around the patient emitting a fan of electrons that is detected by a row of detectors that moves with the source. If the patient is moved through the tube at the same time, the source will describe a helix around the patient (HCT). Several slices can be detected at the same time to reduce imaging time by adding rows of detectors, and possibly also more sources (MSCT). For cardiac imaging very short image times are necessary due to the beating heart. EBT was

designed especially for this. The source is then stationary and the scanning is achieved by electrically deflecting the electron beam across the x-ray material.

At the present, the resolution of CT (about 0.4 mm) is not good enough to image individual plaque components in the coronary arteries. The resolution of CT is fundamentally limited only by Compton scattering, but presently by source and detector sizes. Synchrotron radiation (produced by electrons accelerated in a particle accelerator) has been used to image paleontological samples with micrometer resolution[30]. Contrast is also a problem to overcome for imaging plaques since the x-ray absorption does not vary much between the different components. With advances in biological markers labeled with x-ray absorbers, this obstacle could be overcome.

Clinically, CT is presently used in cardiovascular management to measure the amount of calcifications in the coronary vessels. Coronary calcium score (CCS, or coronary artery calcium score, CACS) gives an indication of the global atherosclerotic burden and have strong predictive power for long term outcome of coronary artery disease[6]. de Weert et al. have shown that CT can be used to differentiate between lipids and fibrous tissue in the carotid artery[28]. By correlating CT measurements with histology from endarterectomy samples, they found that the x-ray absorption in Hounsfield units (HU)² of calcifications, lipids and fibrous tissue was 657 ± 416 HU, 88 ± 18 HU and 25 ± 19 HU, respectively.

CT angiography with contrast agents as a noninvasive alternative to coronary angiography has also been tested. Since regular angiography has been so successful in guiding treatment, a noninvasive procedure with the same clinical information could be very useful. CT angiography can be combined with CCS in one measurement to reduce radiation dose (even though this somewhat reduces the quality of both assessments). The presence of extensive calcification and stents makes CT for angiography difficult since they scatter the x-rays strongly, masking nearby objects. One study compared CT angiography with intravascular ultrasound (IVUS) for determining vessel wall composition and found good agreement[24]. The radiation dose in CT is higher than for conventional angiography but avoiding an invasive procedure could still be clinically advantageous.

As an example of how modalities without the necessary resolution to image coronary arteries can be valuable, it was shown that noninvasive (non-contrast) CT misses stenoses that can be seen functionally by SPECT [6].

The combination of CT and PET could provide a powerful combination with CT providing high resolution anatomical information, and PET giving metabolic information.

²Hounsfield units (HU) are a measure of x-ray absorption and are defined by setting water to $HU = 0$ and air to $HU = -1000$.

3.4.4 Ultrasonography

Ultrasonography uses equipment similar to echocardiography (section 3.3.2) to produce images of the walls of larger vessels. It can be used to image plaques in larger arteries like the carotid and femoral arteries and the aorta.

In plaque imaging, ultrasonography has shown the ability to measure the thickness of the vessel between the intima and media. The external elastic membrane and the lumen can in general be easily seen in ultrasound images and thus defines the thickness of the intima and media, which can be used as a measure of plaque thickness. This thickness in the carotid arteries (called CIMT, *carotid intima-media thickness*) has been proposed as a screening variable that describes the systemic burden of atherosclerosis[71]. With contrast agents, ultrasonography has been used to image the vasa vasorum in carotid arteries, thereby giving information on the neovascularization during atherosclerosis[35]. With the advent of targeted contrast agents that can attach to sites of inflammation, it could be possible to say something about the physiological state of the plaque. A problem with targeted microbubbles is that for flows with large sheer stress values, as they are in the aorta and carotid arteries, the fractional binding of microbubbles to the vessel wall will be very low.

3.4.5 Ankle-Brachial pressure index

If there are stenotic parts in the lower limbs, this will cause the pressure to drop along the vessel. This can be assessed by measuring the blood pressure at the ankle and the arm with a standard cuff. The difference in pressure at these two sites is called the *Ankle-brachial pressure index* (ABPI or ABI) If pressure difference is large, atherosclerosis in the lower extremities is indicated. This techniques is used to quickly and cheaply assess the systemic burden of atherosclerosis.

3.5 Vessel wall anatomy, composition and function

3.5.1 Intravascular ultrasound

Intravascular ultrasound (IVUS) uses a catheter based imaging technique where an ultrasound transducer is located at the tip of the catheter. The transducer is advanced through the coronary arteries, guided by x-ray imaging (fluoroscopy). Motorized pullback of the catheter is then performed at constant speed, usually acquiring images every 1 mm[24]. Imaging rates up to 30 frames per second are achieved. Angular scanning of a vessel can be achieved by mechanical rotation of the transducer by an electrical rotor outside the body which is connected to the transducer with a torque wire.

Another method, that allows for quicker image collection is to have an array of transducer elements located circumferentially around the catheter tip so that the angular scanning is achieved electronically.

An advantage of IVUS is the proximity to the object in question so that high frequency ultrasound, allowing for higher resolution, can be used in spite of the strong attenuation. The excitation signal used in IVUS is generally around 30MHz, yielding an axial resolution around 100 μm , even though the theoretical limit is lower. The lateral resolution is slightly higher, usually around 300 μm [113]. The resolution is therefore not good enough to determine the thickness of a thin fibrous cap.

The disadvantages of IVUS are the radiation dose (from the fluoroscopy) and the invasive nature of the procedure. In addition, IVUS is currently quite expensive.

The American college of cardiology (ACC) has published a guideline document for interpreting and reporting IVUS images[66]. The primary features detectable with IVUS are the geometry of the lumen, calcifications, lipid-rich regions and the external elastic lamina. The lumen geometry gives an indication of the degree of stenosis. The lumen surface together with the external elastic lamina can be used to calculate the total vessel wall cross-sectional area[66]. This is usually called the *intima-media thickness*, and gives a measure of the size of a plaque. It thus offers an advantage compared to angiography as it is also able to detect plaques with positive modeling. Calcifications are seen very clearly due to their strong echogenicity but with the drawback that they shadow for the underlying layers. Calcifications are detected with a sensitivity of 86-97%[113]. Plaques with calcified nodules have been proposed as a type of vulnerable plaque and IVUS could play a significant role in detecting these. Lipid rich areas are characterized by low echogenicity compared to fibrous tissue, but the contrast is low as indicated by the low sensitivities (around 40%) reported in attempts to differentiate between fibrous and lipid rich tissue[113].

IVUS has also been used to better assess the effects of angioplasty and stenting than what is possible with angiography. It has also been used as an endpoint in clinical trials of medication treatments[24] where it was found that statins increased the echogenicity of plaques, hypothesized to be due to increased fibrous or decreased lipid content in the plaques. In one study IVUS was used to determine that ruptured plaques do not occur at minimal plaques but rather at large plaques with minimal stenosis due to positive remodeling[36].

Radiofrequency analysis

Conventional IVUS measures the intensity of the backscattered signal and the recorded signal has gone through several signal processing steps like envelope filtering and gain compensation before it is recorded. Radiofrequency

(RF) ultrasound records the raw signal that is collected by the detector. Since a problem with conventional IVUS is that it differentiates poorly between fibrous and lipid-rich plaques, it was proposed that perhaps the frequency spectrum of the raw RF signal contained information to improve this differentiation. Several methods for analyzing the frequency signal has been proposed, e.g integrated backscatter[46] and frequency spectral analysis (Virtual Histology)[74]. Murashige et al. used wavelet analysis on the RF signals and found that lipid-rich plaques could be detected in-vivo with a sensitivity of 81% and a specificity of 85%[70]. A challenge has been to develop analog-to-digital converters operating at sufficient frequencies (a few times the ultrasound frequency) and sufficient bit depth, but commercial equipment is now available.

Elastography

Elastography (also called palpography) is a method for extracting the mechanical properties of the vessel wall. The tissue is imaged using IVUS at two different pressures. By correlation analysis of the two images the movement or strain of the vessel during systole is determined. Several techniques for analyzing the signal to derive the strain are used[113]. By comparing the strain to the stress induced by the blood pressure, the mechanical properties of the tissue can be extracted. The technique gives the ability to improve the contrast between soft and hard tissue that is a problem with standard IVUS, since the echogenicity difference between soft and hard tissue is small. The excitation of stress in the vessel can either be achieved using the normal variation in blood pressure or using an inflatable balloon[50].

Shear stress imaging

By combining IVUS with biplane angiography (collecting x-ray images in two orthogonal planes), the actual three dimensional geometry of the lumen can be determined. This data can be used to create a finite element model of the lumen which can be used to accurately determine the flow pattern in the vessel. From this pattern the shear stress at the surface can be determined. The shear stress is important both as a factor for plaque rupture and that it has strong effect on the endothelium and its production of cytokines and regulation of vascular tone.

Endothelial vasodilator dysfunction

The endothelium plays a key role in the development of atherosclerosis. Improper function of this organ has been associated with increased risk of cardiovascular events. The function of the endothelium can be assessed by various different methods. The vessels can be exposed to various types of stimuli, either pharmacologically or by exercise, which would cause a

reaction in the vessel wall. By measuring this response, e.g. by IVUS, the actual functioning of the vessel wall can be assessed.

3.5.2 Thermography

Temperature is a tightly regulated parameter in the human body. Just a few degrees of change during a fever quickly reduces the ability to do work. A few degrees more can be fatal (44-46°C). Too low temperatures can lead to cardiac arrhythmias while too high temperatures leads to protein denaturation.

Temperature is regulated by a thermostat in the preoptic area in the hypothalamus. This center receives impulses from thermal sensors in the skin and in the hypothalamus. When the temperature falls below the desired level the preoptic center triggers several heat promoting effects: contraction of blood vessels, release of hormones that increase metabolism (thyroid, epinephrine), and shivering. The opposite process is triggered if the temperature is too high. Fever occurs when the thermostat in the hypothalamus is reset to regulate at a higher temperature. This process can for example be initiated by phagocytes eating bacteria that release interleukin-1 which again initiates the production of prostaglandines which reset the hypothalamus thermostat[103].

Increased heat generation has been linked to inflammation by two macroscopically apparent phenomena. One is that if the body is infected, we get a fever. This is, as explained above, related to a regulatory mechanism and not increased metabolism. The other is that a local inflammation causes the skin to appear red and feel hot. However, this heat is not due to increased metabolism only (if at all), but also that the vessels are dilated (the increased optical absorption of hemoglobin causing the redness), so that more blood from the central body reaches the skin circulation. Normally, the core body temperature is higher than the skin temperature by a few degrees.

To make a mathematical model of the temperature distribution in the body, the physical mechanisms of heat transport must be determined. On the surface of the body the transport mechanisms are radiation into the surroundings (60%), convection due to heated air at the skin surface (15%), evaporation of water on the skin and in the lungs (22%) and convection into the surroundings (2%). The percentages are given for a person at rest in normal room temperature with normal humidity, and can change significantly in other conditions. E.g. at 100% humidity, evaporation can not transport temperature away from the body.

Within the human body, the primary heat transport is by convection of the flowing blood. Radiation is not a significant source of thermal conduction within the body[57]. Thermal transport by conduction requires a thermal gradient, and is not a major factor within the body since the temperature is quite similar throughout the body. The temperature in the body is regulated

by the blood moving the heat generated in the tissue to the skin and lungs where it is dissipated (by conduction, radiation or vaporization). Therefore the arterial blood must necessarily be colder than the internal organs, but warmer than the skin.

If every capillary in a given tissue volume to be modeled was to be included, the resulting geometry would be unwieldy, even for numerical methods. Therefore an assumption (and simplification) is made that for capillaries and small vessels, that the flow is so slow that the blood reaches thermal equilibrium with the surrounding tissue during its passage. Thus, the cooling by the blood is assumed to be proportional to the perfusion of the tissue, and the temperature difference between the arterial and venous blood. This model is not valid when the flow velocity increases to the point where the blood does not reach equilibrium on its pass through the tissue. The vessel must then be modeled as a separate geometry.

Based on these physical assumptions the so-called bioheat equation can be derived[76].

$$\kappa \nabla^2 T - \rho_t c_t \frac{\partial T}{\partial t} = -q + \rho_b c_b \omega (T - T_0) + \rho_b c_b \vec{v}_b \cdot \nabla T. \quad (3.5)$$

The two last terms on the right side represent perfusion and the convection, respectively. Usually, the convection term (the last term) is not included in the bioheat equation.

From autopsy studies it has been shown that macrophages are present in great numbers in ruptured plaques[26]. This prompted the hypothesis that matrix digesting enzymes released by the macrophages degrade the fibrous cap, increasing the vulnerability of the plaque. Since macrophages represent an inflammatory process, it was postulated that an increase in temperature of the plaque would accompany the macrophage infiltration. However, a recent autopsy study has shown that in patients with acute myocardial infarction, the number of inflammatory cells was four-fold higher than in a control group but that the increased inflammation was present in stable plaque as well as non-culprit segments. The difference in inflammation was only 30% between stable and vulnerable plaques within the same group. This study indicates that inflammation is primarily systemic and not located in individual plaques.

The first investigation of thermography was performed by Casscells et al. whom examined the temperature variations in carotid plaques, excised during endarterectomy, and measured the temperature using a thermistor[21]. This was compared to the density of macrophages, determined from histology. They found good correlation between macrophages and temperature and found temperature variations up to 1 K.

Many in-vivo studies have been performed both on humans and animals. The first in-vivo study was performed by Stefanadis et al. who measured the thermal heterogeneity in coronary vessels in patients with differ-

ent diagnoses[93]. They found that the thermal heterogeneity was greater in patients having suffered a myocardial infarction compared to patients suffering from unstable angina. Patients with stable angina had the lowest thermal heterogeneity. The interpretation was that patients who had suffered a myocardial infarction had a higher probability of having an inflamed vulnerable plaque which caused the increased thermal heterogeneity. This group has in several subsequent clinical studies shown the effect of thermography. It has been shown to be a predictor of clinical outcome after percutaneous coronary intervention[91], statin treatment has been shown to reduce thermal heterogeneity[90] in patients, and thermal heterogeneity has shown good correlation with concentration of acute phase proteins[92]. Results of intracoronary thermography is quite varied, so it is interesting to note that already papers are published where thermography is considered to be a standard measuring technique from which secondary information can be derived, e.g. the effect of medication on plaques[94]. It has been previously mentioned that there is a dispute about whether vulnerable plaques should be considered as a diffuse or focal diseases. A study from Stefanadis group used thermography to investigate whether temperature heterogeneity varies between culprit and non-culprit lesions[105]. Several companies (Volcano therapeutics, Thermocoil guidewire and Imetrix) have developed commercial equipment, indicating their belief in the method.

Recent studies have found much lower values than the initial studies by Stefanadis[85, 81, 104] and did not find thermal heterogeneity over 0.1 K in more than 40% of the patients[81]. Interestingly, one study found that the measured temperature heterogeneity that has been reported in the literature have decreased over the years[99]. Perhaps the laws of physics are not as constant as Einstein assumed[31].

However, only a few studies have tried to analyze the physics of the temperature generation and measurement process. These were finite element studies that investigated the effect of plaque geometry[98], probe geometry[97] and heat source location on temperature measurements[40]. Since no direct experimental values for the heat generation in plaques exist, these studies used heat generation which were derived by requiring that they fit experimental values (i.e. 1 K temperature increase).

There are two important facts that are almost never considered in the published thermography studies. One is that arterial blood must be slightly colder than the tissue. The arterial blood must be colder than the tissue (except at the skin and lungs) so that it can absorb the heat generated in the organs and transport it to the skin and lungs where it is dissipated. The other is that temperatures between organs vary. The lungs will for example be cooler than the heart since it is in contact with the colder air. In other organs the temperature difference will not be large due to the efficient perfusion. These factors are important to consider in the measurement process.

Since the arterial blood is cooler than the tissue, the thermal contact with the vessel wall will have a significant effect on the measurements. If the probe moves but a tiny bit from the vessel wall, the measured temperature will fall rapidly. Also the vessel wall temperature will depend on surrounding organs. This is especially true for the aorta which pass by diverse organs as lungs, heart, liver and intestines[111].

A study included in this thesis took another approach (Paper IV). Based on physiological consideration we found an upper limit on heat generation that could be expected in a plaque and found that a temperature increase in the center of the plaque was less than 0.1 K[57].

3.5.3 Optical coherence tomography

Optical coherence tomography (OCT) quantifies the amount of optical scattering within a small volume of tissue. The tissue is irradiated and the reflected light due to scattering is measured. By measuring the time it takes the light to go from the source via the tissue and to the detector, the point within the tissue where the reflected light originated can be determined. In this respect it is equivalent to intravascular ultrasound except that it measures the reflection of light waves instead of sound waves.

The time difference at the detector between two signals generated at locations separated by 10 μm is on the order of 10^{-13} s, and only interferometric methods can be used to measure such small time differences. The light from the source passes a beam splitter where one beam is directed to the tissue and the other to a reference mirror. If a broad band light source is used there will be maximal constructive interference at the detector between the two beams only when their optical path lengths are identical.

Light sources that are used in OCT are usually super luminescent diodes (SLD) or Ti:Sapphire lasers with bandwidths 70 nm and 120 nm, respectively. Their center wavelengths are usually 1300 nm and 800 nm respectively. The resolution in the direction parallel to the beam is dependent on the bandwidth and the center wavelength. The theoretical limit l_c is given by[14],

$$l_c = \frac{2 \ln(2) \lambda_0^2}{\pi \Delta \lambda} \quad , \quad (3.6)$$

where λ_0 is the center wavelength and $\Delta \lambda$ is the bandwidth. For a SLD system the resolution is about 13 μm and about 4 μm for a Ti:Sapphire system.

The penetration depth depends on the scattering and absorption in the tissue. The absorption loss can be somewhat compensated for by increasing the incident power. Due to the scattering there will be some photons that have travelled the same optical length as the volume in question even though they originate somewhere else. At a certain depth there will be more of these

scattered photons than those originating from the volume in question and the signal cannot be improved by increasing incident power. The penetration depth in coronary tissue have been investigated for the various layers and pathological states[64]. It was found that the attenuation coefficient at 800 nm (Ti:Sapphire laser) ranged from $3 - 10 \text{ mm}^{-1}$ and from $2.3 - 7 \text{ mm}^{-1}$ at 1300 nm (SLD). We see that the penetration depth is higher at 1300 nm than at 800 nm even though the absorption is probably highest at 1300 nm, indicating that scattering is the primary limiting factor.

The resolution in the direction perpendicular to the direction of light propagation is achieved by a lens and the resolution depends on the waist of the focused beam at the volume in question. Two different systems have been used for intravascular applications. One system (LightLab Inc.) uses a miniaturized microscope consisting of two lenses, one converging and one diverging. The other uses a gradient index lens (Massachusetts General Hospital). In both systems the light is guided through the catheter by an optical fiber and directed towards the vessel wall by a prism. Scanning in the transverse directions are achieved by rotation and pullback of the probe. The systems achieve frame rates of 30 and 8 frames/s, respectively.

OCT is equally invasive to IVUS and in-vivo studies have shown that complications (ECG changes indicating ischemia and chest pain) are equally frequent in these two modalities with no serious events reported. Due to the high scattering of blood, saline flushing is necessary during measurement and puts an additional burden on the myocardium. The scattering of blood is due to the index mismatch between the erythrocytes and the plasma. Some work on index-matching by adding dextran and ioxaglate (a contrast agent) to the plasma has been shown to increase the reflected signal from the tissue by 70% and 40%, respectively[13]. The incident power used was in the range of 5-8 mW and is considered safe. However, this depends entirely on the irradiation time and the focus of the beam but is usually safe in this application due to the high scanning rate (see paper V).

Since the resolution of OCT is an order of magnitude higher than the resolution of IVUS, it seems likely that new physiological information can be gained.

A study of 357 artery segments from the aorta, carotid and coronary arteries found OCT image criteria for physiological classification[119]. They correlated strong reflection with fibrous cap, calcifications with echolucent regions with sharp borders and lipid rich regions with echolucent regions with diffuse borders. A subset of the measurements were used as a training set for two investigators to classify plaques based on OCT images. They showed good specificity and sensitivity in the remaining samples for detecting fibrous cap, lipid rich regions and calcifications, compared to histological classification.

An in-vivo study found that OCT could detect all physiological characteristics that were detectable with IVUS, but in addition also detected

features related to intimal hyperplasia and lipid-rich regions, indicating that OCT provides additional information compared to IVUS[44].

The high resolution of OCT makes it ideal for measuring cap thickness. Two studies have shown that there is good correlation between cap thickness measured by OCT compared to histology[64, 43]. Oddly enough one of the studies reported the linear coefficient between OCT and histology less than one and the other greater than one.

Macrophage infiltration is an important parameter in plaque vulnerability because it is believed that the enzymes released by the macrophages degrade the fibrous cap. Since the index of refraction is different in the lipid rich macrophages compared to the surrounding tissue it was proposed that this would lead to a greater variance in the OCT signal. This was tested in-vitro and good correlation between OCT variance and macrophage density was found[96]. An in-vivo study found that the OCT variance was greater in patients with unstable angina compared to stable angina, speculating that higher incidence of vulnerable plaques with large macrophage densities can be found in unstable patients[59].

Another area where OCT could have an impact is stenting. Due to its high resolution it can better monitor neointimal growth and dissections after stent placement, thereby providing information that can be used to improve the procedure.

Since apparently vulnerable plaques have been found in several vessels during autopsy studies, it has been proposed that further information must be found to delineate which plaques are vulnerable. One such feature could be the collagen content of the fibrous cap. Since collagen is birefringent, a measure of the degree of birefringence in the cap could be a measure of the collagen content in the cap. One study using polarization sensitive OCT found that the degree of birefringence in the cap could be correlated with the collagen content, determined from histological stains with picrosirius[37].

OCT could also be combined with spectroscopy for even better characterization of tissue, but this has of yet not been investigated.

3.5.4 Multiphoton microscopy

Nonlinear optics

The polarization of a medium due to an electrical field can be described by the susceptibility,

$$P = \epsilon_0(\chi^{(1)}E + \chi^{(2)}E^2 + \dots) \quad (3.7)$$

Here we have used scalars but in reality P and E are vectors and $\chi^{(1)}$ is a second rank tensor, $\chi^{(2)}$ is third rank tensor and so on[10]. This is for a bulk medium. For a single molecule a similar equation can be used by

exchanging the polarization with the dipole moment and the susceptibility with the polarizability.

If monochromatic light is used the polarization due to the second term in the above equation results in polarization oscillating at the double frequency, hence light of half the wavelength of the incident light is generated, this is called second harmonic generation (SHG). In addition, the molecules can also absorb two photons at the same time. Thus, fluorescent states in a molecule can be excited by two photons with half the energy of the excited state. This is called two-photon excited fluorescence (TPEF). SHG and TPEF are the most common nonlinear optical processes used in imaging of biological tissue even though other processes like third harmonic generation and coherent anti-stokes Raman scattering (CARS) are used.

The second order susceptibility is very small so that very strong electric fields must be used to generate detectable signals. To avoid high average power from the laser that could cause photothermal damage to the tissue, pulsed lasers with very short pulses (resulting in high peak intensities) are used. The most popular laser system is the Ti:Sapphire laser that delivers pulses of about 100 fs, with a repetition rate of about 100 MHz, and average power of about 1 W. To achieve short pulses relatively large bandwidths are needed (about 10 nm) so the generated signal is not only second harmonic generation but also sum frequency generation.

Multiphoton microscopy

Using nonlinear properties of tissues have several advantages in microscopy. Red light penetrates deeper than the blue light traditionally used for exciting fluorophores and can therefore provide imaging deeper into the tissue. Also the excited signal depends quadratically on the intensity so that if a high numerical aperture objective is used, a signal is only generated near the focus. The signal will in the geometrical approximation decay as d^{-4} , where d is the distance from the focus. This approximation is not valid near the focus where the geometrical optics approximation is not valid. This means that a confocal effect is achieved without a confocal pinhole and the excited light can be collected more efficiently. Also, photobleaching is reduced since the long wavelength light is very weakly absorbed outside the focus.

Exogenous dyes can be added to a sample to improve TPEF imaging of specific structures, but also endogenous fluorophores generate TPEF and some molecules also generate SHG. Collagen I and III are the only biological molecules known to produce SHG. TPEF, on the other hand, is generated by several different proteins.

Multiphoton microscopy (MPM), the combination of microscopy and nonlinear excitation, has been used for imaging many biological tissues, both at the cellular and tissue level of organization. This include brain[41, 100, 53, 45], tumors[15], cartilage[120] and skin[49].

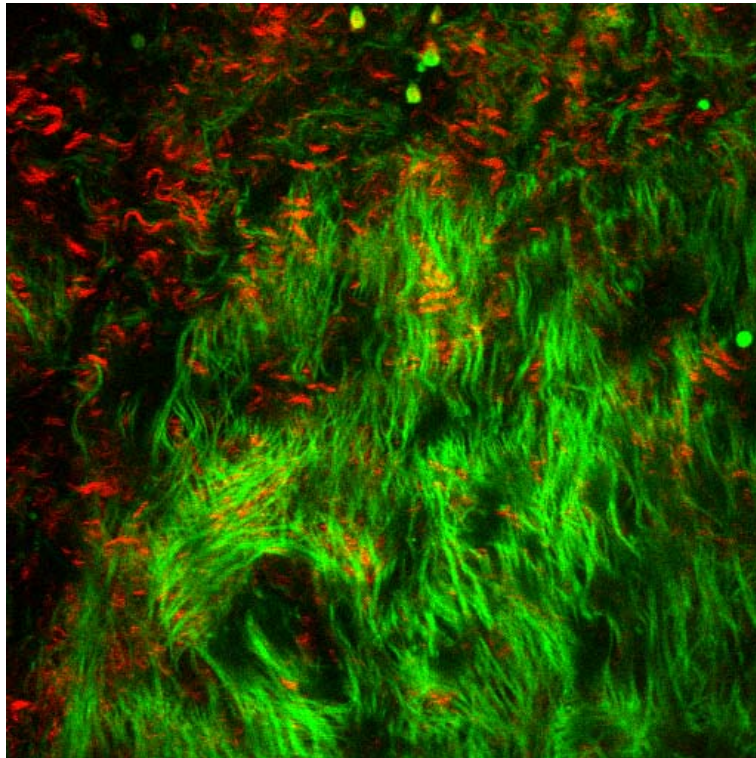


Figure 3.1: MPM image of a normal artery, near the surface. TPEF is shown in green and SHG in red. A dense layer of elastic fibers exhibiting TPEF can be seen over a layer of thin, scattered collagen fibers that give SHG. The image is $230 \times 230 \mu\text{m}$.

MPM has also been used to image cardiovascular structures. One study of atherosclerotic mice found that different structures of the plaques could be seen both in intact tissue and in stained thin sections[110]. A few studies have also confirmed that elastin and collagen can be differentiated in human vessel walls[122, 84]. As an example of a clinical application, one group investigated the vessel of rats where the parents had been exposed to *lindane* (a pesticide), and found changes in the vessel structure of the offspring[9]

It has thus been shown that MPM can efficiently image connective fibers within tissue, both elastin and collagen. In atherosclerosis, advanced plaques are characterized by a collagenous cap that covers the lipid-rich necrotic core. For vulnerable plaque the danger is that this cap ruptures exposing the lipid core. It is thus the mechanical strength of the cap that ultimately determines the vulnerability of the plaque to rupture (even though thrombotic blood and health of myocardium are important factors for the outcome). By imaging the individual collagen fibers within the cap, a better understanding of its mechanical properties can be gained[58]. (See figures 3.1 and 3.2.)

Developing an intravascular probe for multiphoton microscopy seems challenging but not impossible. There are two main obstacles. One is to develop a miniaturized microscope objective with focus control. This could perhaps be achieved by microoptical devices. The other challenge is to guide the necessary high intensity pulse through a fiber. The problem is that the broad wavelength will lead to both linear and nonlinear dispersion. However, this problem can also be overcome by prechirping techniques[107].

3.5.5 Optical spectroscopy

This section will present optical methods where light is collected in the backscatter mode, but without imaging. The reflected light gives information on the bulk optical properties of the sample which can be used to partially derive its chemical composition. Techniques that have been used for characterization of plaque are diffuse reflection spectroscopy (using visible or near-infrared (NIR) light), fluorescence spectroscopy and Raman spectroscopy.

Diffuse reflection spectroscopy

Tissue is a very turbid medium and the refractive index varies between interstitial fluid, membranes, connective fibers, lipids and cell nuclei. This variation in the refractive index causes the light to be scattered, i.e. the electromagnetic field changes its direction of propagation. When the light is scattered enough times it can be reemitted from the surface, appearing as reflected light. In the field of tissue characterization this is commonly

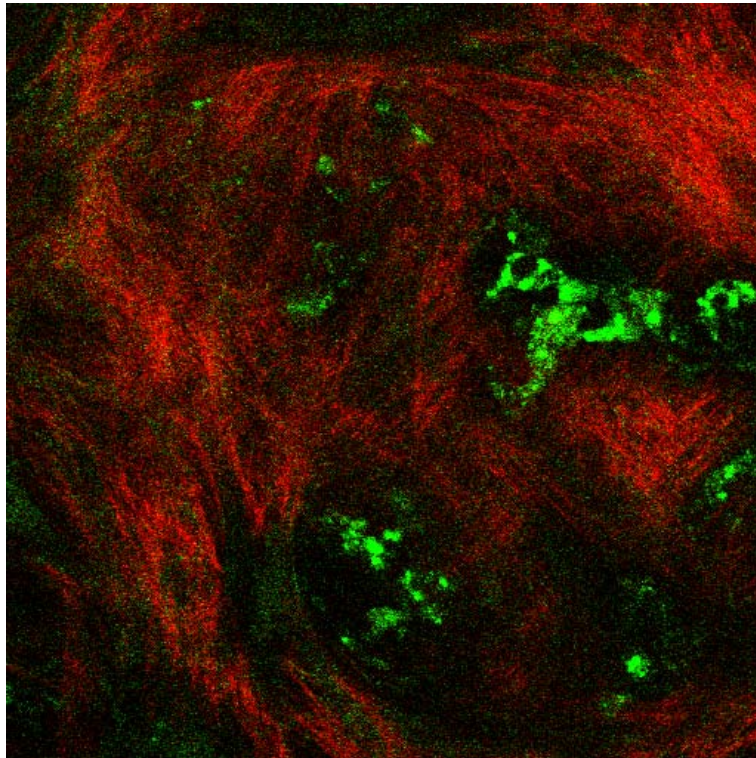


Figure 3.2: MPM image of an atherosclerotic plaque. Notice the difference in structure of the collagen fibers in this image compared to the normal artery (figure 3.1). In between the fibers are small fluorescent spheres whose nature have not been determined but could perhaps be lipid droplets within macrophages, or other cellular components. The image is $230 \times 230 \mu\text{m}$.

referred to as diffuse reflectance³.

As the light propagates through the tissue it can encounter molecules that have energy states that correspond to the photons in the beam and can absorb part of the light. The spectral dependence of the reflected light will depend on the type, location and concentration of such molecules, and therefore this information about the tissue can be extracted from the diffusely scattered light. Only the linear absorption is considered (see equation 3.7).

In addition, the scattering of the inhomogeneities in the tissue is not the same for all wavelengths, usually it will tend to decrease for longer wavelengths. Less scattering effectively means that the light travels deeper into the tissue before it can be reemitted. Scattering from tissue is usually divided into Mie-scattering (for objects on the order of the wavelength) and Rayleigh scattering (for objects that are much smaller than the wavelength). The scattering as a function of wavelength for Mie-scattering depends on the ratio of the wavelength and the size of the object, but is generally less wavelength dependent than Rayleigh scattering which goes as λ^{-4} .

The refractive index mismatch between the tissue and the surrounding medium is also important as it can cause the light to be internally reflected at the surface, thereby traveling further through the tissue.

Since the scattering quickly makes the light incoherent, phase and polarization of the light field is usually ignored and only the intensity of the light is considered. This is called the model of radiative transfer. The basic equation describing radiative transfer is the Boltzmann equation.

$$\begin{aligned} \frac{1}{c} \frac{\partial L(\vec{r}, \hat{s}, t)}{\partial t} + \hat{s} \cdot \nabla L(\vec{r}, \hat{s}, t) = & -(\mu_a + \mu_s)L(\vec{r}, \hat{s}, t) \\ & + \mu_s \iint_{4\pi} d\Omega' L(\vec{r}, \hat{s}', t) f(\hat{s} \cdot \hat{s}') + Q \end{aligned} \quad (3.8)$$

Here L is the radiance, defined as the power through an infinitesimal small area at point \vec{r} and in the direction of an infinitesimal small solid angle $d\Omega$ in the direction \hat{s} ,

$$L(\vec{r}, \hat{s}, t) = \frac{dP}{dAd\Omega} \quad (3.9)$$

μ_a and μ_s are the absorption and scattering coefficients, respectively, which are defined as the change in light intensity over an infinitesimally

³In tissue characterization, light reflected from the surface (without penetrating the tissue) is referred to as specular reflection. In other fields specular reflection refers to surface reflection obeying Snell's law of reflection at equal angles, and diffuse reflection refers to surface reflection from a coarse surface so that light is reflected at all angles. What is called diffuse reflection in the field of tissue characterization (and this thesis) is also known as transfection.

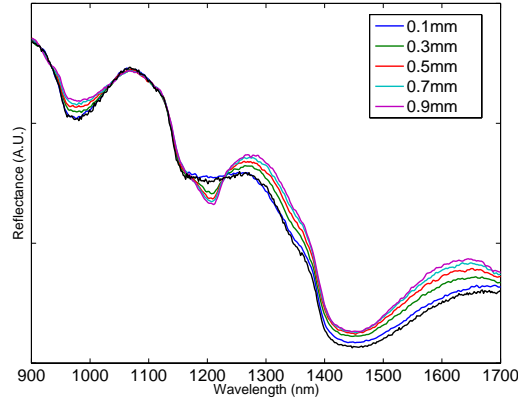


Figure 3.3: Monte Carlo simulation of a layer of fat of various thickness 0.1 mm below the surface, giving the diffuse reflection as a function of wavelength. The absorption of pure porcine fat was used for the lipid layer. The only absorber in the rest of the tissue was water at a 70% concentration. The absorption peak of fat at 1210 nm can be seen.

small length dx , $dI = \mu_i I dx$, where i can be substituted by either a or s . The term $f(\hat{s} \cdot \hat{s}')$ is the probability that a photon travelling in the direction \hat{s} will be scattered in the direction \hat{s}' . This factor is also called the phase function. Q is a source term and c the speed of light. The source term can for example represent fluorescent light generated in the tissue, or collimated light that is diffused when the diffusion approximation is used (see below).

The Boltzmann equation cannot be solved analytically. Simplifications must be made or one must resolve to numerical methods. One common simplification for samples where the scattering dominates over the absorption is the diffusion approximation. The basis of this model is that since the medium is highly scattering, the radiance will be nearly isotropic and can be described by an isotropic fluence rate together with a small directional flux

$$L = \frac{\phi}{4\pi} + \frac{3}{4\pi} \vec{j} \cdot \hat{s} \quad (3.10)$$

Substituting this expression in the Boltzmann equation and integrating over the appropriate variables yields a diffusion type equation that can be solved analytically[39].

Monte Carlo simulation is a popular numerical tool. This technique simulates packages of photons that are launched into the tissue and their path is traced using probabilities based on μ_a , μ_s and f . By repeating this many times a statistical distribution of the light in the tissue can be found. Figure 3.3 shows Monte Carlo simulations of a one dimensional model of

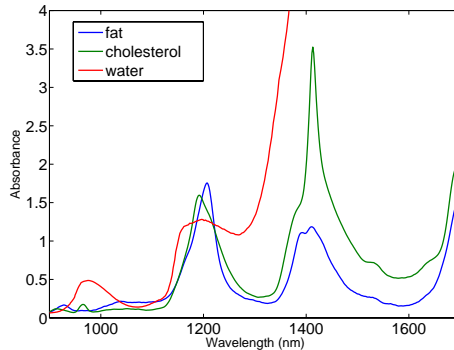


Figure 3.4: Absorbance A of porcine fat, cholesterol and water. Measured in the liquid phase in a 1 cm cuvette.

a layer of fat of varying thickness, embedded in tissue, 0.1 mm below the surface.

The most common methods to collect the reflected light from a tissue is either by a fiber optic probe or an integrating sphere. These are usually connected via an optical fiber to a spectrometer which sends the data to a computer. The integrating sphere collects light down to a depth of about one penetration depth. The penetration depth in highly scattering media can be defined from the diffusion approximation to be $\delta = \frac{1}{\sqrt{3\mu_a\mu_{tr}}}$ where $\mu_{tr} = \mu_a + (1 - g)\mu_s$. With optical fibers one can change the volume which is investigated. One fiber can be used for the illumination and one for the collection of the reflected light. By increasing this distance, the light will travel deeper before reaching the detector and a larger volume is sampled. For example in the work presented in *paper III*, we used a probe with a central collection fiber with seven illumination fibers in a tight circle around the central fiber. Another had four fibers placed in a linear array, each separated by 150 μm . Usually the reflectance spectra are reported relative to a reflectance standard which is assumed to have wavelength independent reflection of almost 100%.

In the NIR part of the spectrum, the primary absorbers are water and lipids of various types (e.g. free or esterified cholesterol and triglycerides), and hemoglobin up to about 1100nm. Figure 3.4 shows the absorbance, $A = -\log(I/I_0)$ of important absorbers in the NIR region, relevant to detection of plaque.

Water is always present in biological tissue and usually dominates the NIR reflectance spectra unless the measurement is performed through whole blood (see figure 3.7). However, one can see in figure 3.4 that the absorption of lipids around 1210 nm is comparable to the water absorption, indicating that this wavelength could be used to detect lipids in tissue. As a preliminary experiment to test whether NIR spectroscopy could be used to detect lipids,

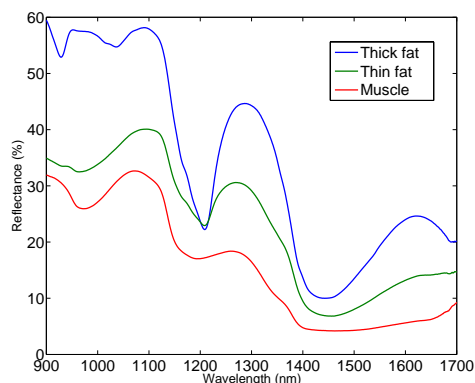


Figure 3.5: Reflection spectra taken at various sites on the outside of a bovine heart, both muscular areas and of thick adipose tissue. The spectra of muscular tissue shows the water absorption at 980 nm, 1190nm and around 1450nm. The spectra of thick adipose tissue shows lipid absorption peaks at 930 nm, 1080 nm and 1210 nm. In addition the large water absorption peak at 1450 nm dominates the spectra at higher wavelengths. The area with thin adipose tissue had some dried blood over it which can be seen by the broad absorption from 900 nm to about 1100 nm due to oxy-hemoglobin.

we measured the diffuse reflectance at various sites on the surface of a bovine heart. Figure 3.5 shows the reflectance from muscle and adipose tissue. The absorption peaks from figure 3.4 are clearly visible. Water at 980 nm, 1190 nm and 1450 nm and lipids at 930 nm, 1050 nm and 1210 nm.

A few studies have been published in this field. The first study used Fourier transform infrared (FTIR) spectroscopy and found that they could spatially differentiate between lipids and connective tissue in sections of aortic tissue[61]. They collected spectra from 3-12 μm . This has since been developed to include imaging and it has been found that elastic lamella and foam cells could be imaged[19]. Spectra were collected in the range 2.6-10 μm However IR light is not very useful for in-vivo applications since the penetration depth is only about 10 μm . Using NIR light gives good penetration depth, especially in the so-called optical window from 800-1200 nm. One study using light from 1100-2200 nm for reflection spectroscopy using partial least squares analysis found that they could detect lipids, thin cap and inflammatory cells with good sensitivity and specificity (90% and 93%, 77% and 93%, 84% and 89%, respectively)[68]. A similar study using cluster analysis found that lipid/protein ratio extracted from the spectra correlated with histological classification according to the American Heart Association[114]. A company called Infraredx is trying to commercialize this technique and claims to be on the brink of clinical trials.

In the visible range important absorbers are blood and carotenoids. Clin-

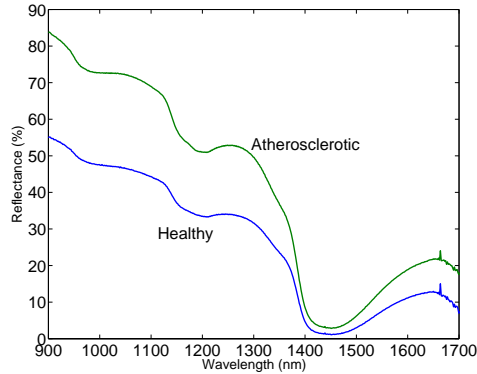


Figure 3.6: Reflectance spectra from healthy and atherosclerotic rabbit aorta

ical studies with angiography have shown that a "yellow glistening plaque" is associated with vulnerable plaques, determined from histology. This yellow color could be due to carotenoids that bind to the lipids within the plaque. It has been shown that beta-carotene taken orally has preferential absorption in plaques[8]. The reflectance spectra of plaques in the visible region was investigated, but it was found that it offered poor sensitivity and specificity for detecting plaques compared to the NIR spectrum[56]. This could be due to the strong overlap of the blood absorption with the carotenoid absorption. Only small amounts of blood in the vasa vasorum would strongly affect the spectra.

Previously published work on the reflection spectra from atherosclerotic plaques use statistical methods to determine whether vulnerable plaques can be differentiated from stable ones[68]. A drawback of statistical methods is that the measurement must be performed in its actual setting (i.e. in-vivo) to develop the actual training set that serves the basis for diagnosis.

We used a more analytic approach, which makes it easier to determine how the spectra will vary in an in-vivo setting.

To test the technique on an atherosclerotic plaque, aorta samples from atherosclerotic rabbits were excised and the diffuse reflectance was measured using a fiber optic probe. The results are shown in figure 3.6. One can see that the scattering from plaques are higher than for healthy aorta, probably due to increased scattering from fibrous cap or lipid droplets in the necrotic core. Also, for the atherosclerotic sample, at 1210 nm there is a small dip in the reflectance superimposed on the water absorption at 1190 nm. This could be due to the lipids in the plaque. The amount of lipid in the plaque was based on the change in the derivative of the spectra close to the lipid absorption line at 1200 nm[56].

To explore this further, reflectance measurements on human aorta was performed and it was shown that it could detect lipids in plaques with quite

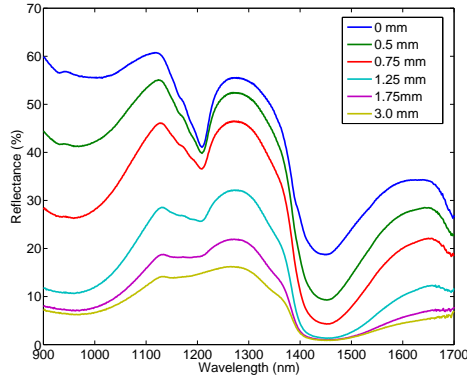


Figure 3.7: Measurement of a piece of adipose tissue taken from a bovine heart measured through a thin layer of blood, the thickness which is specified in the legend.

good sensitivity and specificity[56].

In intravascular measurements, the presence of blood might cause a problem for detection of plaque since blood has a significant absorption in the NIR range. Figure 3.7 shows the reflectance spectra when a sample of adipose tissue was measured through a layer of blood and how the signal varies with increasing distance between the probe and the sample. Through 3 mm of blood the absorption peaks due to lipids could no longer be seen.

Raman spectroscopy

When a photon interacts with a molecule it can be scattered inelastically, thereby slightly changing its wavelength. This is called Raman scattering. The wavelength change is highly characteristic of the type of molecule and depends on the structure of the vibrational bands. The photon can both lose and gain energy in this process (Stokes and anti-Stokes scattering, respectively). The interaction is very weak so that relatively high intensity light and efficient light collection methods must be used. Traditional Raman spectroscopy used in material characterization used visible light. In biological tissue the absorption of visible light is quite strong leading to low penetration depths, and a lot of background fluorescence, making the Raman signal harder to detect. Therefore, near-infrared sources were used instead. Since the Raman signal is so weak, many different statistical methods have been investigated to extract the signal in an efficient manner[86, 27].

The first studies on arterial tissue used a Nd:Yag laser and found strong Raman bands that could be attributed to vibrations in amid groups, C-H groups and phosphate groups[78, 5]. This indicated that the method was useful for detecting collagen (amid groups), lipids (C-H groups) and calcifi-

cations (phosphate groups). Later this was confirmed by quantifying these components by Raman spectroscopy and comparing the results to chemical methods, where good agreement was found[12]. In a preliminary test of the clinical application of Raman spectroscopy, spectra were collected from excised coronary arteries[80]. A subset of the samples was defined as a training set that was used to determine component spectra that indicated various states of disease. They then used these component spectra on the remaining samples and found that Raman spectroscopy served as a good predictor for non-atherosclerotic vessel, non-calcified and calcified lesions. Buschman et al. collected Raman spectra from different morphological structures and found that these could serve as a complete basis set for spectra that were collected from an intact vessel, i.e. the measured spectra could be completely reconstructed by adding various weights of the component spectra[18]. In-vivo trials on lamb and sheep found that blood only affected the signal as an added component and therefore relatively easily could be removed from the spectra[17]. Human in-vivo studies have recently been performed on vessels scheduled for endarterectomy and femoral bypass[69]. They found that vulnerable plaques could be detected with specificity of 84% and sensitivity of 79%. Raman spectroscopy has also been used in the monitoring of pharmacological treatment of atherosclerotic mice, where it was found that there was a strong reduction in cholesterol and calcifications within the artery after treatment of atorvastatin[109, 108].

Fluorescence spectroscopy

When a molecule is irradiated by light the electrons can be excited by the absorption of a photon. This atom will then emit a photon as it decays back to the ground state. However, some of the energy is lost to molecular vibrations before the decay so that the emitted photon has slightly longer wavelength. This process is called fluorescence.

There are several substances in the arteries that exhibit fluorescence. The most important are collagen, calcifications, ceroid and carotenoids. The problem with fluorescence is that all the different components have broad fluorescence spectra with large overlap, making it difficult to discern the various components. The fluorescence is also dependent on the chemical environment of the molecule. One study compared the fluorescence of pure elements with different features of a plaque[4]. They found that the fluorescence spectra of atherosclerotic plaque was similar to collagen, the lipid core to oxidized lipoproteins, and normal vessel to collagen.

The earliest works on fluorescence of atherosclerosis were for the automatic guiding of laser ablation techniques[51, 29]. Later, studies of whether fluorescence can differentiate different types of plaques seem to end up with the conclusion that they can differentiate between calcified and non-calcified regions[83, 79, 55]. Recently, it has also been shown that a combination of

diffuse reflectance spectroscopy and intrinsic fluorescence could detect superficial foam cells in atherosclerotic plaques[3].

A problem with in-vivo fluorescence is the strong absorption of blood. Just a small amount of blood between the probe and tissue will have a significant effect on the recorded spectra. One way to overcome this problem is to measure the blood layer and calibrate for it. One study used IVUS for measuring the blood layer and found improved diagnostic ability with this calibration[115].

Another method is to use time resolved fluorescence spectroscopy and differentiate the plaques based on varying fluorescent decay time constants[33, 2, 1]. The advantage is that this parameter is not affected by a layer of blood between the probe and tissue.

3.5.6 Angioscopy

Angioscopy is a method to directly visualize the surface of the lumen. Angioscopic catheters usually consist of a fiberoptic bundle attached to a detector system, where each fiber creates a pixel in the image. This technique is one of the few where prospective studies have been conducted. It has been found that plaques with a yellowish color (xanthomatous plaques) are correlated with unstable angina and higher risk of developing acute coronary events[75, 101]. A disadvantage of coronary angioscopy is that the vessels have to be flushed with phosphate buffered saline during imaging, due to the strong blood absorption.

Chapter 4

Conclusions

4.1 Conclusions

Do not fear to be eccentric in opinion, for every opinion now accepted was once eccentric.

Bertrand Russell, british philosopher and mathematician.

The technology stands today at a point where it is possible for the clinician to get almost unlimited detail of the tissue in question if he so desires. From the movement of the myocardium as a whole to individual collagen fibers in a plaque (about five orders of magnitude different in size). However, the drawback of more detail, is often higher cost, time expenditure, and invasiveness.

The question is then: How much detail is needed to find the necessary clinical information. Many methods now exist for characterizing coronary plaques and it seems likely that vulnerable plaques can be detected. The best method for characterizing plaques depends on the exact feature to be detected and the resources available. More prospective studies are necessary to determine this.

If treatment of vulnerable plaques is systemic, one might as well look for plaques in more accessible arteries to assess a more global plaque burden. This seems likely to give a more cost-effective clinical solution. However, if local treatment of vulnerable plaques is developed, methods for localizing them within coronary arteries will become more valuable. Still, detailed imaging procedures are important for research purposes to determine what a vulnerable plaque really is.

If the future should bring us local treatment modalities that warrants individual plaque detection, a likely superior detection modality could be a combination of ultrasound for rapid size determination, NIR reflection spectroscopy for rapid lipid-determination, and multiphoton techniques (or OCT) for cap thickness and structure characterization.

Modality	Invasive	Resolution	VP	Comments
Systemic markers	No	-	Inflammation (?).	Biomarkers for atherosclerotic and non-specific inflammation. Detect vulnerable blood.
EKG	No	-	-	Stress test for subclinical stenosis. Detect vulnerable heart.
ECG	No	-	-	Stress test for subclinical stenosis. Vulnerable heart.
SPECT	No	10-15 mm	Inflammation	Stress test for subclinical stenosis. Targeted contrast agents for plaque components.
PET	No	4-5 mm	Inflammation	Stress test for subclinical stenosis. Targeted contrast agents for plaque components. Image larger arteries.
MRI	No	300 μm	Size, inflammation, lipids.	Image carotid arteries and aorta.
CT	No	500 μm	Size, lipid	Measure stenosis and coronary calcium score. Image larger arteries
Ultrasonography	No	200 μm	Size, lipid (?).	Image carotid arteries and aorta.
ABI	No	-	-	
Angiography	Yes	500 μm	-	Image stenosis.
IVUS	Yes	50-100 μm	Size, lipid.	
Thermography	Yes	-	Inflammation (?)	Probably not working.
OCT	Yes	10 μm	Fibrous cap, lipid core, inflammation (?)	
Multiphoton microscopy	Yes	1 μm	Cap thickness and structure	
Optical spectroscopy	Yes	-	Lipid	NIR, fluorescence and Raman

Table 4.1: An overview of the properties of the detection modalities presented in this work. The resolution of imaging techniques and the various features of vulnerable plaques that can be detected. A question mark is added where the possibility of detecting a feature is uncertain.

Chapter 5

Future work

5.1 Future Work

Fear to be eccentric in opinion, for many opinions once eccentric are still eccentric.

Magnus Lilledahl, Norwegian poet.

Even though the techniques of spectroscopy and multiphoton microscopy might be too advanced for plaque detection (since treatments are lacking), they will be a valuable tool in understanding plaque development that warrants further development of the modalities. Furthermore, they show great promise for locally characterizing tissue. A microscopic tool that can be used in multiple organs with multiple sensors for characterizing tissue could be quite useful. This will open up in-vivo information to clinicians that were once the domain of pathologists. A miniaturized microscope, measuring various optical interactions (SHG, TPEF, CARS,...) could realize a true optical biopsy that has been promised for so long.

Bibliography

- [1] S. Andersson-Engels, J. Johansson, U. Stenram, K. Svanberg and S. Svanberg. Time-resolved laser induced fluorescence spectroscopy for enhanced demarcation of human atherosclerotic plaques. *J. Photochem. and Photobiol.*, 4:363–369, 1990.
- [2] S. Andersson-Engels, J. Johansson and S. Svanberg. The use of time-resolved fluorescence for diagnosis of atherosclerotic plaque and malignant tumours. *Spectrochimica Acta A*, 46:1203–1210, 1990.
- [3] George O. Angheloiu, Joseph T. Arendt, Markus G. Muller, Abigail S. Haka, Irene Georgakoudi, Jason T. Motz, Obrad R. Scepanovic, Barry D. Kuban, Jonathan Myles, Frank Miller, Eugene A. Podrez, Maryann Fitzmaurice, John R. Kramer and Michael S. Feld. Intrinsic fluorescence and diffuse reflectance spectroscopy identify superficial foam cells in coronary plaques prone to erosion. *Arterioscler. Thromb. Vasc. Biol.*, 26(7):1594–1600, 2006.
- [4] K. Arakawa, K. Isoda, I. Toshimitu, K. Nakajima, T. Shibuya and F. Ohsuzu. Fluorescence analysis of biochemical constituents identifies atherosclerotic plaque with a thin fibrous cap. *Arterioscler. Thromb. Vasc. Biol.*, 1:1–71, 2002.
- [5] J. J. Baraga, M. S. Feld and R. P. Rava. In situ optical histochemistry of human artery using near infrared Fourier transform Raman spectroscopy. *PNAS*, 89(8):3473–3477, 1992.
- [6] Daniel S. Berman, Rory Hachamovitch, Leslee J. Shaw, John D. Friedman, Sean W. Hayes, Louise E. J. Thomson, David S. Fieno, Guido Germano, Nathan D. Wong, Xingping Kang and Alan Rozanski. Roles of nuclear cardiology, cardiac computed tomography, and cardiac magnetic resonance: Noninvasive risk stratification and a conceptual framework for the selection of noninvasive imaging in patients with known or suspected coronary artery disease. *The Journal of Nuclear Medicine*, 47(7):1107–1118, 2006.
- [7] K. Bethge, G. Kraft, P. Kreisler and G. Walter. *Medical applications of nuclear physics*. Springer, 2004.

- [8] David H. Blankenhorn, David G. Freiman and Harvey C. Knowles. Carotenoids in man. The distribution of epiphasic carotenoids in atherosclerotic lesions. *J. Clin. Invest.*, 35:1243–1247, 1956.
- [9] T. Boulesteix, A. M. Pena, N. Pagés, G. Godeau, M. P. Sauviat, E. Beaurepaire and M. C. Schanne-Klein. Micrometer scale ex vivo multiphoton imaging of unstained arterial wall structure. *Cytometry Part A*, 69A(1):20–26, 2006.
- [10] Robert W. Boyd. *Nonlinear Optics*. Accademic Press, Inc., 1992.
- [11] G. Breithardt, J. Schwarzmaier, M. Borggrefe, K. Haerten, and L. Seipel. Prognostic significance of late ventricular potentials after acute myocardial infarction. *Eurupean Heart Journal*, 4(7):487–95, 1983.
- [12] James F. Brennan III, Tjeerd J. Romer, Robert S. Lees, Anna M. Tercyak, John R. Kramer Jr. and Michael S. Feld. Determination of human coronary artery composition by Raman spectroscopy. *Circulation*, 96(1):99–105, 1997.
- [13] Mark Brezinski, Kathleen Saunders, Christine Jesser, Xingde Li and James Fujimoto. Index matching to improve optical coherence tomography imaging through blood. *Circulation*, 103(15):1999–2003, 2001.
- [14] Mark E. Brezinski, Guillermo J. Tearney, Brett E. Bouma, Joseph A. Izatt, Michael R. Hee, Eric A. Swanson, James F. Southern and James G. Fujimoto. Optical coherence tomography for optical biopsy: Properties and demonstration of vascular pathology. *Circulation*, 93(6):1206–1213, 1996.
- [15] Edward Brown, Trevor McKee, Emmanuelle diTomaso, Alain Pluen, Brian Seed, Yves Boucher and Rakesh K. Jain. Dynamic imaging of collagen and its modulation in tumors in vivo using second-harmonic generation. *Nature Medicine*, 9(6):796–800, 2003.
- [16] Allen P. Burke, Andrew Farb, Gray T. Malcom, You-Hui Liang, John Smialek and Renu Virmani. Coronary risk factors and plaque morphology in men with coronary disease who died suddenly. *N. Engl. J. Med.*, 336(18):1276–1282, 1997.
- [17] H. P. Buschman, E. T. Marple, M. L. Wach, B. Bennett, T. C. Bakker Schut, H. A. Bruining, A. V. Bruschke, A. van der Laarse and G. J. Puppels. In vivo determination of the molecular composition of artery wall by intravascular Raman spectroscopy. *Anal. Chem.*, 72(16):3771–3775, 2000.

- [18] Hendrik P. Buschman, Jason T. Motz, Geurt Deinum, Tjeerd J. Romer, Maryann Fitzmaurice, John R. Kramer, Arnoud van der Laarse, Albert V. Brusckhe and Michael S. Feld. Diagnosis of human coronary atherosclerosis by morphology-based Raman spectroscopy. *Cardiovascular Pathology*, 10(2):59–68, 2001.
- [19] C. S. Colley, S. G. Kazarian, P. D. Weinberg and M. J. Lever. Spectroscopic imaging of arteries and atherosclerotic plaques. *Biopolymers*, 74(4):328–335, 2004.
- [20] Vincent C. Cappendijk, Kitty B. J. M. Cleutjens, Alfons G. H. Kessels, Sylvia Heeneman, Geert Willem H. Schurink, Rob J. T. J. Welten, Werner H. Mess, Mat J. A. P. Daemen, Jos M. A. van Engelshoven and M. Eline Kooi. Assessment of human atherosclerotic carotid plaque components with multisequence MR imaging: Initial experience. *Radiology*, 234(2):487–492, 2005.
- [21] Ward Casscells, Marian Hathorn David, Tim Krabach, William K. Vaughn, Hugh A. McAllister, Greg Bearman and James T. Willerson. Thermal detection of cellular infiltrates in living atherosclerotic plaques: Possible implications for plaque rupture and thrombosis. *The Lancet*, 347:1447–1449, 1996.
- [22] Roberto Corti, Zahi A. Fayad, Valentin Fuster, Stephen G. Worthley, Gerard Helft, James Chesebro, Michele Mercuri and Juan J. Badimon. Effects of lipid-lowering by simvastatin on human atherosclerotic lesions: A longitudinal study by high-resolution, noninvasive magnetic resonance imaging. *Circulation*, 104(3):249–252, 2001.
- [23] Roberto Corti, Valentin Fuster, Zahi A. Fayad, Stephen G. Worthley, Gerard Helft, Donald Smith, Jesse Weinberger, Jolanda Wentzel, Gabor Mizsei, Michele Mercuri and Juan J. Badimon. Lipid lowering by simvastatin induces regression of human atherosclerotic lesions: Two years follow-up by high-resolution noninvasive magnetic resonance imaging. *Circulation*, 106(23):2884–2887, 2002.
- [24] John R. Crouse. Imaging atherosclerosis: State of the art. *Journal of Lipid Research*, 47:1677–1694, 2006.
- [25] John R. Davies, James H. F. Rudd, Peter L. Weissberg and Jagat Narula. Radionuclide imaging for the detection of inflammation in vulnerable plaques. *J. Am. Coll. Cardiol.*, 47(8 Suppl C):C57–68, 2006.
- [26] M. J. Davies, N. Woolf, P. Rowles and P. D. Richardson. Lipid and cellular constituents of unstable human aortic plaques. *Basic Res. Cardiol.*, 89 Suppl 1:33–9, 1994.

- [27] Jr Alderico R. de Paula and Sokki Sathaiah. Raman spectroscopy for diagnosis of atherosclerosis: A rapid analysis using neural networks. *Medical Engineering and Physics*, 27(3):237–244, 2005.
- [28] Thomas T. de Weert, Mohamed Ouhlous, Erik Meijering, Pieter E. Zondervan, Johanna M. Hendriks, Marc R. H. M. van Sambeek, Diederik W. J. Dippel and Aad van der Lugt. In vivo characterization and quantification of atherosclerotic carotid plaque components with multidetector computed tomography and histopathological correlation. *Arterioscler. Thromb. Vasc. Biol.*, 26(10):2366–2372, 2006.
- [29] Lawrence I. Deckelbaum. Fluorescence spectroscopy in cardiovascular disease. Fundamental concepts and clinical applications. *Trends in cardiovascular medicine*, 1(4):171–176, 1991.
- [30] Philip C. J. Donoghue, Stefan Bengtson, Xi-ping Dong, Neil J. Gostling, Therese Huldtgren, John A. Cunningham, Chongyu Yin, Zhao Yue, Fan Peng and Marco Stampanoni. Synchrotron x-ray tomographic microscopy of fossil embryos. *Nature*, 442(7103):680–683, 2006.
- [31] A. Einstein. Zur elektrodynamik bewegter körper. *Annalen der Physik*, 322(10):891–921, 1905.
- [32] Robert Eisberg and Robert Resnick. *Quantum physics of atoms, molecules, solids, nuclei and particles*. John Wiley and sons, 1985.
- [33] Q. Fang, J. Jo, T. Papaioannou, A. Dorafshar, T. Reil, Qiao Jian-Hua, C. M. Fishbein, J. A. Freischlag and L. Marcu. Validation of a time-resolved fluorescence spectroscopy apparatus using a rabbit atherosclerosis model. In *Proceedings of SPIE*, vol. 5312, 294–299, 2005.
- [34] Andrew Farb, Allen P. Burke, Anita L. Tang, Youhui Liang, Poonam Mannan, John Smialek and Renu Virmani. Coronary plaque erosion without rupture into a lipid core: A frequent cause of coronary thrombosis in sudden coronary death. *Circulation*, 93(7):1354–1363, 1996.
- [35] Steven B. Feinstein. The powerful microbubble: From bench to bedside, from intravascular indicator to therapeutic delivery system, and beyond. *Am. J. Physiol. Heart. Circ. Physiol.*, 287(2):H450–457, 2004.
- [36] Kenichi Fujii, Gary S. Mintz, Stephane G. Carlier, Jose di Ribamar Costa Jr, Masashi Kimura, Koichi Sano, Kaoru Tanaka, Ricardo A. Costa, and Joanna Lui. Intravascular ultrasound profile analysis of ruptured coronary plaques. *The American Journal of Cardiology*, 98(4):429–435, 2006.

- [37] S. D. Giattina, B. K. Courtney, P. R. Herz, M. Harman, S. Shortkroff, D. L. Stamper, B. Liu, J. G. Fujimoto and M. E. Brezinski, "Assessment of coronary plaque collagen with polarization sensitive optical coherence tomography (PS-OCT)", *International Journal of Cardiology* **107**(3), pp. 400–409, (2006).
- [38] D. Hackett, G. Davies and A. Maseri. Pre-existing coronary stenoses in patients with first myocardial infarction are not necessarily severe. *Eur. Heart J.*, 9(12):1317–1323, 1988.
- [39] Richard C. Haskell, Lars O. Svaasand, T. Tsay, T. Feng, Matthew S. McAdams and Bruce J. Tromberg. Boundary conditions for the diffusion equation in radiative transfer. *Journal of the Optical Society of America A*, 11:2727–2741, 1994.
- [40] A. G. ten Have, F. J. H. Gijzen, J. J. Wentzel, C. J. Slager, P. W. Serruys and A. F. W. van der Steen. A numerical study on the influence of vulnerable plaque composition on intravascular thermography measurements. *Phys. Med. Biol.*, 51(22):5875, 2006.
- [41] Fritjof Helmchen, Michale S. Fee, David W. Tank and Winfried Denk. A miniature head-mounted two-photon microscope: High-resolution brain imaging in freely moving animals. *Neuron*, 31(6):903–912, 2001.
- [42] Joerg Herrmann. New kits on the blot - can we microarray the future of atherosclerosis? *Cardiovascular Research*, 60(2):220–222, 2003.
- [43] Ik-kyung Jang. Cardiovascular optical coherence tomography. Ex-vivo results. In *The 4th vulnerable plaque satellite symposium at TCT*, Chicago, 2002. Association for the eradication of heart attack.
- [44] Ik-Kyung Jang, Brett E. Bouma, Dong-Heon Kang, Seung-Jung Park, Seong-Wook Park, Ki-Bae Seung, Kyu-Bo Choi, Milen Shishkov, Kelly Schlendorf, Eugene Pomerantsev, Stuart L. Houser, H. Thomas Aretz and Guillermo J. Tearney. Visualization of coronary atherosclerotic plaques in patients using optical coherence tomography: Comparison with intravascular ultrasound. *J Am Coll Cardiol*, 39(4):604–609, 2002.
- [45] Juergen C. Jung, Amit D. Mehta, Emre Aksay, Raymond Stepnoski and Mark J. Schnitzer. In vivo mammalian brain imaging using one- and two-photon fluorescence microendoscopy. *J. Neurophysiol.*, 92(5):3121–3133, 2004.
- [46] Masanori Kawasaki, Hisato Takatsu, Toshiyuki Noda, Keiji Sano, Yoko Ito, Kenji Hayakawa, Kunihiko Tsuchiya, Masazumi Arai, Kazuhiko Nishigaki, Genzou Takemura, Shinya Minatoguchi, Takako

- Fujiwara and Hisayoshi Fujiwara. In vivo quantitative tissue characterization of human coronary arterial plaques by use of integrated backscatter intravascular ultrasound and comparison with angioscopic findings. *Circulation*, 105(21):2487–2492, 2002.
- [47] W. Yong Kim, Matthias Stuber, Peter Bornert, Kraig V. Kissinger, Warren J. Manning and Rene M. Botnar. Three-dimensional black-blood cardiac magnetic resonance coronary vessel wall imaging detects positive arterial remodeling in patients with nonsignificant coronary artery disease. *Circulation*, 106(3):296–299, 2002.
- [48] Ioannis Koktzoglou, Yiu-Cho Chung, Venkatesh Mani, Timothy J. Carroll, Mark D. Morasch, Gabor Mizsei, Orlando P. Simonetti, Zahi A. Fayad and Debiao Li. Multislice dark-blood carotid artery wall imaging: A 1.5 T and 3.0 T comparison. *Journal of Magnetic Resonance Imaging*, 23(5):699–705, 2006.
- [49] Karsten Konig and Iris Riemann. High-resolution multiphoton tomography of human skin with subcellular spatial resolution and picosecond time resolution. *Journal of Biomedical Optics*, 8(3):432–439, 2003.
- [50] Chris L. de Korte, Anton F. W. van der Steen, E. Ignacio Cespedes, Gerard Pasterkamp, Stephane G. Carlier, F. Mastik, Arjen H. Schoneveld, Patrick W. Serruys and Nicolaas Bom. Characterization of plaque components and vulnerability with intravascular ultrasound elastography. *Phys. Med. Biol.*, 45(6):1465, 2000.
- [51] M. B. Leon, Y. Almagor, A. L. Bartorelli, L. G. Prevosti, P. S. Teirstein, R. Chang, D. L. Miller, P. D. Smith, and R. F. Bonner. Fluorescence-guided laser-assisted balloon angioplasty in patients with femoropopliteal occlusions. *Circulation*, 81(1):143–155, 1990.
- [52] Wolfgang Lepper, Todd Belcik, Kevin Wei, Jonathan R. Lindner, Jiri Sklenar, and Sanjiv Kaul. Myocardial contrast echocardiography. *Circulation*, 109(25):3132–3135, 2004.
- [53] Michael J. Levene, Daniel A. Dombek, Karl A. Kasischke, Raymond P. Molloy, and Watt W. Webb. In vivo multiphoton microscopy of deep brain tissue. *J. Neurophysiol.*, 91(4):1908–1912, 2004.
- [54] Peter Libby. Inflammation in atherosclerosis. *Nature*, 420(6917):868–874, 2002.
- [55] Magnus B. Lilledahl, M. Barkost, M. W. Gran, Olav A. Haugen, and Lars O. Svaasand. The effect of a thin bloodlayer on intravascular fluorescence spectroscopy. In *Proceedings of SPIE*, 2006.

- [56] Magnus B. Lilledahl, M. Barkost, M. W. Gran, Olav A. Haugen, and Lars O. Svaasand. Reflection spectroscopy of atherosclerotic plaque. *Journal of Biomedical Optics*, 11(2), 2006.
- [57] Magnus B. Lilledahl, Eivind La Publa Larsen, and Lars O. Svaasand. An analytic and numerical analysis of thermography of vulnerable plaque. *Phys. Med. Biol.*, In Press.
- [58] Magnus Borstad Lilledahl, Catharina de Lange Davies, and Lars Othar Svaasand. Multiphoton microscopy of unstained healthy and atherosclerotic aorta. *Journal of Biomedical Optics* Conditionally accepted.
- [59] Briain D MacNeill, Ik-Kyung Jang, Brett E Bouma, Nicusor Iftimia, Masamichi Takano, Hiroshi Yabushita, Milen Shishkov, Christopher R Kauffman, Stuart L Houser, and H Thomas Aretz. Focal and multifocal plaque macrophage distributions in patients with acute and stable presentations of coronary artery disease. *Journal of the American College of Cardiology*, 44(5):972–979, 2004.
- [60] Mohammad Madjid, Alireza Zarrabi, Silvio Litovsky, James T. Willerson, and Ward Casscells. Finding vulnerable atherosclerotic plaques: Is it worth the effort? *Arteriosclerosis Thrombosis and Vascular Biology*, 24(10):1775–1782, 2004.
- [61] Ramasamy Manoharan, Joseph J. Baraga, Richard P. Rava, Ramachandra R. Dasari, Maryann Fitzmaurice, and Michael S. Feld. Biochemical analysis and mapping of atherosclerotic human artery using FT-IR microspectroscopy. *Atherosclerosis*, 103(2):181–193, 1993.
- [62] Wim Martinet, Dorien M. Schrijvers, Guido R. Y. De Meyer, Arnold G. Herman, and Mark M. Kockx. Western array analysis of human atherosclerotic plaques: Downregulation of apoptosis-linked gene 2. *Cardiovascular Research*, 60(2):259–267, 2003.
- [63] Alessandro Mauriello, Giuseppe Sangiorgi, Stefano Fratoni, Giampiero Palmieri, Elena Bonanno, Lucia Anemona, Robert S. Schwartz, and Luigi Giusto Spagnoli. Diffuse and active inflammation occurs in both vulnerable and stable plaques of the entire coronary tree: A histopathologic study of patients dying of acute myocardial infarction. *Journal of the American College of Cardiology*, 45(10):1585–1593, 2005.
- [64] F. J. van der Meer, D. J. Faber, J. Perra, G. Pasterkamp, D. Baraznji Sassoon, and T. G. van Leeuwen. Quantitative optical coherence tomography of arterial wall components. *Lasers in Medical Science*, V20(1):45–51, 2005.

- [65] Roger Mills and Deepak L. Bhatt. The yin and yang of arterial inflammation. *Journal of the American College of Cardiology*, 44(1):50–52, 2004.
- [66] Gary S. Mintz, Steven E. Nissen, William D. Anderson, Steven R. Bailey, Raimund Erbel, Peter J. Fitzgerald, Fausto J. Pinto, Kenneth Rosenfield, Robert J. Siegel, and E. Murat Tuzcu. American college of cardiology clinical expert consensus document on standards for acquisition, measurement and reporting of intravascular ultrasound studies (IVUS): A report of the american college of cardiology task force on clinical expert consensus documents developed in collaboration with the european society of cardiology endorsed by the society of cardiac angiography and interventions. *Journal of the American College of Cardiology*, 37(5):1478–1492, 2001.
- [67] Robbert-Jan J. H. M. Miserus, Sylvia Heeneman, Jos M. A. van Engelsehoven, Marianne Eline Kooi, and Mat J. A. P. Daemen. Development and validation of novel imaging technologies to assist translational studies in atherosclerosis. *Drug Discovery Today: Technologies*, 3(2):195–204, 2006.
- [68] Pedro R. Moreno, Robert A. Lodder, Raman Purushotaman, William E. Charash, William N. O’Connor, and James E. Muller. Detection of lipid pool, thin fibrous cap and inflammatory cells in human aortic atherosclerotic plaques by near-infrared spectroscopy. *Circulation*, 105:923–927, 2002.
- [69] Jason T. Motz, Maryann Fitzmaurice, Arnold Miller, Saumil J. Gandhi, Abigail S. Haka, Luis H. Galindo, Ramachandra R. Dasari, John R. Kramer, and Michael S. Feld. In vivo Raman spectral pathology of human atherosclerosis and vulnerable plaque. *Journal of Biomedical Optics*, 11(2):021003–9, 2006.
- [70] Akihiro Murashige, Takafumi Hiro, Takashi Fujii, Koji Imoto, Takashige Murata, Yusaku Fukumoto, and Masunori Matsuzaki. Detection of lipid-laden atherosclerotic plaque by wavelet analysis of radiofrequency intravascular ultrasound signals: In vitro validation and preliminary in vivo application. *Journal of the American College of Cardiology*, 45(12):1954–1960, 2005.
- [71] Morteza Naghavi, Erling Falk, Harvey S. Hecht, Michael J. Jamieson, Sanjay Kaul, Daniel Berman, Zahi Fayad, Matthew J. Budoff, John Rumberger, and Tasneem Z. Naqvi. From vulnerable plaque to vulnerable patient—part III: Executive summary of the screening for heart attack prevention and education (SHAPE) task force report. *The American Journal of Cardiology*, 98(2, Supplement 1):2–15, 2006.

- [72] Morteza Naghavi, Peter Libby, Erling Falk, S. Ward Casscells, Silvio Litovsky, John Rumberger, Juan Jose Badimon, Christodoulos Stefanadis, Pedro Moreno, Gerard Pasterkamp, Zahi Fayad, Peter H. Stone, Sergio Waxman, Paolo Raggi, Mohammad Madjid, Alireza Zarrabi, Allen Burke, Chun Yuan, Peter J. Fitzgerald, David S. Siscovick, Chris L. de Korte, Masanori Aikawa, K. E. Juhani Airaksinen, Gerd Assmann, Christoph R. Becker, James H. Chesebro, Andrew Farb, Zorina S. Galis, Chris Jackson, Ik-Kyung Jang, Wolfgang Koenig, Robert A. Lodder, Keith March, Jasenka Demirovic, Mohammad Navab, Silvia G. Priori, Mark D. Rekhter, Raymond Bahr, Scott M. Grundy, Roxana Mehran, Antonio Colombo, Eric Boerwinkle, Christie Ballantyne, Jr. Insull, William, Robert S. Schwartz, Robert Vogel, Patrick W. Serruys, Goran K. Hansson, David P. Faxon, Sanjay Kaul, Helmut Drexler, Philip Greenland, James E. Muller, Renu Virmani, Paul M. Ridker, Douglas P. Zipes, Prediman K. Shah, and James T. Willerson. From vulnerable plaque to vulnerable patient: A call for new definitions and risk assessment strategies: Part I. *Circulation*, 108(14):1664–1672, 2003.
- [73] Morteza Naghavi, Peter Libby, Erling Falk, S. Ward Casscells, Silvio Litovsky, John Rumberger, Juan Jose Badimon, Christodoulos Stefanadis, Pedro Moreno, Gerard Pasterkamp, Zahi Fayad, Peter H. Stone, Sergio Waxman, Paolo Raggi, Mohammad Madjid, Alireza Zarrabi, Allen Burke, Chun Yuan, Peter J. Fitzgerald, David S. Siscovick, Chris L. de Korte, Masanori Aikawa, K. E. Juhani Airaksinen, Gerd Assmann, Christoph R. Becker, James H. Chesebro, Andrew Farb, Zorina S. Galis, Chris Jackson, Ik-Kyung Jang, Wolfgang Koenig, Robert A. Lodder, Keith March, Jasenka Demirovic, Mohammad Navab, Silvia G. Priori, Mark D. Rekhter, Raymond Bahr, Scott M. Grundy, Roxana Mehran, Antonio Colombo, Eric Boerwinkle, Christie Ballantyne, Jr. Insull, William, Robert S. Schwartz, Robert Vogel, Patrick W. Serruys, Goran K. Hansson, David P. Faxon, Sanjay Kaul, Helmut Drexler, Philip Greenland, James E. Muller, Renu Virmani, Paul M. Ridker, Douglas P. Zipes, Prediman K. Shah, and James T. Willerson. From vulnerable plaque to vulnerable patient: A call for new definitions and risk assessment strategies: Part II. *Circulation*, 108(15):1772–1778, 2003.
- [74] Anuja Nair, Barry D. Kuban, E. Murat Tuzcu, Paul Schoenhagen, Steven E. Nissen, and D. Geoffrey Vince. Coronary plaque classification with intravascular ultrasound radiofrequency data analysis. *Circulation*, 106(17):2200–2206, 2002.
- [75] Tomohito Ohtani, Yasunori Ueda, Isamu Mizote, Jota Oyabu, Katsuki Okada, Atsushi Hirayama, and Kazuhisa Kodama. Number of yellow

- plaques detected in a coronary artery is associated with future risk of acute coronary syndrome: Detection of vulnerable patients by angiography. *Journal of the American College of Cardiology*, 47(11):2194–2200, 2006.
- [76] Harry H. Pennes. Analysis of tissue and arterial blood temperatures in the resting human forearm. *Applied physiology*, 1(2):93–122, 1948.
- [77] Binh An P. Phan, Baocheng Chu, William S. Kerwin, Dongxiang Xu, Chun Yuan, Thomas Hatsukami, and Xue-Qiao Zhao. Effect of contrast enhancement on the measurement of carotid arterial lumen and wall volume using MRI. *Journal of Magnetic Resonance Imaging*, 23(4):481–485, 2006.
- [78] R. P. Rava, J. J. Baraga, and M. S. Feld. Near infrared Fourier transform Raman spectroscopy of human artery. *Spectrochimica Acta Part A: Molecular Spectroscopy*, 47(3-4):509–512, 1991.
- [79] R. Richards-Kortum, R. P. Rava, M. Fitzmaurice, J. R. Kramer, and M. S. Feld. 476 nm excited laser-induced fluorescence spectroscopy of human coronary arteries: Applications in cardiology. *American Heart Journal*, 122:1141–1150, 1991.
- [80] Tjeerd J. Romer, James F. Brennan III, Maryann Fitzmaurice, Michael L. Feldstein, Geurt Deinum, Jonathan L. Myles, John R. Kramer, Robert S. Lees, and Michael S. Feld. Histopathology of human coronary atherosclerosis by quantifying its chemical composition with Raman spectroscopy. *Circulation*, 97(9):878–885, 1998.
- [81] Lukasz Rzeszutko, Jacek Legutko, Grzegorz L. Kaluza, Marcin Wizimirski, Angela Richter, Michal Chyrchel, Grzegorz Heba, Jacek S. Dubiel, and Dariusz Dudek. Assessment of culprit plaque temperature by intracoronary thermography appears inconclusive in patients with acute coronary syndromes. *Arterioscler. Thromb. Vasc. Biol.*, 26(8):1889–1894, 2006.
- [82] T. Saam, M. S. Ferguson, V. L. Yarnykh, N. Takaya, D. Xu, N. L. Polissar, T. S. Hatsukami, and C. Yuan. Quantitative evaluation of carotid plaque composition by in vivo MRI. *Arteriosclerosis Thrombosis and Vascular Biology*, 25(1):234–239, 2005.
- [83] M. Sartori, R. Sauerbrey, S. Kubodera, F. Tittel, R. Roberts, and P. Henry. Autofluorescence maps of atherosclerotic human arteries - a new technique in medical imaging. *Quantum Electronics, IEEE Journal of*, 23(10):1794–1797, 1987.

- [84] Katja Schenke-Layland, Iris Riemann, Ulrich A. Stock, and Karsten Konig. Imaging of cardiovascular structures using near-infrared femtosecond multiphoton laser scanning microscopy. *Journal of Biomedical Optics*, 10(2):024017–5, 2005.
- [85] Axel Schmermund, Jörg Rodermann, and Raimund Erbel. Intracoronary thermography. *Herz*, 28(6):505–512, 2003.
- [86] Landulfo Silveira, Sokki Sathaiiah, Renato A. Zángaro, Marcos T. T. Pacheco, Maria C. Chavantes, and Carlos A. G. Pasqualucci. Correlation between near-infrared raman spectroscopy and the histopathological analysis of atherosclerosis in human coronary arteries. *Lasers in Surgery and Medicine*, 30(4):290–297, 2002.
- [87] Herbert C. Stary, David H. Blankenhorn, A. Bleakley Chandler, Seymour Glagov, William Insull Jr., Mary Richardson, Michael E. Rosenfeld, Sheldon A. Schaffer, Colin J. Schwartz, William D. Wagner, and Robert W. Wissler. A definition of the intima of human arteries and of its atherosclerosis-prone regions. *Circulation*, 85(1):391–405, 1992.
- [88] Herbert C. Stary, A. Bleakley Chandler, Robert E. Dinsmore, Valentin Fuster, Seymour Glagov, William Insull Jr., Michael E. Rosenfeld, Colin J. Schwartz, William D. Wagner, and Robert W. Wissler. A definition of advanced types of atherosclerotic lesions and a histological classification of atherosclerosis. *Circulation*, 92:1355–1374, 1995.
- [89] Herbert C. Stary, A. Bleakley Chandler, Seymour Glagov, John R. Guyton, William Insull, Micheal E. Rosenfeld, Sheldon A. Schaffer, Colin J. Schwartz, William D. Wagner, and Robert W. Wissler. A definition of initial, fatty streak, and intermediate lesions of atherosclerosis. *Arteriosclerosis and Thrombosis*, 14(5):840–856, 1994.
- [90] C. Stefanadis, K. Toutouzas, M. Vavuranakis, E. Tsiamis, D. Tousoulis, D. B. Panagiotakos, S. Vaina, C. Pitsavos, and P. Toutouzas. Statin treatment is associated with reduced thermal heterogeneity in human atherosclerotic plaques. *Eur. Heart J.*, 23(21):1664–9, 2002.
- [91] Christodoulos Stefanadis. Increased local temperature in human coronary atherosclerotic plaques: An independent predictor of clinical outcome in patients undergoing a percutaneous coronary intervention. *Journal of the American College of Cardiology*, 37:1277–1283, 2001.
- [92] Christodoulos Stefanadis, Leonidas Diamantopoulos, John Dernellis, Emanuel Economou, Eleftherios Tsiamis, Konstantinos Toutouzas, Charalambos Vlachopoulos, and Pavlos Toutouzas. Heat production of atherosclerotic plaques and inflammation assessed by the acute phase

- proteins in acute coronary syndromes. *Journal of Molecular and Cellular Cardiology*, 32(1):43–52, 2000.
- [93] Christodoulos Stefanadis, Leonidas Diamantopoulos, Charalambos Vlachopoulos, Eleftherios Tsiamis, John Dernellis, Konstantinos Toutouzas, Elli Stefanadi, and Pavlos Toutouzas. Thermal heterogeneity within human atherosclerotic coronary arteries detected in vivo: A new method of detection by application of a special thermography catheter. *Circulation*, 99(15):1965–1971, 1999.
- [94] Christodoulos Stefanadis, Konstantinos Toutouzas, Eleftherios Tsiamis, Manolis Vavuranakis, Costas Tsioufis, Elli Stefanadi, and Harisios Boudoulas. Relation between local temperature and c-reactive protein levels in patients with coronary artery disease: Effects of atorvastatin treatment. *Atherosclerosis*, In Press, Corrected Proof, 2006.
- [95] Norihide Takaya, Chun Yuan, Baocheng Chu, Tobias Saam, Hunter Underhill, Jianming Cai, Nam Tran, Nayak L. Polissar, Carol Isaac, Marina S. Ferguson, Gwenn A. Garden, Steven C. Cramer, Kenneth R. Maravilla, Beverly Hashimoto, and Thomas S. Hatsukami. Association between carotid plaque characteristics and subsequent ischemic cerebrovascular events: A prospective assessment with MRI—initial results. *Stroke*, 37(3):818–823, 2006.
- [96] Guillermo J. Tearney, Hiroshi Yabushita, Stuart L. Houser, H. Thomas Aretz, Ik-Kyung Jang, Kelly H. Schlendorf, Christopher R. Kauffman, Milen Shishkov, Elkan F. Halpern, and Brett E. Bouma. Quantification of macrophage content in atherosclerotic plaques by optical coherence tomography. *Circulation*, 107(1):113–119, 2003.
- [97] Anna G. ten Have, Erasmus B. G. T. Draaijers, Frank J. H. Gijzen, Jolanda J. Wentzel, Cornelis J. Slager, Patrick W. Serruys, and Antonius F. W. van der Steen. Influence of catheter design on lumen wall temperature distribution in intracoronary thermography. *Journal of Biomechanics*, In Press, Corrected Proof, 2006.
- [98] Anna. G. ten Have, F. J. H. Gijzen, J. J. Wentzel, C. J. Slager, and A. F. W. van der Steen. Temperature distribution in atherosclerotic coronary arteries: Influence of plaque geometry and flow (a numerical study). *Phys. Med. Biol.*, 49:4447–4462, 2004.
- [99] Anna G. ten Have, Frank J. H. Gijzen, Jolanda J. Wentzel, Cornelis J. Slager, Patrick W. Serruys, and Antonius F.W. van der Steen. Intracoronary thermography, heat generation, transfer and detection. *Eurointervention*, 1(1):105–114, 2005.

- [100] Patrick Theer, Mazahir T. Hasan, and Winfried Denk. Two-photon imaging to a depth of 1000 micrometers in living brains by use of a Ti:Al₂O₃ regenerative amplifier. *Opt. Lett.*, 28(12):1022–1024, 2003.
- [101] Torsten Thieme, Klaus D. Wernecke, Rudolph Meyer, Elke Brandenstein, Dirk Habedank, Antje Hinz, Stephan B. Felix, Gert Baumann, and Franz X. Kleber. Angioscopic evaluation of atherosclerotic plaques: Validation by histomorphologic analysis and association with stable and unstable coronary syndromes. *Journal of the American College of Cardiology*, 28(1):1–6, 1996.
- [102] Troels F. Thomsen, Dan McGee, Michael Davidsen, and Torben Jorgensen. A cross-validation of risk-scores for coronary heart disease mortality based on data from the Glostrup population studies and Framingham heart study. *International Journal of Epidemiology*, 31(4):817–822, 2002.
- [103] Gerard J. Tortora and Sandra Reynolds Grabowski. *Principles of Anatomy and Physiology*. Wiley, 2003.
- [104] K. Toutouzas, M. Drakopoulou, V. Markou, P. Stougianos, E. Tsiamis, D. Tousoulis, and C. Stefanadis. Increased coronary sinus blood temperature: Correlation with systemic inflammation. *Eur. J. Clin. Invest.*, 36(4):218–23, 2006.
- [105] Konstantinos Toutouzas, Maria Drakopoulou, John Mitropoulos, Eleftherios Tsiamis, Sophia Vaina, Manolis Vavuranakis, Virginia Markou, Eirini Bosinakou, and Christodoulos Stefanadis. Elevated plaque temperature in non-culprit de novo atheromatous lesions of patients with acute coronary syndromes. *Journal of the American College of Cardiology*, 47(2):301–306, 2006.
- [106] Rikin A. Trivedi, Jean-Marie U-King-Im, Martin J. Graves, Justin J. Cross, Jo Horsley, Martin J. Goddard, Jeremy N. Skepper, George Quartey, Elizabeth Warburton, Ilse Joubert, Liqun Wang, Peter J. Kirkpatrick, John Brown, and Jonathan H. Gillard. In vivo detection of macrophages in human carotid atheroma: Temporal dependence of ultrasmall superparamagnetic particles of iron oxide-enhanced MRI. *Stroke*, 35(7):1631–1635, 2004.
- [107] Mankei Tsang, Demetri Psaltis, and Fiorenzo G. Omenetto. Reverse propagation of femtosecond pulses in optical fibers. *Opt. Lett.*, 28(20):1873–1875, 2003.
- [108] Sweder W. E. van de Poll, Dianne J. M. Delsing, J. Wouter Jukema, Hans M. G. Princen, Louis M. Havekes, Gerwin J. Puppels, and

- Arnoud van der Laarse. Raman spectroscopic investigation of atorvastatin, amlodipine, and both on atherosclerotic plaque development in apoe*3 leiden transgenic mice. *Atherosclerosis*, 164(1):65–71, 2002.
- [109] Sweder W. E. van de Poll, Tjeerd J. Romer, Oscar L. Volger, Dianne J. M. Delsing, Tom C. Bakker Schut, Hans M. G. Princen, Louis M. Havekes, J. Wouter Jukema, Arnoud van der Laarse, and Gerwin J. Puppels. Raman spectroscopic evaluation of the effects of diet and lipid-lowering therapy on atherosclerotic plaque development in mice. *Arteriosclerosis Thrombosis and Vascular Biology*, 21(10):1630–1635, 2001.
- [110] M. van Zandvoort, W. Engels, K. Douma, L. Beckers, M. oude Egbrink, M. Daemen, and D. W. Slaaf. Two-photon microscopy for imaging of the (atherosclerotic) vascular wall: A proof of concept study. *Journal of Vascular Research*, 41(1):54–63, 2004.
- [111] Stefan Verheye, Guido R. Y. De Meyer, Glenn Van Langenhove, Michiel W. M. Knaapen, and Mark M. Kockx. In vivo temperature heterogeneity of atherosclerotic plaques is determined by plaque composition. *Circulation*, 105(13):1596–1601, 2002.
- [112] R. Virmani, Frank D. Kolodgie, Allen P. Burke, Andrew Farb, and Stephen M. Schwartz. Lessons from sudden coronary death. A comprehensive morphological classification scheme for atherosclerotic lesions. *Arteriosclerosis Thrombosis and Vascular Biology*, 17:1337–1345, 2000.
- [113] Ron Waksman and Patrick W. Serruys, editors. *Handbook of the vulnerable plaque*. Taylor and Francis, London, 2004.
- [114] Jing Wang, Y. Geng, Bujin Guo, Tomas Klima, Birendra N. Lal, James T. Willerson, and S. Ward Casscells. Near-infrared spectroscopic characterization of human advanced atherosclerotic plaque. *Atherosclerosis*, 39:1305–1313, 2002.
- [115] S. Warren, K. Pope, Y. Yazdi, A. J. Welch, S. Thomsen, A. L. Johnston, M. J. Davis, and R. Richards-Kortum. Combined ultrasound and fluorescence spectroscopy for physico-chemical imaging of atherosclerosis. *Biomedical Engineering, IEEE Transactions on*, 42(2):121–132, 1995.
- [116] Robert L. Wilensky, Hee Kwon Song, and Victor A. Ferrari. Role of magnetic resonance and intravascular magnetic resonance in the detection of vulnerable plaques. *Journal of the American College of Cardiology*, 47(8 Suppl C):C48–56, 2006.

- [117] Peter W. F. Wilson, Ralph B. D'Agostino, Daniel Levy, Albert M. Belanger, Halit Silbershatz, and William B. Kannel. Prediction of coronary heart disease using risk factor categories. *Circulation*, 97(18):1837–1847, 1998.
- [118] www.wikipedia.org.
- [119] Hiroshi Yabushita, Brett E. Bouma, Stuart L. Houser, H. Thomas Aretz, Ik-Kyung Jang, Kelly H. Schlendorf, Christopher R. Kauffman, Milen Shishkov, Dong-Heon Kang, Elkan F. Halpern, and Guillermo J. Tearney. Characterization of human atherosclerosis by optical coherence tomography. *Circulation*, 106(13):1640–1645, 2002.
- [120] Alvin T. Yeh, Marie J. Hammer-Wilson, David C. Van Sickle, Hilary P. Benton, Aikaterini Zoumi, Bruce J. Tromberg, and George M. Peavy. Nonlinear optical microscopy of articular cartilage. *Osteoarthritis and Cartilage*, 13(4):345–352, 2005.
- [121] Chun Yuan and William S. Kerwin. MRI of atherosclerosis. *Journal of Magnetic Resonance Imaging*, 19(6):710–719, 2004.
- [122] Aikaterini Zoumi, Xiao Lu, Ghassan S. Kassab, and Bruce J. Tromberg. Imaging coronary artery microstructure using second-harmonic and two-photon fluorescence microscopy. *Biophysical journal*, 87(4):2778–2786, 2004.

Paper I

Characterization of atherosclerotic plaque by reflection spectroscopy and thermography: A comparison

Magnus B. Lilledahl, Olav A. Haugen, Lise L. Randeberg and Lars O. Svaasand. *Proceedings of SPIE*, vol. 5686, 415-425 (2005)

Characterization of Atherosclerotic Plaque by Reflection Spectroscopy and Thermography: A comparison

Magnus B. Lilledahl^a, Olav A. Haugen^{b,c}, Lise L. Randeberg^a and Lars O. Svaasand^a

^aDepartment of Electronics and Telecommunications, Norwegian University of Science and Technology;

^bDepartment of Morphology, Norwegian University of Science and Technology;

^cDepartment of Pathology, St. Olav's University Hospital.

ABSTRACT

Many methods for detecting and measuring vulnerable atherosclerotic plaques have been proposed. These include reflection spectroscopy, thermography, ultrasound, computed tomography (CT) and magnetic resonance imaging (MRI). This paper presents an analysis and a comparison of two of these methods, near-infrared reflection spectroscopy (NIRS) and thermography.

Most of the published literature evaluate methods statistically. A more analytic approach will make it easier to compare the different methods and determine if the measured signal will be strong enough in a real measurement situation. This is the approach taken in this article.

Eight samples of human aorta were examined by NIRS and subsequently prepared for histology. A total of 28 measurement points were selected. A measure of the lipid content based on reflection spectra is proposed. Comparisons of this lipid measure with histology show that the lipid content in the plaques yields relatively small changes in the value of this *lipid-index*. Reflectance spectra from models based on the diffusion approximation for total reflectance were simulated.

Temperature measurements were performed on three Watanabe heritable hyperlipidemic (WHHL) rabbits and one New Zealand white (NZW) rabbit with a thermistor-type intravascular temperature sensor. The measurements gave no significant signals which correlated with the subsequent histology. A simple analytic model was developed which indicates that a temperature increase of more than $0.01 - 0.04^{\circ}\text{C}$ at the surface of a vessel wall, due to inflammation in a plaque, is unlikely. Such a small temperature difference will probably be obscured by normal variation in the vessel wall temperature.

Keywords: Atherosclerosis, NIR, reflection spectroscopy, thermography, plaque

1. INTRODUCTION

A large number of deaths in the industrialized countries are caused by acute cardiovascular events. Clinical studies have shown that the majority of sudden myocardial ischemia can be traced back to the rupture of atherosclerotic plaques which cause a sudden thrombotic occlusion of the vessel.¹ Plaques that are prone to rupture are denoted *vulnerable plaques*.

Many detection modalities with different advantages and disadvantages have been proposed. Some are already in clinical use. Some of these are angiography, intravascular ultrasound (IVUS), computed tomography (CT) and magnetic resonance imaging (MRI). Angiography is currently the standard method. However, it only images the internal volume of the lumen. Since many plaques grow radially outwards from the lumen and even small, non-stenotic plaques can rupture, the method has important limitations. CT and MRI have the advantage of being non-invasive but require large and very expensive equipment. For CT the radiation dose must be considered to avoid tissue damage due to harmful x-rays. It is also uncertain if the resolution is good enough to detect a small plaque with a size on the order of 1 mm. State of the art equipment report a resolution of 0.4 mm (e.g.

Further author information: (Send correspondence to Magnus B. Lilledahl)
Magnus B. Lilledahl: E-mail: magnus.b.lilledahl@iet.ntnu.no, Telephone: +47 73591471

the Siemens Somatron CT Scanner). IVUS is invasive but uses a fairly standard procedure (often classified as minimally invasive). The problem with this method is partially that the resolution might not be good enough to resolve small plaques and that the difference in acoustic wave impedance between healthy and atherosclerotic arterial wall might be too small to generate images where they can be differentiated. The experience of the medical personnel interpreting the images is currently very important.

Numerous novel methods are under development. Some of these are reflection spectroscopy, fluorescence measurements (steady state and time resolved), optical coherence tomography, polarization measurements, multiphoton microscopy, intravascular thermography and shear-modulus elastography. In this paper we will further investigate the feasibility of near-infrared reflection spectroscopy and thermography.

Vulnerable plaques are characterized by a large, lipid-rich, core covered by a thin fibrous cap. Due to this characteristic chemical composition, spectroscopy has been proposed as a suitable detection method. Especially the near-infrared region from 900-1400 nm seems promising due to characteristic lipid absorption bands and relatively low blood and water absorption.^{2,3,4} Reflection spectra of human aorta have been collected and analyzed to investigate whether they can be used to determine the physiological structure and composition of the vessel wall as determined from histology.

Another discriminating property of vulnerable plaques is inflammation and proliferation of macrophages. This inflammatory condition leads to a higher metabolic rate which could induce a higher local temperature in the plaque. A temperature map of the artery could therefore give information about the state of the vessel wall. Some studies have been performed which indicate that this is a feasible method.^{5,6} Thermography measurements have been performed on rabbits. The technique has also been analyzed mathematically to find an estimate on the signal that can be expected.

2. MATERIALS AND METHODS

2.1. Reflectance measurements

2.1.1. Materials

Eight samples of human aorta were collected from eight different autopsies. Measurements were performed within 24 hours of death. The samples consisted of an approximately 10 cm long section of the thoracic aorta which was excised and opened longitudinally. After excision the specimen was placed in phosphate buffered saline (PBS). Measurements began up to a few hours after autopsy. A total of 28 measurements were collected (1-7 measurements on each sample). Before measurements the sample was put on black cardboard. During the experiment the tissue was kept moist by dripping PBS on the sample with a pipette between each measurement. Just before placing the measurement probe on the sample, the surface was dried lightly with paper towels. Some of the tissue surrounding the outside of the aorta was left intact making the samples on average about 5 mm thick.

2.1.2. Method and apparatus

Reflection spectra were collected in the wavelength range 900-1700 nm using an Ocean Optics NIR512 spectrometer (Ocean Optics B.V., Duiven, The Netherlands. www.oceanoptics.com). Three different reflection probes were used. Firstly, an integrating sphere (Ocean Optics ISP-REF) was used to measure the total diffuse reflectance. Secondly, a fiber reflection probe (Ocean Optics R400-7-VIS/NIR) with six excitation fibers placed in a tight circle around a centered collection fiber (see Fig. 1) was used. The fiber core diameters were 400 μm . Thirdly, a probe with 4 fibers (270 μm fiber core diameter) placed linearly with equal spacing (about 300 μm) between each fiber was used (Ocean Optics, custom design. See Fig. 1). Each fiber in this probe had a separate SMA-connector on the other end. Measurements were collected with the fiber closest to the edge of the probe as the excitation fiber and then in turn using each of the three other fibers as the collection fiber. A tungsten-halogen lamp (Ocean Optics LS-1) was used as light source for the fiber probes. The integrating sphere had a built-in tungsten-halogen lamp.

The spectra were recorded as reflected intensity relative to a reference reflectance spectrum measured on a diffuse reflectance standard with a reflectivity greater than 99% (LabSphere, North Sutton, UK. www.labsphere.com).

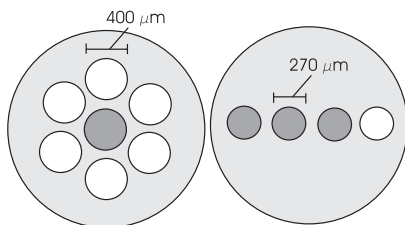


Figure 1. Simple illustration of the tip of the two fiber reflection probes that were used. The white circles represent excitation fibers and grey circles the fibers used for collecting the reflected light

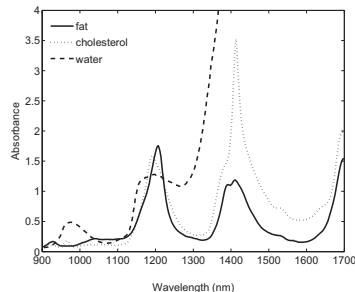


Figure 2. In the figure is a plot of the absorbance of the substances used in the modeling. The absorbance A is defined as $A = -\log_{10}(\mu_a l)$. The given values are for a path length l of 10 mm, so that the absorption coefficient can be calculate from the equation $\mu_a = 10^{A-1} [mm^{-1}]$. The values correspond to measurements on pure substances in liquid phase.

$$R(\lambda) = \frac{I_{meas}(\lambda)}{I_{ref}(\lambda)} \quad (1)$$

The sphere was put directly on the standard when acquiring the reference spectrum. The end of the probes were positioned 1 cm away from the reflectance standard when acquiring the reference spectrum. The tip of the probe was inserted into a cylinder so that the space between the probe tip and standard was shielded from ambient stray-light. The interior of the cylinder was painted with black paint.

2.1.3. Histology

After collecting the spectrum, a tissue sample about 4 mm wide and 15 mm long, centered on the measurement point, was cut out with a surgical knife. This was again divided longitudinally and one piece was fixed in formalin. After paraffin embedding thin sections were cut from the sample and stained with hematoxylin-eosin (HES). The thin sections were then photographed under a microscope and the total plaque thickness was determined by comparison with a similar microphotograph of a measurement stick. Total plaque thickness was defined as the distance from the lumen to the beginning of the tunica media.

2.2. Modelling

To determine the expected change in a spectrum due to changes in plaque composition, a three-layer model based on the diffusion approximation was used to model the plaque.⁷ The top layer represents the fibrous cap of the plaque, the middle layer the lipid core and the bottom layer the rest of the vessel wall. The anisotropy factor was set to $g = 0.9$ and the scattering coefficient was modeled as $\mu_s(\lambda) = 20.2mm^{-1} + \lambda \cdot 2.3mm^{-1}/\mu m$ for all the layers. The coefficients were determined by fitting a linear function to the reported values of μ_s at 1030 nm and 1064 nm.⁸ Due to the varying sizes of scatterers in the tissue, the scattering coefficient is probably a complex function of wavelength. By choosing a linear function it is assumed that most of the scatterers are small compared to the wavelength so that the linear function is a good approximation of the tail of the function describing Rayleigh scattering which is proportional to λ^{-4} . The only absorbers included were water and lipids. The absorbance of water in the three layers were set to 60 % of pure water absorbance and in the middle layer the lipid absorbance was added as 40 % of pure liquid fat. The absorbance spectra of water, fat and cholesterol is shown in Fig. 2. The absorbance of water was taken from published values.⁹ The spectrum of cholesterol was measured by melting cholesterol powder from sheep wool (Sigma-Aldrich, US. C 8503) in a quartz cuvette and

subsequently measuring the absorbance using the same NIR spectrometer which was used for the reflectance measurements. The spectrum of fat was acquired by grinding and melting porcine fat which was subsequently centrifuged and the absorbance measured in the same spectrometer. The ISS-UV-VIS integrated sampling system from Ocean Optics was used as cuvette holder and light source.

2.3. Thermographic measurements

Thermographic measurements were performed on three WHHL rabbits and one NZW rabbit, all aged 6-18 months. A thermistor-based temperature sensor (Medispec, Greece) was used. During anesthesia the sensor was inserted in the femoral artery and advanced approximately to the aortic arch. Pull-back was then performed and temperature was recorded at points with 1 mm to 5 mm increments. The rabbits were put to death while still under general anesthesia. The aorta was then excised and further processed for paraffin embedding and histological investigation.

3. ANALYSIS AND RESULTS

3.1. Reflectance measurements

3.1.1. Analysis

To estimate the detectability of lipids in a plaque, the measure that will have the highest sensitivity and robustness against variations in other optical parameters of the tissue must be determined. In other works this has been done using statistical methods.^{3,4} A more analytic approach, however, will yield better insight into the problem. By trying to understand the underlying physical properties that influence the measurement, it can be determined whether the measured signal will be strong enough to be detected and how changing physiological parameters will affect the measurement. In the wavelength region we have measured there are three lipid absorption peaks located at 930 nm, 1209 nm and 1410 nm (Fig. 2). In the collected spectra only the peak at 1209 nm and possibly the cholesterol peak at 1190 nm have been visible (Fig. 3). The peak at 930 nm is too weak and the peak at 1410 nm is obscured by the large water absorption at 1450 nm. Other groups have reported changes in the reflection spectra in the spectral region at approximately 1700 nm where the water absorption has a local minimum³. The absorption coefficient of water is about 10 times higher at this wavelength than at 1200 nm: $\mu_a(1200nm) \approx 0.1mm^{-1}$, $\mu_a(1700nm) \approx 1mm^{-1}$. An expression for the penetration depth based on the diffusion equation is,¹⁰

$$\delta = \frac{1}{\sqrt{3\mu_a\mu'_{s,r}}} \quad (2)$$

Setting the reduced scattering coefficient to $\mu_{s,r} = 3mm^{-1}$, this yields $\delta(1200nm) \approx 1mm$ and $\delta(1700nm) \approx 0.3mm$. 300 μm is probably too shallow a penetration depth to yield good information about the plaque.¹¹ The diffusion approximation is only accurate if the scattering coefficient is much larger than the absorption coefficient. The model is thus close to the limit of its validity when the absorption is as high as $1mm^{-1}$. This might perturb the above considerations to some degree but the conclusion is unlikely to change.

Having concluded that the lipid absorption peak at 1209 nm is the best candidate for measuring the lipid content it remains to be determined how to best extract this information. There is strong water absorption in this region (maximum at 1190 nm) making it difficult to extract the spectral change that is due to the lipid absorption only. Two important problems must be overcome. Firstly, changes in the scattering properties change the overall reflectance level of the spectrum. These properties vary from person to person, with age and also from plaque to plaque. Secondly, changes in the water concentration or the path the photons travel on average in the medium (which again is related to scattering properties) changes the water absorption level.

The following analysis is an attempt to design a measure that will calibrate for these effects. To correct for the level of water absorption a straight line that crosses the reflection spectrum at $\lambda_1 = 1190nm$ and $\lambda_2 = 1250nm$ is calculated (water has a local absorption minimum at 1250 nm),

$$y = \frac{R(\lambda_2) - R(\lambda_1)}{\lambda_2 - \lambda_1}x + R(\lambda_1) - \frac{R(\lambda_2) - R(\lambda_1)}{\lambda_2 - \lambda_1}\lambda_1 \quad (3)$$

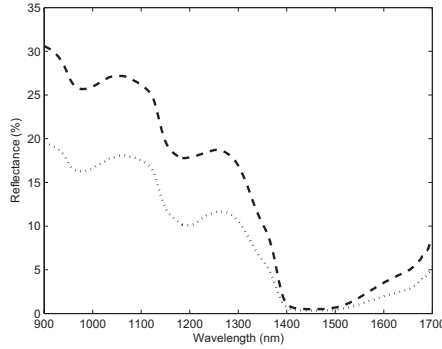


Figure 3. Reflection from healthy and atherosclerotic arteries. The dotted graph is from an atherosclerotic artery and the dashed graph from a healthy one. The absorption maximum (reflection minimum) at 1200 nm can be seen to be shifted towards higher wavelengths. Wavelength in nm on the x-axis and reflection level in percent on the y-axis.

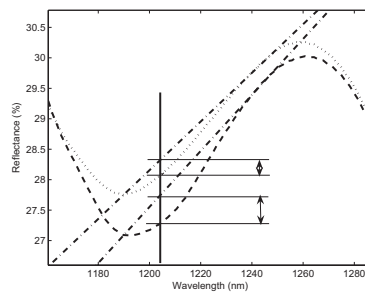


Figure 4. Illustration of the calculation of lipid-index described in Eq. (4). On the x-axis is the wavelength in nanometers and on the y-axis is the reflection level in percent. The dotted graph is the reflectance measurement of a healthy artery and the dashed line from an atherosclerotic artery. The dash-dot lines are the linear functions which are fitted to the values at 1190 nm and 1250 nm. The vertical, double headed arrows graphically illustrates the lipid-index measure.

This effectively gives the depth of the water absorption. This function is then evaluated at 1209 nm and the actual reflection level at 1209 nm is subtracted. Subtracting two closely spaced values also corrects for the overall reflectance level of the spectrum. This results in the following measure which can serve as a *lipid-index*, M of the plaque.

$$M_{lipid} = \frac{R_{1190} - R_{1250}}{60nm} 1209nm - R_{1190} - \frac{R_{1190} - R_{1250}}{60nm} 1190nm - R_{1209} \quad (4)$$

This measure should to a certain degree correct for variations in tissue parameters which are not related to the lipid content. The calculation is illustrated in Fig. 4. If the lipid absorption is small this measure will be small and increase with increasing amount of lipid in the plaque.

3.1.2. Measurement results

The measure was compared with plaque thickness which was obtained from formalin fixed, HES stained histology. None of the probes yielded results where a tendency that the lipid index M (Eq. (4)) increased with increasing

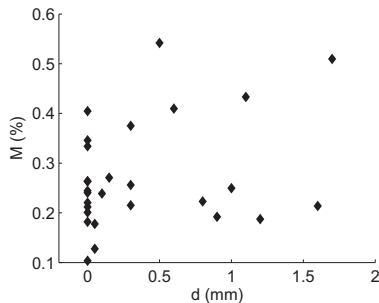


Figure 5. On the x-axis is the thickness of the plaque, determined from histology. This was determined by comparing histological photographs with photographs of a measurement stick. On the y-axis is the lipid-index defined in Eq. (4) using the integrating sphere to collect the reflected light.

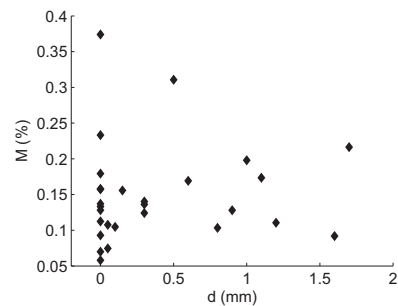


Figure 6. Same as Fig. 5 but using the fiber probe on the right in Fig. 1 with the fiber second from the left as the collection fiber. This gives a fiber separation of about 600 μm .

plaque thickness. (Fig. 5). Only the results for the integrating sphere and the fiber probe on the right of Fig. 1 is shown but the other probes gave similar results.

3.1.3. Modelling

Parameters from histological samples were used in the mathematical model and can be seen to agree fairly well with the measured spectrum (Fig. 7). The model was used to predict the estimated change in the spectrum due to changes in the plaque geometry. In Fig. 8 is a plot of the lipid index versus plaque core thickness and cap thickness.

3.2. Thermographic measurements

An example of a temperature measurement is shown in Fig. 9. No significant variation that correlated well with the locations of plaque, was found. The locations of plaques were determined from macroscopic photographs. Local variations were only on the order of 0.01°C. Larger, global variations were most likely due to changes in systemic temperature.

4. DISCUSSION

4.1. Reflection measurements

The poor correlation between plaque thickness and lipid-index could be due to the fact that plaques might be either lipid-rich or mainly fibrous. A histological study which can determine the amount of lipid in the plaque (e.g. staining frozen sections with sudan red) might correlate better with the measured spectra.

Since plaques often appear as white areas in the artery, another possible measure of plaque index could be the reflectance level. This, however, is a poor measure of vulnerability as both stable fibrous plaque and unstable lipid-rich plaque would increase the reflection. Both the higher collagen content in the fibrous cap and the lipid droplets in the plaque core are strong scatterers. The scattering properties of a vessel varies from person to person so that any detection measurement must be relative to a measurement of a healthy vessel. This large variation from patient to patient makes it difficult to create a detection measure based on statistical analysis (e.g. principal component analysis).

The changes in the measured spectra are small even for a fairly large plaque(1-2 mm). This leaves very little room for noise which will be a factor in an actual experiment. Since the signal due to the lipid is fairly small it is uncertain if it is detectable. Future studies need to determine quantitatively the spectral changes variation

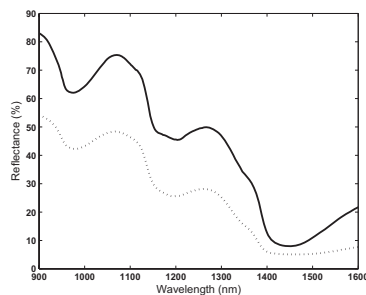


Figure 7. A comparison of the modeled spectra (solid line) with a measured spectrum (dashed line) taken with an integrating sphere. The model used is the three layer model described in Sect. 2.2. The top and middle layer are both $500 \mu\text{m}$. The absorption coefficient in the top and bottom layer is 60 % of pure water. In the middle layer the absorption coefficient is the sum of 40 % pure water and 30 % pure liquid lipid. The reason that the measured spectrum is lower is probably due to the fact that the reference spectrum was taken on a standard where the penetration depth is practically zero. When measuring on the tissue sample some light will be lost at the edges of the aperture, effectively reducing the light intensity inside the sphere. The measurement spectrum is of a fairly large plaque.

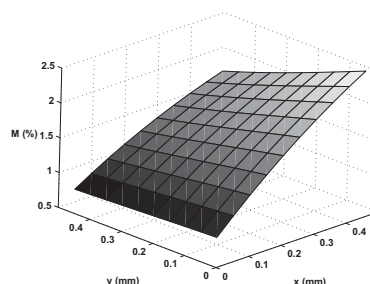


Figure 8. On the x-axis is the thickness of the lipid layer in the model and on the y-axis is the thickness of the fibrous cap. The unit is in millimeters. In the upper and bottom layer the absorption coefficient is set to 60 % of pure water absorption. In the middle layer the absorption coefficient is the sum of 40 % of water absorption and 30 % of liquid lipid absorption (as shown in Fig. 2). On the z-axis is the value of the lipid-index defined by Eq. (4) determined from the modeled spectra. The reason that the values of M are higher here than in Fig. 5 and Fig. 6 is that absorption features become more pronounced when the reflection level is higher (see Fig. 7)

in tissue properties might cause. The noise that will be present in the system and variations that are caused by different measuring conditions, e.g. the contact with the tissue surface, must also be considered. It is also uncertain if the lipid-measure presented is optimal. This needs to be investigated further.

Another important issue that must be explored is the effect of the tissue surrounding the artery. In the coronary arteries the plaque size might be on the order of the thickness of the vessel wall. The tissue outside the artery might thus influence the measured spectra. Since this also might contain lipids it may have an important impact on the measured spectrum.

4.2. Thermographic measurements

No local temperature variations that correlated well with the histological studies were found. A simple computation shows that a 1 mm diameter plaque theoretically should maximally give about 0.02°C change in temperature. To get a temperature change about 1°C , the heat producing object must have a size on the order of centimeters (see App. A). The theoretical estimates and measurements for thermography do not make this a good candidate for detecting plaques. The reported measurements of up to 1°C temperature variation could be due to nearby organs (heart, lungs, liver) that could possibly induce temperature variations of this magnitude.⁶ Detecting a plaque that only changes the temperature by 0.02°C against this background will be difficult.

To estimate the temperature variation, a value for the metabolic rate that can be expected needs to be found. A study of the heat production in macrophages gives a value of about 20 pW/cell.¹² The heat production per volume of tissue dense with macrophages can then be calculated. The size of monocytes is reported as $20 \mu\text{m}$ in diameter.¹³ The size of macrophages is larger than this so this represents a conservative estimate. Rounding off to get manageable numbers the volume of a macrophage can be found to be,

$$V_{mp} = 4\pi r^3 = 4\pi \cdot (10\mu\text{m})^3 \approx 10^4 \mu\text{m}^3 \quad (5)$$

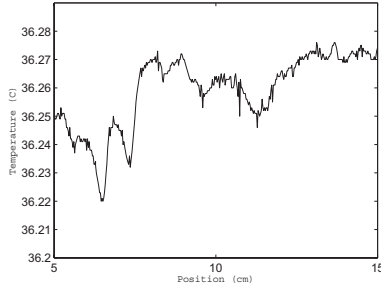


Figure 9. Temperature in rabbit aorta as a function of position.

The heat production per cubic millimeter is then

$$\frac{20pW}{cell} \cdot \frac{1mm^3}{10^4\mu m^3/cell} = 2\mu W \quad (6)$$

A rule of thumb for the heat production in the human body is 100 W/body. Assuming that the body is about $0.1m^3$ and that about 50 % of the body consists of metabolizing tissue this gives $2 \mu W/mm^3$, which is the same result as in Eq. (6) Thus, assuming that the metabolism in the plaque due to macrophage infiltration is significantly elevated seems unlikely. A study based on the finite element method reported that a $0.4 W/mm^3$ was needed to achieve the often reported $1^\circ C$ temperature difference between healthy and atherosclerotic vessel wall.¹⁵ This is a factor 10^5 above normal metabolism and seems very unlikely to be the case. Assuming 10 times normal metabolism yields a temperature difference of $0.01^\circ C$ between the healthy and the atherosclerotic wall.

4.3. Conclusion and future work

Based on the analysis in this paper it can be concluded that thermography is not a good method for detecting vulnerable plaque. No conclusions about NIRS can be drawn from the results in this article. Future work need to compare spectra with histological studies that can determine the lipid content in the plaque. The lipid-index presented in this paper can probably be improved and this must be investigated further. Also, to determine the robustness of the method, the natural variability in composition between vulnerable plaque and how this affect the measured spectrum must be studied.

APPENDIX A. THERMAL HETEROGENITY IN PLAQUE

Let a small sphere with diameter $r = a$ be embedded in an infinite medium. The sphere represents the heat producing plaque and the medium the tissue surrounding it. Blood flow in the vessel and perfusion in the vasa vasorum have been neglected as these will only reduce ΔT even more.^{14,15} The temperature is normalized so that $0^\circ C$ actually represents the normal body temperature of $37^\circ C$. The heat generation was set to $10^4 W/m^3$. This value was derived by assuming that the human body generates about 100 W and taking 1 W/kg as the average heat generation in the body and multiplying this by 10 due to the higher metabolism.

We then solve the stationary heat equation in spherical coordinates. In the heat producing sphere the equation becomes Poisson's equation,

$$\frac{1}{r} \frac{\partial^2}{\partial r^2}(rT) = -\frac{q}{\kappa} \quad (7)$$

and in the region surrounding the sphere there are no sources and the heat equation becomes Laplace's equation

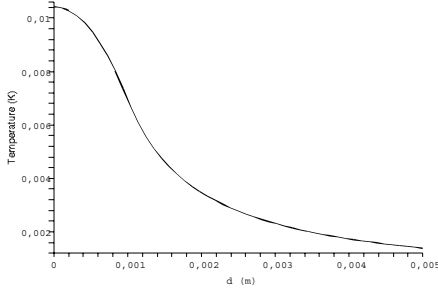


Figure 10. Temperature due to a sphere with radius 1 mm producing a heat of 10^4 W/m^3 embedded in an infinite medium. ΔT in $^\circ\text{C}$ on the y-axis and distance from the center of the sphere in meters on the x-axis.

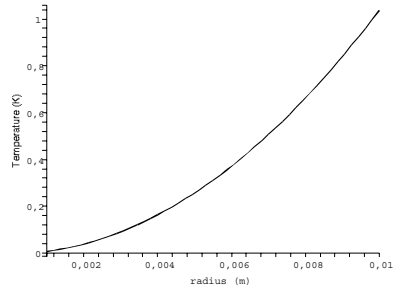


Figure 11. Temperature at the surface of a sphere embedded in an infinite medium as a function of the radius of the sphere.

$$\frac{1}{r} \frac{\partial^2}{\partial r^2} (rT) = 0 \quad (8)$$

We then solve these equations with the boundary conditions that the heat flow is zero at $r = 0$, that the temperature and heat flow are continuous at the boundary between the two regions and that $T(r \rightarrow \infty) = 0$.

The solution for the two regions are then,

$$T_1(r) = -\frac{q}{6\kappa} (r^2 - 3a^2) \quad (9)$$

$$T_2(r) = \frac{qa^3}{3\kappa r} \quad (10)$$

These solutions with $a = 1 \text{ mm}$ and $\kappa = 0.48 \text{ W/m} \cdot \text{K}$ are plotted in Fig. 10. From the graph it can be seen that 1 mm from the surface of the sphere (which can represent the top of the cap of the plaque) $\Delta T = 0.005^\circ\text{C}$. The cooling effect of blood flow and perfusion will reduce this value even more. This is too low a temperature to be measured with confidence and accuracy in the turbulent environment of the coronary artery. To achieve a temperature difference of 1°C at the surface the heat producing object must have a radius of 1 cm (Fig. 11). This means that large organs (heart, lungs, liver) around the aorta could give temperature fluctuations which have been reported in the literature. All these estimates are conservative as the cooling effect of the blood has not been taken into account.

To allow for more general geometries and present an upper bound on the temperature that can be expected at the surface, a Green's function calculation was also performed. One proposed design for a thermal probe thermally insulates the surface from the blood stream. To model this, we have the Green's function for a semi-infinite solid ($z > 0$) with no flow of heat across the surface is*,

$$G = \frac{1}{4\pi\sqrt{(x-\zeta)^2 + (y-\eta)^2 + (z-\xi)^2}} + \frac{1}{4\pi\sqrt{(x-\zeta)^2 + (y-\eta)^2 + (z+\xi)^2}} \quad (11)$$

The temperature at the surface of the solid was then determined by the integral,

*The Green's function was found using a mirror-image method. A mirror image of the source about the $z = 0$ plane makes the gradient at the $z = 0$ plane equal to zero so that there is no flow of heat across this plane.

$$T(x, y, z) = \int_V G \frac{\rho(\zeta, \eta, \xi)}{\kappa} d\zeta d\eta d\xi \quad (12)$$

where the integral is taken over the region where the heat production ρ is non-zero. The integral was evaluated using Maple (Maplesoft. Waterloo, Canada. www.maplesoft.com) for a plaque with a volume of 2 mm x 4 mm x 4 mm. The resulting surface temperature was 0.037°C.

ACKNOWLEDGMENTS

This work is part of a project funded by the Norwegian Research Council and has been approved by the Norwegian Committee on Ethics in Medical Research. Participation, comments and help from the following people are greatly appreciated: Marianne Barkost, Unn Granli, Eivind La Puebla Larsen and Dag Roar Hjelme.

REFERENCES

1. H. C. Stary, A. B. Chandler, R. E. Dinsmore, V. Fuster, S. Glagov, I. William, M. E. Rosenfeld, C. J. Schwartz, W. D. Wagner, and R. W. Wissler, "A definition of advanced types of atherosclerotic lesions and a histological classification of atherosclerosis", *Circulation* **92**, pp. 1355–1374, 1995.
2. W. Jaross, V. Neumeister, P. Lattke, and D. Schuh, "Determination of cholesterol in atherosclerotic plaques using near infrared diffuse reflection spectroscopy", *Atherosclerosis* **47**, pp. 327–337, 1999.
3. P. R. Moreno, R. A. Lodder, R. Purushotaman, W. E. Charash, W. N. O'Connor, and J. E. Muller, "Detection of lipid pool, thin fibrous cap and inflammatory cells in human aortic atherosclerotic plaques by near-infrared spectroscopy", *Circulation* **105**, pp. 923–927, 2002.
4. J. Wang, Y. Geng, B. Guo, T. Klima, B. N. Lal, J. T. Willerson, and W. Casscells, "Near-infrared spectroscopic characterization of human advanced atherosclerotic plaque", *Atherosclerosis* **39**, pp. 1305–1313, 2002.
5. W. Casscells, M. Hathorn, David, T. Krabach, W. K. Vaughn, H. A. McAllister, G. Bearman, and J. T. Willerson, "Thermal detection of cellular infiltrates in living atherosclerotic plaques: Possible implications for plaque rupture and thrombosis", *The Lancet* **347**, pp. 1447–1449, 1996.
6. C. Stefanadis, "Increased local temperature in human coronary atherosclerotic plaques: An independent predictor of clinical outcome in patients undergoing a percutaneous coronary intervention", *Journal of the American College of Cardiology* **37**, pp. 1277–1283, 2001.
7. L. O. Svaasand, L. T. Norvang, E. J. Fiskerstrand, E. K. S. Stopps, M. W. Berns, and J. S. Nelson, "Tissue parameters determining the visual appearance of normal skin and port-wine stains", *Lasers in Medical Science* **10**, pp. 55–65, 1995.
8. M. Essenpreis, *Thermally induced changes in optical properties of biological tissues*. PhD thesis, London College, 1992.
9. K. F. Palmer and W. Williams, "Optical properties of water in the near infrared", *Journal of the Optical Society of America* **64**, pp. 1107–1110, 1974.
10. R. C. Haskell, L. O. Svaasand, T. Tsay, T. Feng, M. S. McAdams, and B. J. Tromberg, "Boundary conditions for the diffusion equation in radiative transfer", *Journal of the Optical Society of America A* **11**, pp. 2727–2741, 1994.
11. W. Cheong, S. A. Prael, and A. J. Welch, "A review of the optical properties of biological tissues", *IEEE Journal of Quantum Electronics* **26**, pp. 2166–2185, 1990.
12. S. A. Thoren, M. Monti, and B. Holma, "Heat conduction microcalorimetry of overall metabolism in rabbit alveolar macrophages in monolayer and in suspensions", *Biochimica et Biophysica Acta* **1033**, pp. 305–310, 1990.
13. G. Tortora, *Principles of Anatomy and Physiology*, Wiley, 2003.
14. C. Stefanadis, K. Toutouzas, E. Tsiamis, I. Mitropoulos, C. Tsioufis, I. Kallikazaros, and C. Pitsavos, "Thermal heterogeneity in stable human coronary atherosclerotic plaque is underestimated in vivo: The 'cooling effect' of blood flow", *Physics in Medicine and Biology* **49**, pp. 4447–4462, 2004.

15. A. G. ten Have, F. Gijsen, J. Wentzel, C. Slager, and A. F. W. van der Steen, "Temperature distribution in atherosclerotic coronary arteries: Influence of plaque geometry and flow (a numerical study)", *Physics in Medicine and Biology* **49**, pp. 4447–4462, 2004.

Paper II

The effect of a thin bloodlayer on fluorescence spectroscopy

Magnus B. Lilledahl, Marianne Barkost, Mari W. Gran, Olav A. Haugen and Lars O. Svaasand. *Proceedings of SPIE, vol. 6078, 60782J-1 (2006)*

Effect of a thin blood layer on fluorescence spectroscopy

Magnus B. Lilledahl^a, Marianne Barkost^a, Mari Warløs Gran^a, Olav A. Haugen^{b,c} and Lars O. Svaasand^a

^aNorwegian University of Science and Technology, Department of electronics and telecommunications, O.S Bragstads plass 2A, 7049 Trondheim, Norway;

^bNorwegian University of Science and Technology, Department of Laboratory Medicine, Children's and Women's Health, Olav Kyrres gate 17, 7006 Trondheim, Norway;

^cSt.Olavs Hospital, Department of Pathology and Medical Genetics, Olav Kyrres gate 17, 7006 Trondheim, Norway.

1. ABSTRACT

When performing intravascular spectroscopy there is always the possibility that there will be a thin layer of blood between the probe and the vessel wall. This will affect measurements especially below 600 nm where blood absorption is strong (important for fluorescence and Raman measurements) and above 1400 nm where the water absorption is strong. Between these two regions (the therapeutic window) the absorption is fairly low and can be neglected. This article explores the possibility of performing measurements outside the optical window by minimizing blood layer and increasing the excitation signal.

Keywords: Fluorescence spectroscopy, atherosclerosis, intravascular, blood layer

2. INTRODUCTION

In recent years the paradigm has emerged that it is not the degree of stenosis but rather the composition of the arterial plaque which determines the risk of an acute coronary event. Plaque which are composed of a thick, necrotic, lipid-rich core, covered by a thin fibrous cap are typically prone to rupture and are thus denoted as *vulnerable plaques*.

Current non-invasive detection modalities (CT, MRI) are mainly effective at determining the geometry of the plaque, that is, the degree of stenosis, but is limited in determining the actual chemical and physiological composition. To determine the composition it might be necessary to perform an intravascular measurement of the plaques. Several optical methods have been proposed for intravascular spectroscopy: near infrared (NIR) reflection spectroscopy, fluorescence spectroscopy and Raman spectroscopy. This work mainly deals with the effect of a blood layer on fluorescence spectroscopy.

Probably the earliest work in the field of fluorescence spectroscopy of atherosclerotic plaques was by Blankenhorn in 1957 which measured the fluorescence of various types of plaques and compared this to the presence of various chromophores, especially carotenoids.¹ Several studies have later confirmed these findings²⁻⁶ Filipidies used double wavelength excitation of fluorescence to improve the detection of various types of plaque.⁷ A review of the field was given by Papazoglou in 1995.⁸

Most of the published studies investigating the possible uses of optical methods in plaque classification have been in-vitro studies except one study performed in rabbit aorta.⁹ In the ex-vivo studies there have been no significant amount of blood present in the experiments. Since blood could have an interfering effect on the measurements, effectively as noise and reduction of signal level, conclusions on the feasibility of the methods based on ex-vivo studies might need to be modified. In the in-vivo study in a rabbit model they were able to differentiate between various types of atherosclerotic lesions using both the lifetime and fluorescence intensity

Further author information: (Send correspondence to Magnus Lilledahl.)

Magnus B. Lilledahl: E-mail: magnus.b.lilledahl@iet.ntnu.no, Telephone: +47 73591471

Photonic Therapeutics and Diagnostics II, edited by N. Kollias, H. Zeng, B. Choi, R. S. Malek, B. J.-F. Wong, J. F. R. Ilgner, E. A. Trowers, W. T.W. de Riese, H. Hirschberg, S. J. Madsen, M. D. Lucroy, L. P. Tate, K. W. Gregory, G. J. Tearney, Proc. of SPIE Vol. 6078, 60782J, (2006) · 1605-7422/06/\$15 · doi: 10.1117/12.645965

of the signal.⁹ They avoided the interference of blood by saline irrigation and clamping of arteries during measurement.

There are several techniques for removing or correcting for the effect of a blood layer between the probe and the vessel wall. Flushing the vessel with saline is possible but how effective this removes the blood has to our knowledge not been investigated. Constant irrigation or blocking of the artery could put too much of a burden on the heart to be clinically safe. Lin et al. investigated the feasibility of optical spectroscopy in the presence of blood.¹⁰ Using signal processing methods they improved the detection of the fluorescence signal. Fluorescence lifetime measurements have also been shown to be independent of an interfering blood layer.^{11,12}

The goal of the present work is to gain an understanding of how a blood layer can adversely affect an optical measurement which seeks to determine the composition of atherosclerotic plaques. Firstly it is investigated how variation in the signal due to a varying layer of blood will affect the differentiation of various types of plaque based on fluorescence spectroscopy. Secondly, it is considered how the temperature rise in a thin layer of blood will limit the allowed irradiation intensity.

Section 3 gives a description of measurements performed: 3.1 gives a description of fluorescent measurements on human plaques in the aorta, measured ex-vivo. 3.2 gives a description of measurements performed on a fluorescent tissue phantom through a layer of blood with various thickness. In 3.4 are some calculations on theoretically expected values on heat generation in blood due to light absorption and in 3.3 are models on the signal reduction due to the blood layer.

3. MATERIALS AND METHODS

3.1. Fluorescence measurements of plaque

A section of the thoracic aorta was excised during autopsy from 21 patients. The work was approved by the Norwegian Board on Ethics in Medicine. The samples were opened longitudinally and fluorescent measurements were performed on various locations, which from visual inspection appeared to be in various pathological states. The same samples were used for another study and a more complete description of the samples and their handling is given there.¹³

The fluorescence measurements were performed with an optical fiber probe. The probe consisted of four 270 μm optical fibers which were inserted in four equally spaced holes, drilled in the tip of an SMA fiber connector (Ocean Optics, Duiven, The Netherlands. Custom design). The distance between the centers of two adjacent fibers was about 500 μm . Only two adjacent fibers were used, one for the excitation light and one for collection of fluorescent light. On the other end, each of the fibers were terminated in separate SMA connectors. A blue LED source at 470 nm (Ocean Optics, LS450), delivering about 10 μW into the fiber, was used as the excitation light and a fiber optic spectrometer (SD2000, Ocean Optics) was used to measure the collected light.

The measurement sites were cut out in pieces roughly 4x10 mm. These were again divided in two with one of the slices being frozen in liquid nitrogen and the other fixated in formalin. The sections were then sliced and stained for histology, one with Hemotoxylin-Eosin-Safron and the other with Sudan Red. From the histology the thickness of the lipid pool and the fibrous cap were found and the pathological classification were determined.

3.2. Fluorescence measurements of phantom through blood

Small fluorescent tissue phantoms approximately 1 cm thick and 1 cm in diameter were prepared in cylindrical steel cups using a mixture of agar, intralipid and fluorescein. The agar was made from 3.1 g of agar (Sigma-Aldrich, agar-agar, A7002) dissolved in 210 ml of water. 150 μl of intralipid solution (200 mg/l, Fresenius Kabi, Uppsala, Sweden) was then added to 10 ml of the agar/water mixture. Various amounts (100-500 μl) of a fluorescein (fluorescein sodium salt, 67844, Sigma-Aldrich)/water solution (73 mg/l) were then added to 10 ml of the agar/intralipid mixture. This mixture was then poured into the steel cylinders while still hot and left to solidify at room temperature covered with plastic film to avoid water evaporation.

The same equipment that was used for the measurements of the fluorescence of the aorta was used for the measurements on the tissue phantoms. The fiber optic probe was positioned just at the surface of the sample with a stand that could be adjusted up and down using a micrometer positioning system. A fluorescent spectrum

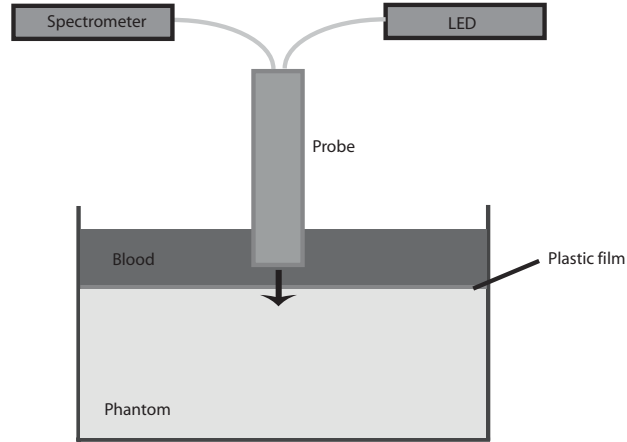


Figure 1. A schematic illustration of the measurement of fluorescence from a tissue phantom through a layer of blood.

was collected, excited by the 470 nm LED. The measurements were performed in a dark room to avoid affects of stray light. The probe was then lifted without loosing the height reference to the phantom and a plastic film was put on the phantom, assuring that it clung thightly to the surface. This was done to avoid that blood diffused into the phantom, which it otherwise did quite rapidly. A small amount of blood (red blood cells in Sagman solution, hematocrit \approx 40%) was then added on top of this film (see Fig. 1). The probe was then lowered towards the phantom, using the positioning screw, through the layer of blood and the reflected spectra were recorded at various heights. In the end the plastic film and blood was removed and another measurement was performed on the top of the phantom surface.

3.3. Optical models

To model theoretically the reduction in signal due to a thin bloodlayer a simple one dimensional model was used. The signal reduction is then given by

$$I(x) = I_0 \exp(-(\mu_{a,470} + \mu'_{s,470} + \mu_{a,518} + \mu'_{s,518})x) \quad (1)$$

470 nm was the excitation wavelength of the LED and 518 nm is the emission maximum of fluorescein. The absorption coefficient μ_a was taken as 4.74 mm^{-1} and 4.02 mm^{-1} at 470 nm and 518 nm respectively* and the reduced scattering coefficient μ'_s as 20 mm^{-1} as a mean value of various values reported, was used for both wavelengths.¹⁴ The reduced scattering is used since it seems unreasonable to assume that every scattering event will remove the scattered light from the measured region. The light that is absorbed in the blood layer is given by,

$$I_0 (1 - \exp(-\mu_{a,470}x)) \quad (2)$$

if one assumes that the light absorbed from the reflected light is negligible compared to what is absorbed from the incident light. This is valid if the thickness of the blood layer is at least two penetration depths,

$$d = 2\delta = \frac{2}{\mu_t} = \frac{2}{\mu_{a,470} + \mu_{s,470}} \approx 30\mu m. \quad (3)$$

*taken from <http://omlc.orgi.edu/spectra/hemoglobin/summary.html>

3.4. Temperature models

Analytical solutions to the heat diffusion equation quickly becomes unwieldy for complicated geometries so simplifications are necessary to find a manageable solution in terms of familiar functions. Another method is to use numerical methods (FEM analysis), but often the response of the system to changes in variables is less transparent when using this method.

3.4.1. Model 1

As a first approximation one can use a simple model where it is assumed that no heat diffuses out from the irradiated volume during the irradiation (the validity of this will be discussed further down). The temperature change in the volume of blood irradiated by the light will be,

$$\Delta T = \frac{Pt}{\rho cV} (1 - \exp(-\mu_{a,470}x)), \quad (4)$$

where P is the incident power, t is the time of irradiation and ρ and c the density and specific heat of the irradiated volume V.

3.4.2. Model 2

During the absorption process some of the heat will diffuse out of the irradiated area, especially through the probe if it is made of a highly conductive material, e.g. steel. A rule of thumb for the distance d that heat diffuses in a time interval Δt is $d = \sqrt{\chi \Delta t}$ where χ is the diffusivity of the material. Using for steel $\chi_{st} = 1.2 \cdot 10^{-5} \text{ m}^2/\text{s}$ † and for blood $\chi_{st} = 1.5 \cdot 10^{-7} \text{ m}^2/\text{s}$ we find that the diffusion depth during 0.1 s is 1 mm and 0.1 mm respectively which is significant since the volume of the irradiated sample is less than 1 mm³. Hence, a more complicated model must be considered.

A more sophisticated model incorporating this effect is that of a heat generating sphere embedded in a conductive medium. The heat generation in the sphere represents the light absorbed by the blood. By surrounding the sphere both by medium with similar properties as blood/tissue and by steel one can find bounds on the possible temperature increase. The solution to this is given in.¹⁵

However the solution is so complicated that the advantages of an analytical solution is lost and it is more advantageous to use the more flexible finite element method (FEM).

3.4.3. FEM

A FEM structure was analyzed using FEMLAB (Comsol AB, Stockholm, Sweden). The FEM analysis gives more information on how the geometry affects the solution as complicated geometries are very difficult to solve analytically. This consisted of a rectangular region (3x3x0.2 mm) representing the vessel wall, on top of this a rectangular (3x3x0.5 mm) region representing the blood with a smaller cylindrical region ($r = h = 0.5 \text{ mm}$) embedded in the blood representing the irradiated volume and on top of this a rectangular region (3x3x0.5 mm) representing the probe. The model is illustrated in figure 2 The thermal properties that were used in the model was given in the FEMLAB model library. For the probe, the properties of steel AISI 4340 was used. Blood was assumed to have the same thermal properties as water. For the tissue the thermal conductivity was set to $\kappa = 0.4 \text{ W/m}\cdot\text{K}$, the specific heat capacity 2000 J/kg·K and 800 kg/m³ for the density.

4. RESULTS

4.1. Fluorescent spectra of plaque

The measurement sites on the aortas were classified into six pathological classes based on the histology: Normal, fatty streak, fibrous, thin cap fiberoatheroma, calcified and ruptured.¹⁶ Generally atheromas had low fluorescence, normal, fibrous, and fatty streak had fairly similar fluorescence, while calcified plaques had the highest fluorescence.

†from FEMLAB material library

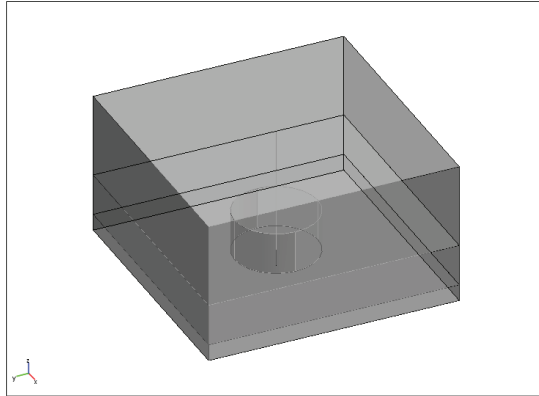


Figure 2. FEM geometry.

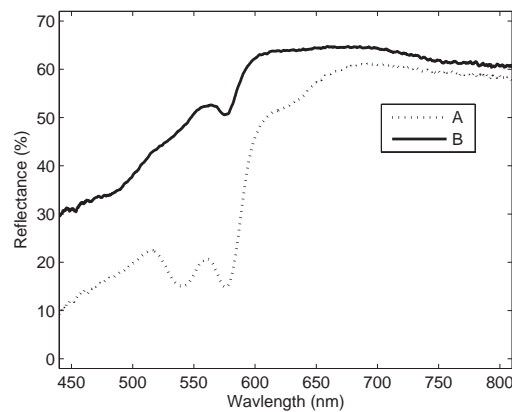


Figure 3. Reflection spectra of a normal area of the vessel wall from two different aortas. The A curve is from a 78 year old male and the B curve from 24 year old male. One can see that there is a large variation in the absorption which will affect how much of the excitation signal that is absorbed. This can be seen as a redder color on visual inspection of the aortas.

However, there were large differences in the general level of fluorescence between various aorta samples. The general color of the aorta varied. The older the person from which the aorta was taken, generally the aorta had a more reddish color. This can be seen in the two absorption spectra in figure 3 which were taken from two different aortas.

In figure 4 is a typical fluorescence spectrum from a single aorta. The spectra indicate that the difference in fluorescence between calcified, fibrous and atheromatous plaques can be differentiated.

In figure 5 is a plot of the mean value of the fluorescence at 560 nm for each of the classifications of plaque from all the aortas with error bars indicating the standard deviation. The fluorescence level of the calcified plaques clearly stand out. The trend in the other classes are masked by the large standard deviation.

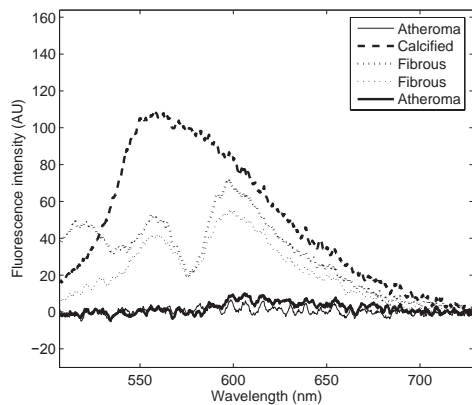


Figure 4. A typical fluorescence spectrum for a single aorta sample with various pathological classification of the measurement sites.

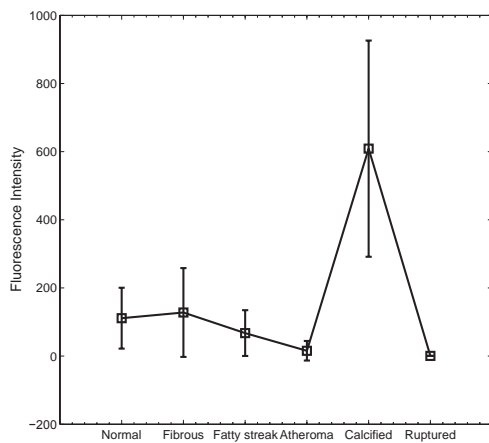


Figure 5. Mean values of the fluorescence for the various pathological conditions for all the aorta samples with error bars indicating the standard deviation.

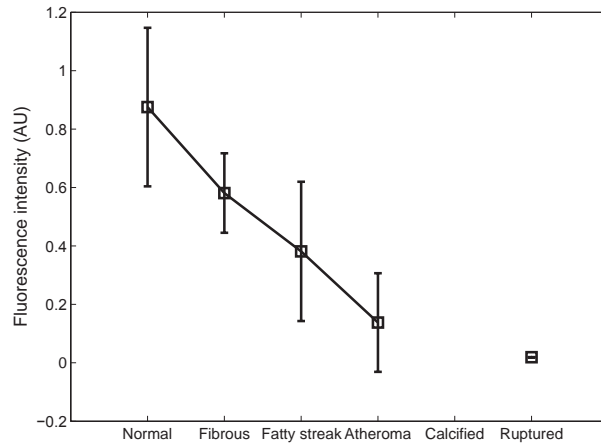


Figure 6. Same as figure 5 but here each spectrum from each aorta has been normalized with the value of the spectrum of normal aorta from the same sample. We can see that the errorbars are smaller and differentiation between various pathological states are better. The sample which had calcified plaques did not have a measurement of normal aorta and is therefore removed from this analysis.

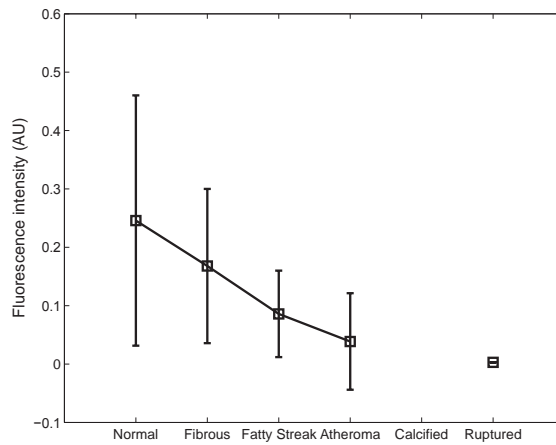


Figure 7. Same as figure 6 but here each spectrum has had a random reduction in signal intensity due to a random layer of blood between 10-100 μm

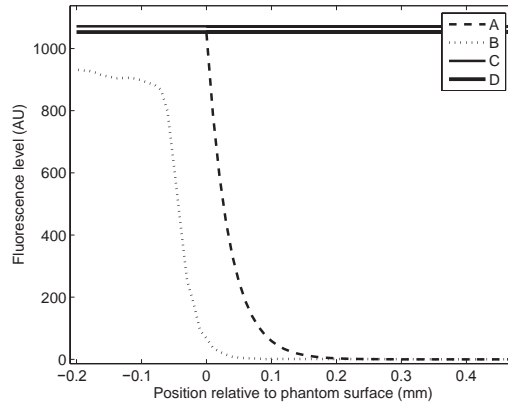


Figure 8. Curve B shows the fluorescence level at 560 nm with varying blood layer between the probe and the tissue phantom, while A shows the corresponding theoretical spectra using the model given in section 3.3. Curve C is the original fluorescence intensity without the blood and plastic film while D is the same after removing the plastic film and the blood.

4.2. Effect of blood layer

In our measurements, the layer of blood masked any signal from the tissue phantom until the probe was about 100 microns from the aorta. In figure 8 is a plot of the measurements on the phantom and the theoretical model described in section 3.3. Except for a shift in position we see that the graphs agree fairly well but that the measured spectra falls off as the probe approaches the phantom surface. All the measurements only got up to about 80-90% of the original fluorescence value when measuring through blood. When the probe was lifted and the plastic film and the blood removed, the original fluorescence level was recovered within a few percent. This reduction in signal level while the blood was present was interpreted as a thin layer of blood between the probe and the surface even when the probe was pressed against the surface. We can estimate this thickness by assuming that the reduction in the signal is given by $exp(-\mu'_s + \mu_a)$. Using the values from section 3.3 we find that the reduction in signal by 10-20% corresponds to a blood layer of 5-10 μm .

4.3. Heat generation in blood

Loss in signal level due to absorption of light in the blood could be compensated by an increase in the power of the excitation signal or using a longer integration time in the detector. There is, however, a limit to both methods. The integration time must be less than the heart's pulse rate as the probe cannot be expected to be kept steady for longer periods of time. An order of magnitude estimate is 0.1 s. At such small times the blood can withstand quite high temperature levels but a 40°C temperature increase is a maximum where cell damage is instantaneous. The probe also needs a certain amount of lateral resolution so in the following calculations it is assumed that the irradiated area covers 1 mm^3 .

The power that can be applied is limited by heating of the blood and the surrounding tissue. At 470 nm the absorption coefficient is 4.7 mm^{-1} . Three times the penetration depth will be 630 μm and at this depth 95% of the incoming light will be absorbed. If precise positioning of the probe inside a vessel is not possible it must be assumed that such a high absorption can occur.

Using material parameters indicated in section 3.4.3 gives that the maximum power that can be delivered in 0.1 s is 1 W, given that the 40 degrees is the maximum allowed temperature increase. In figure 10 is a plot of the temperature increase as a function of blood layer thickness and the power of the incident light using eq. 4. The equation actually approaches a constant as $x \rightarrow 0$ but cannot be expected to be valid when the layer thickness approaches the size of a red blood cell ($\sim 10\mu\text{m}$).

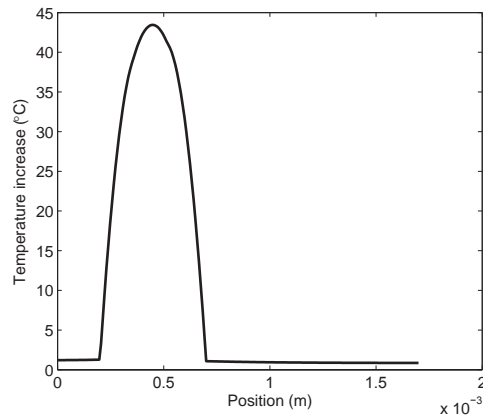


Figure 9. The temperature increase in a blood layer between the probe and the vessel wall using FEM. The probe is located at $0.7 \mu\text{m}$ and the vessel wall at $0.2 \mu\text{m}$. The power irradiated on the area was 1 W during 0.1 s. The irradiated area was a circle with radius $0.5 \mu\text{m}$.

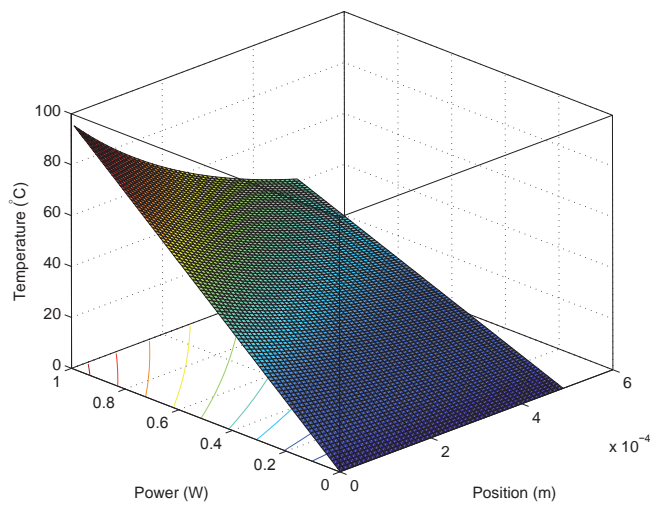


Figure 10. Temperature in blood layer as a function of incident power and thickness of the blood layer.

These models slightly underestimate the allowed power as some heat will diffuse away from the irradiated volume. Using the FEM model described in section 3.4.3 and using a 1 W source and a $500 \mu\text{m}$ layer between the probe and detector and 0.1 s irradiation gave a maximum temperature increase of 43°C indicating that the effect of heat being diffused away from the irradiated area is not important for these values.

5. DISCUSSION

5.1. Effect of blood layer on fluorescence measurements

Fluorescence spectra can without the presence of blood differentiate between various types of plaques based on the level of fluorescence. However, it was found that at thin blood layer will form between the probe and the vessel wall that is about 10-20 microns thick. In addition the vessel wall is not completely flat, especially in the presence of plaques so that even larger films of blood must be expected. If the film can vary up to 150 microns the signal variation due to the blood layer will be much larger than the expected variation in the fluorescence spectra. Washing the artery with saline could be possible but is stressful for the organs and might be clinically undesirable. Especially when large parts of the coronary tree is to be mapped constant flushing might be too stressful for this to be used as a screening method.

Some works have proposed variations in fluorescence lifetimes as a detection modality for plaque to avoid the interference of the blood but here signal and heating issues could be important.^{9,11,12} As shown, about 1 W is the limit on the power that can be used to irradiate to vessel wall to avoid serious damage to the blood. A security margin should probably be incorporated into this number. The temperature issue is dependent on the excitation wavelength used but 470 nm is close to the minimum in blood absorption in the wavelength region where autofluorescence can be excited. If the temperature issue turns out to be a problem, perhaps some cooling method of the blood layer could be incorporated.

6. CONCLUSION

To conclude fluorescence measurements of aorta are not feasible unless an effective flushing method that is clinically safe can be incorporated in the method. If this is possible fluorescence spectra can differentiate atherosclerotic plaques and calcified plaques from other pathological or normal states of the vessel wall. Without flushing heating of the blood is an issue when increasing the power of the excitation signal to achieve enough power on the detector due to the strong scattering and absorption of blood.

7. ACKNOWLEDGMENTS

The experiments in this report were approved by the Norwegian Board of Ethics in Medicine and was funded by the Norwegian Research Council. The help of the Norwegian Blood Bank for supplying materials is greatly appreciated. The authors greatly appreciate the aid of Eivind La Puebla Larsen, Andreas Meyer Winnem, Lise Lyngsnes Randeberg and Kari Kilen in preparing the document.

REFERENCES

1. D. H. Blankenhorn and H. Braunstein, "Carotenoids in man. iii. the microscopic pattern of fluorescence in atheromas and its relation to their growth", *J. Clin. Invest.* **37**, pp. 160–165, 1958.
2. C. Kittrell, R. Willett, C. de los Santos-Pacheo, N. Ratliff, J. Kramer, E. Malk, and M. Feld, "Diagnosis of fibrous arterial atherosclerosis using fluorescence", *Applied Optics* **24**, pp. 2280–2281, 2005.
3. R. Richards-Kortum, R. P. Rava, M. Fitzmaurice, J. R. Kramer, and M. S. Feld, "476 nm excited laser-induced fluorescence spectroscopy of human coronary arteries: Applications in cardiology", *American Heart Journal* **122**, pp. 1141–1150, 1991.
4. R. Richards-Kortum, R. P. Rava, M. Fitzmaurice, L. L. Tong, N. Ratliff, J. R. Kramer, and M. S. Feld, "A one layer model of laser-induced fluorescence for diagnosis of disease in human tissue: Applications to atherosclerosis", *IEEE Transactions on biomedical engineering* **36**, pp. 1222–1232, 1989.
5. K. Arakawa, K. Isoda, I. Toshimitu, K. Nakajima, T. Shibuya, and F. Ohsuzu, "Fluorescence analysis of biochemical constituents identifies atherosclerotic plaque with a thin fibrous cap", *Arterioscler. Thromb. Vasc. Biol.* **1**, pp. 1–71, 2002.
6. L. Marcu, Q. Fang, J. A. Jo, T. Papaioannou, A. Dorafshar, T. Reil, J.-H. Qiao, J. Baker, J. Freischlag, and M. Fishbein, "Fluorescence analysis of biochemical constituents identifies atherosclerotic plaque with a thin fibrous cap", *Arterioscler. Thromb. Vasc. Biol.* **181**, pp. 1–71, 2005.

7. G. Fillipidis, G. Zacharakis, A. Katsamouris, A. Giannoukas, and T. Papazoglou, "Single and double wavelength excitation of laser-induced fluorescence of normal and atherosclerotic peripheral vascular tissue", *J. Photochem. and Photobiol. B* **56**, pp. 163–171, 2000.
8. T. G. Papazoglou, "Malignancies and atherosclerotic plaque diagnosis - is laser induced fluorescence spectroscopy the ultimate solution?", *J. Photochem. and Photobiol. B* **28**, pp. 3–11, 1995.
9. Q. Fang, J. Jo, T. Papaioannou, A. Dorafshar, T. Reil, J.-H. Qiao, C. M. Fishbein, J. Freischlag, and L. Marcu, "Validation of a time-resolved fluorescence spectroscopy apparatus using a rabbit atherosclerosis model", *Proc. of SPIE* **5312**, pp. 294–299, 2005.
10. W.-C. Lin, S. A. Toms, E. D. Jansen, and A. Mahadevan-Jansen, "Intraoperative application of optical spectroscopy in the presence of blood", *IEEE journal on selected topics in quantum electronics* **7**, pp. 996–1003, 2001.
11. S. Andersson-Engels, J. Johansson, and S. Svanberg, "The use of time-resolved fluorescence for diagnosis of atherosclerotic plaque and malignant tumours", *Spectrochimica Acta A* **46**, pp. 1203–1210, 1990.
12. S. Andersson-Engels, J. Johansson, U. Stenram, K. Svanberg, and S. Svanberg, "Time-resolved laser induced fluorescence spectroscopy for enhanced demarcation of human atherosclerotic plaques", *J. Photochem. and Photobiol. B* **4**, pp. 363–369, 1990.
13. M. B. Lilledahl, M. Barkost, M. Gran, O. A. Haugen, and L. O. Svaasand, "Reflection spectroscopy of atherosclerotic plaque", *Journal of Biomedical Optics*, To be published march 2006 .
14. V. Tuchin, *Tissue Optics: Light scattering methods and Instrumentation for medical diagnostics*, SPIE Press, 2000.
15. H. S. Carslaw and J. Jaeger, *Conduction of heat in Solids*, Oxford Science Publications, 1959.
16. H. C. Stary, A. B. Chandler, R. E. Dinsmore, V. Fuster, S. Glagov, I. William, M. E. Rosenfeld, C. J. Schwartz, W. D. Wagner, and R. W. Wissler, "A definition of advanced types of atherosclerotic lesions and a histological classification of atherosclerosis", *Circ.* **92**, pp. 1355–1374, 1995.

Paper III

Reflection spectroscopy of atherosclerotic plaque

Magnus B. Lilledahl, Olav A. Haugen, Marianne Barkost
and Lars O. Svaasand. *Journal of biomedical optics*
11(2), 0210051-0210057 (2006)

Reflection spectroscopy of atherosclerotic plaque

Magnus B. Lilledahl

Norwegian University of Science and Technology
Department of Electronics and Telecommunications
O.S. Bragstads plass 2A
Trondheim 7491, Norway
E-mail: magnus.b.lilledahl@iet.ntnu.no

Olav A. Haugen

Saint Olavs Hospital
Department of Pathology and Medical Genetics
Olav Kyrres Gate 17
Trondheim 7006, Norway
and
Norwegian University of Science and Technology
Department of Laboratory Medicine, Children's
and Women's Health
Trondheim 7006, Norway

Marianne Barkost

Lars O. Svaasand

Norwegian University of Science and Technology
Department of Electronics and Telecommunications
Trondheim 7006, Norway

Abstract. Heart disease is the primary cause of death in the western world. Many of these deaths are caused by the rupture of vulnerable plaque. Vulnerable plaques are characterized by a large lipid core covered by a thin fibrous cap. One method for detecting these plaques is reflection spectroscopy. Several studies have investigated this method using statistical methods. A more analytic and quantitative study might yield more insight into the sensitivity of this detection modality. This is the approach taken in this work. Reflectance spectra in the spectral region from 400 to 1700 nm are collected from 77 measurement points from 23 human aortas. A measure of lipid content in a plaque based on reflection spectra is presented. The measure of lipid content is compared with the thickness of the lipid core, determined from histology. Defining vulnerable plaque as having a lipid core $>500 \mu\text{m}$ and fibrous cap $<500 \mu\text{m}$, vulnerable plaques are detected with a sensitivity of 88% and a specificity of 94%. Although the method can detect lipid content, it is not very sensitive to the thickness of the fibrous cap. Another detection modality is necessary to detect this feature. © 2006 Society of Photo-Optical Instrumentation Engineers. [DOI: 10.1117/1.2186332]

Keywords: atherosclerosis; fiber probe; near-infrared reflection spectroscopy; reflection spectroscopy; vulnerable plaque.

Paper 05163SSR received Jun. 30, 2005; revised manuscript received Jan. 19, 2006; accepted for publication Jan. 19, 2006; published online Apr. 20, 2006.

1 Introduction

Atherosclerotic plaques can be dangerous in two ways. First, the degree of stenosis can be severe enough to obstruct blood flow, thereby causing hypoxia in the tissue distal to the obstruction. Second, a plaque can rupture, exposing the blood stream to thrombogenic material that can induce the formation of a thrombus and sudden occlusion of the vessel. The latter is more dangerous because it is usually nonsymptomatic before rupture, and currently there exists no detection modality in clinical use that can detect these plaques. Plaques that are prone to rupture are denoted as vulnerable plaques. They are characterized by a large lipid core covered by a thin fibrous cap. Felton et al. reported the average lipid composition of the plaque as 25% free cholesterol, 52% cholesterol esters, 14% phospholipids, and 9% triglycerides.¹ Blankenhorn et al. have shown that the concentration of carotenoids (mainly beta-carotene) is larger in lipid-rich plaque than in a normal aorta.² Vulnerable plaques also have a thin fibrous cap, leaving them mechanically unstable. Virmani et al. give a value for the lipid core as less than $65 \mu\text{m}$ for a plaque to be denoted vulnerable.³ Prediman reports a cap thickness of less than 40% of total plaque size as a marker for vulnerability.⁴ This work investigates the use of reflection spectroscopy for detecting the lipid core, and whether it is possible to quantify the thickness of the lipid core and fibrous cap.

Many other methods have been proposed for the detection of vulnerable plaques, e.g., fluorescence spectroscopy, Raman

spectroscopy, elastography, thermography, and intravascular ultrasound (IVUS). Methods that are in clinical use today for detecting plaque (angiography, IVUS) cannot differentiate between vulnerable and stable plaques.

Existing studies on the applicability of reflection spectroscopy for detecting plaque can roughly be separated in two groups. It has been shown that near-infrared reflection spectroscopy (NIRS) correlates with measurements of the chemical composition of the plaque.⁵ It has also been shown that NIRS can differentiate between vulnerable and stable plaques, as determined from histology with good sensitivity and specificity.⁶⁻⁸ This has been shown using statistical methods like principle component analysis (PCA)^{6,7} and cluster analysis.⁸

In this work, a more analytic approach is taken. The region where a change in the reflection spectrum is expected is determined from the absorption spectra of the known constituents of plaque. It is determined if the change in spectral features can quantitatively be correlated with lipid content in the plaques. The major chromophores in the near-infrared (NIR) region are water, lipid, and cholesterol. The absorption spectra of these substances are shown in Fig. 1.⁹ Fat has three absorption peaks in the NIR region at approximately 930, 1200, and 1390 nm. The first two bands corresponds to the third and second overtone of the C-H stretching vibration. The third band is a combination of stretching and deformation vibrations of the C-H bond.¹⁰ Wang et al. reported absorption peaks at 1210, 1720, and 2304 nm.⁸

Address all correspondence to Magnus Lilledahl, Department of Electronics and Telecommunication, NTNU, O.S. bragstads plass 2A, Trondheim 7491, Norway. Tel: +47 73591471. Fax: +47 73591441. E-mail: b.lilledahl@iet.ntnu.no

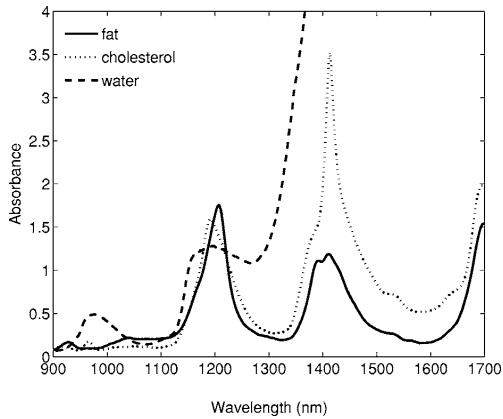


Fig. 1 Absorption spectra of the most important absorbers in the NIR spectral region.⁹

In the visible region, the most significant change in the spectrum for lipid-rich plaques is probably due to a higher concentration of carotenoids (mainly beta-carotene).² Figure 2 shows the absorption spectrum of beta-carotene.¹¹ Based on the knowledge of this spectrum, regions where there is a change in the reflectance spectrum due to lipid content in the plaque has been identified. A simple measure of lipid content in the plaque based on this information is proposed.

2 Materials and Methods

2.1 Materials

A section of the thoracic aorta from 23 patients (14 men and 9 women) were excised during autopsy. No special rules were employed in selecting the patients that were included in the study. Age of patients at death were 56 ± 21 years. In the time between autopsy and measurements (~ 2 h), the sample was kept in phosphate buffered saline (PBS) at room temperature. The section of the aorta was opened longitudinally and placed

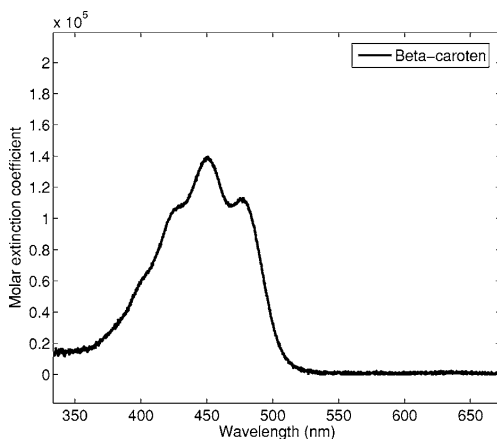


Fig. 2 Molar extinction coefficient of beta-carotene.¹¹

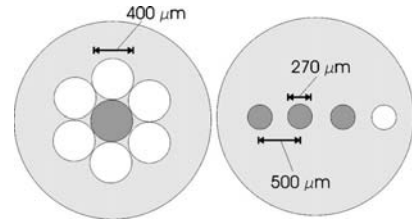


Fig. 3 A schematic view of the tip of the two fiber probes used in the experiment. The white circles represent excitation fibers and the gray represent collection fibers.

on a piece of black cardboard with the lumen side facing up. For two of the samples, measurements were also collected with white copy paper as the bottom layer, but no systematic difference in the reflectance was detected. Between one and seven measurement points were selected from each sample, depending on the prevalence of atherosclerotic plaque. The selection was performed by visual inspection. One measurement point was chosen from a region that looked normal and the remaining points from areas that looked like plaque. The entire measurement series took about 2 h for each sample. During measurements, the samples were kept hydrated by dripping PBS on the samples with a pipette. Just before placing a probe on the sample, the surface was lightly dried with paper tissue.

2.2 Methods: Reflection Measurements

Reflection spectra in the wavelength range 400 to 1700 nm were acquired for each measurement point using two different spectrometers (Ocean Optics SD2000, double channel; and Ocean Optics NIR512, Ocean Optics, Duiven, The Netherlands). The SD2000 spectrometer is sensitive in the region from 400 to 1100 nm, and the NIR512 spectrometer from 900 to 1700 nm. Three different probes were used in the measurements: 1. an integrating sphere (Ocean Optics, ISP-REF), 2. a fiber reflection probe (Ocean Optics, VIS-NIR) with seven excitation fibers placed in a circular fashion around a central collection fiber (hereby denoted "circular probe"), and 3. a fiber reflection probe (Ocean Optics, custom design) with four fibers placed in a linear array (hereby denoted "linear probe"). For the linear probe, the fiber furthest to the side was used as the excitation fiber, and the three other fibers could act independently as collection fibers. For a schematic drawing and dimensions of the fiber probes, see Fig. 3. All the probes were connected to the spectrometers via fiber connections.

The integrating sphere was hand-held during measurements while the fiber probes were positioned using a micrometer positioning stand and kept just in contact with the tissue during measurements. The contact point was determined by visual inspection. The sample was not fixed to the stand, so the placement of different probes at the same point was done visually. The error of the lateral position was estimated to be less than 2 mm.

Spectra were recorded as percent reflection relative to a reflection standard (SRS-99-010, LabSphere, North Sutton, United Kingdom). The integrating sphere was placed in direct contact with the standard for the reference measurements. For

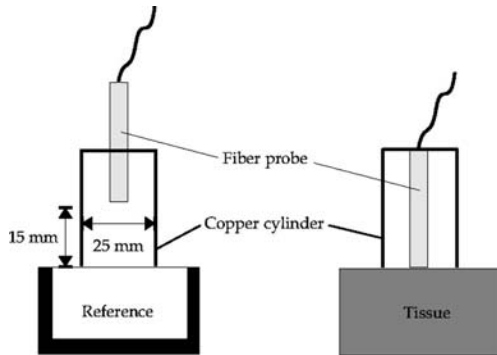


Fig. 4 A schematic view of the reference measurement used for the fiber probes. For the reference measurement (left), the fiber probes were positioned 1.5 cm away from the standard but were in contact with the tissue during reflection measurements (right).

the circular and linear probes, the tip of the probe was positioned 15 mm from the surface of the reflectance standard. The reflectance standard has a very high scattering coefficient, so the penetration depth is very small. If the fiber probes are put on the surface, very few photons will reach a fiber that is separated from the excitation fiber by more than one penetration depth. This effect might be wavelength dependent, and this is the reason that the fibers were positioned away from the surface of the reflectance standard. The reflectance values for the probes are thus not relative to 100% reflectance, but relative to a spectrally flat standard of unknown absolute reflectance. A black-painted copper cylinder was placed around the probe to shield from ambient lighting. The same black cylinders were used during measurements to shield from the ambient lighting, but the probes were then in contact with the tissue. The procedure is illustrated in Fig. 4.

2.3 Methods: Histology

The samples were prepared for histology immediately after the spectroscopic measurements. A rectangle ($\sim 10 \times 4$ mm) was cut out around the measurement point with a scalpel and divided along the long center line. One part was fixed in 10% buffered formalin and embedded in paraffin, while the other was frozen in liquid nitrogen. The samples were then sliced and stained. The formalin sample was stained with hematoxylin-eosin-saffron (HES) and the frozen sections with Sudan(3). The sections were then photographed through a microscope at three different magnifications (2, 10, and $20\times$). To be able to quantify the size of histological sections, a microscopic measurement stick was also photographed at the various magnifications. The size of the histological features (total plaque, lipid core, and cap thickness) was measured by manually comparing prints of the sample and the measurement stick, at the same magnification, using a ruler.

3 Analysis

3.1 Spectral Analysis

The first derivative of the NIR spectra was computed using the method of Savitzky and Golay using the software package

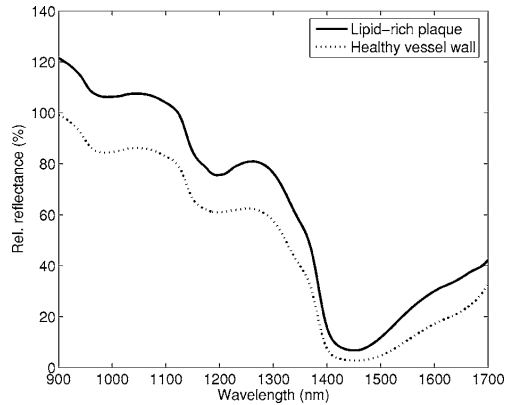


Fig. 5 Example reflectance spectra from the NIR region. For the lipid-rich plaque (solid line), there is an additional local minimum around 1200 nm that is superimposed on the broader minimum due to water absorption.

Matlab (Mathworks, Natick, MA).¹² The lipid peak around 1200 nm causes a local minimum in the spectrum that is superpositioned on the reflectance minimum due to the water absorption (see Fig. 5). The derivatives of these spectra are shown in Fig. 6. For the normal vessel, the derivative increases monotonically (i.e., a decrease in the negative slope of the reflectance spectra), while for the lipid-rich plaque, the derivative starts to decrease around 1168 nm due to the superpositioning of the lipid absorption band over the water absorption band. The difference between the peak and the valley of this spectrum is assigned as the lipid index denoted C_l . This is illustrated in Fig. 6.

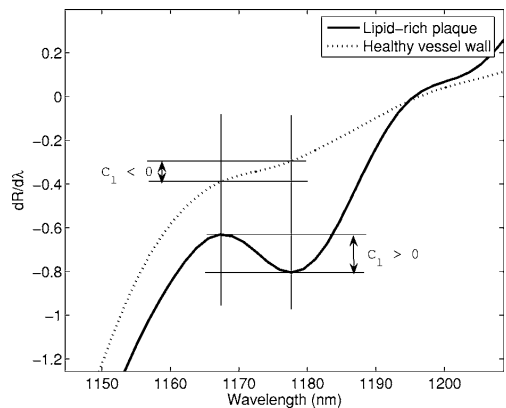


Fig. 6 Illustration of the lipid index $C_l = dR/d\lambda|_{\lambda=1168} - dR/d\lambda|_{\lambda=1178}$. The figure shows the derivative of the spectra in Fig. 5. For the normal artery (dashed line), the derivative increases monotonically, whereas for the lipid-rich, there is a local minima due to the superimposed lipid absorption. $C_l > 0$ when a certain amount of lipid is present in the sampling region of the probe.

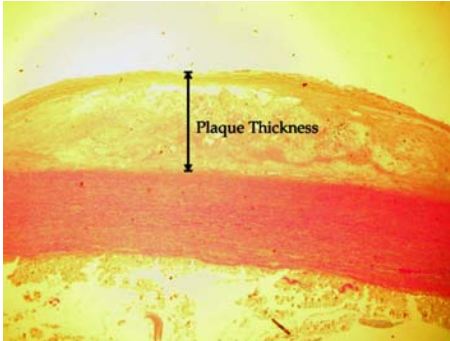


Fig. 7 Definition of plaque thickness.

$$C_l = \frac{dR}{d\lambda} \Big|_{\lambda=1168} - \frac{dR}{d\lambda} \Big|_{\lambda=1178} \quad (1)$$

In the visible region, the lipid-index C'_l was taken as the difference between the reflection at 560 nm (where there is little beta-carotene absorption but substantial blood absorption) and the reflection at 450 nm (the absorption peak of beta-carotene), divided by the reflection at 700 nm. At 700 nm, the absorption of both beta-carotene and blood is relatively small. Dividing by this value accounts for the overall reflectance level of the spectrum due to scattering properties.

$$C'_l = \frac{R(560) - R(450)}{R(700)} \quad (2)$$

3.2 Histological Analysis

A picture was taken of a microscopic measuring stick for each magnification so that absolute lengths could be determined in the histological photographs. From these photographs, the thickness of the total plaque, the fibrous cap, and the lipid core were determined. The total plaque thickness was determined from the HES stained sections as the distance from the media (defined as the presence of red colored elastin fibers) to the endothelium (Fig. 7). The core thickness was determined from the Sudan Red stained sections as the thickness of the area where red stained lipid droplets were present. The fibrous cap thickness was defined as the distance from the inner lining of the vessel to the start of the lipid core (Fig. 8).

4 Results

Figures 9 and 10 contain typical reflectance data from an artery for the NIR and visible spectral region. The corresponding aorta sample is shown in Fig. 11. The only change in the NIR reflectance spectra where there is known lipid absorption was at a point around 1200 nm. In the visible region, there seemed to be an increased absorption from 450 to 500 nm for lipid-rich plaques.

The spectral analysis, defined in Sec. 3.1 was then compared with the histological studies. In Figs. 12–15, plots of C_l and C'_l are plotted against the lipid core thickness. In these plots, plaques with a lipid core greater than 500 μm or a

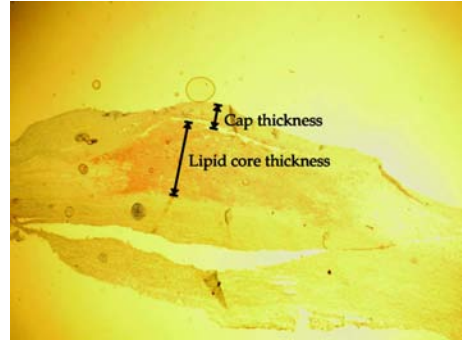


Fig. 8 Definition of lipid core thickness and fibrous cap thickness.

fibrous cap less than 500 μm are defined as vulnerable. For measurements in the NIR, a line has been drawn at $C_l=0$ as a possible demarcation between a lipid-index, indicating a stable or vulnerable plaque. For the visible region (Fig. 15), the demarcation line was arbitrarily put at 0.25, which seemed to yield the best results. Only data for the circular probe are presented for the visual region. Using these definitions, the sensitivities and specificities for the various measurements were calculated. The results are tabulated in Table 1.

5 Discussion

Water is an important absorber in the NIR region. Even though the samples were put in PBS, which has the same osmotic pressure as tissue, there might be some absorption of water into the tissue, which can cause swelling. This might change the optical properties of the tissue. However, the endothelium of the aorta is constantly exposed to the liquid environment of the blood stream, so it seems likely that the sample should be somewhat resistant to this effect. On the other hand, since the combined measurements took up to 2 h, there might be some dehydration during the experiment, even if PBS was often dripped onto the sample. This swelling or dehydration effect (whichever is stronger) might affect the reflectance spectra on which the calculation of C_l is based.

The thickness of the vessel wall was different as determined from the formalin fixed sections compared to the frozen sections. Size artifacts are known problems in histology.¹³ The measurement of the lipid core thickness might therefore have an inherent systematic error. The precision of the size measurements was estimated to be about 50 μm . This was calculated as the average size difference of the same structure, measured in the frozen and in the formalin fixed sections. This gives no estimate on how well the measurements compare to the original size of the plaque, as there might be other systematic errors linked to the fixation process.

From Fig. 10, it seems like the difference in the spectra between a normal vessel and a lipid containing plaque is stronger in the visible region than in the near-infrared region. However, Fig. 15 shows that the correlation with lipid content is poorer. This is most likely due to the large blood absorption that overlaps the absorption spectra of beta-carotene. Small differences in the vasculature of the vessel can have large implications on the measured spectra. This can be seen in Fig.

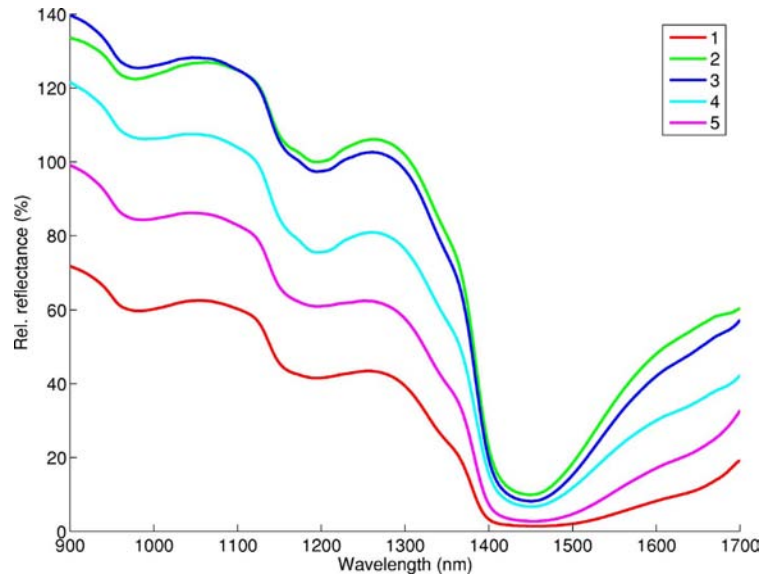


Fig. 9 Reflectance spectra in the NIR region corresponding to the measurement points in Fig. 11.

16, where two reflection spectra of normal aorta from a 24 and a 78 year old male are shown. In general, the older the person was from which the aorta was taken, the redder the vessel appeared. This variation had a stronger effect on the spectra the deeper the penetration depth of the probe was. No trends could therefore be seen for the integrating sphere and the linear probe, and they have hence not been included. Also, the large blood absorption for wavelengths below 700 nm makes it difficult to perform measurements through even a thin film of blood, making it uncertain if a measurement is feasible. Some form of flushing of the artery is most likely needed. Since carotenoids are preferentially absorbed in lipid-rich plaque, it might be possible to attach some fluorescent

molecule or stronger chromophore to a carotenoid or other lipophilic molecule to increase the contrast between stable and vulnerable plaque. The preferential uptake of endogenous beta-carotene in plaque has been demonstrated by Prince, Glenn, and MacNichol.¹⁴

The absorbance values in Fig. 1 are measured in pure form. The absorbance peaks will change slightly due to the chemical environment, so these spectra cannot be taken exactly as the absorbance values that are expected from the tissue. Neither are the many types of lipids in the plaque the same as those used in the absorption measurements.¹ The absorbance spectra should only be regarded as indications of where variations in the reflectance spectra can be expected.

A histological section of a vulnerable plaque can be seen in Fig. 7. It is apparent that the thickness of the fibrous cap

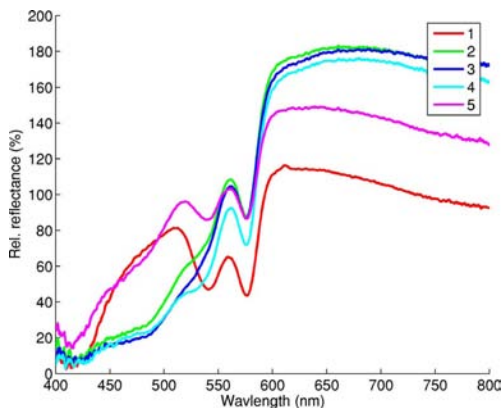


Fig. 10 Reflectance spectra in the visible spectral region corresponding to the measurement points in Fig. 11.

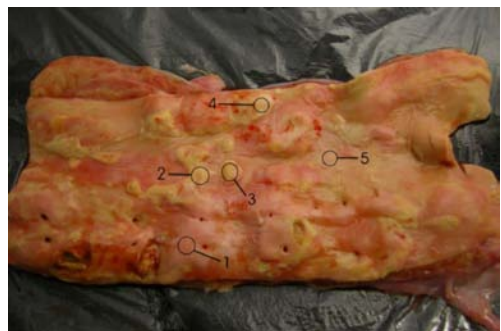


Fig. 11 Aorta sample. The circles show measurement points and the numbers correspond to the reflectance spectra in Figs. 10 and 9. The sample is approximately 15 cm long.

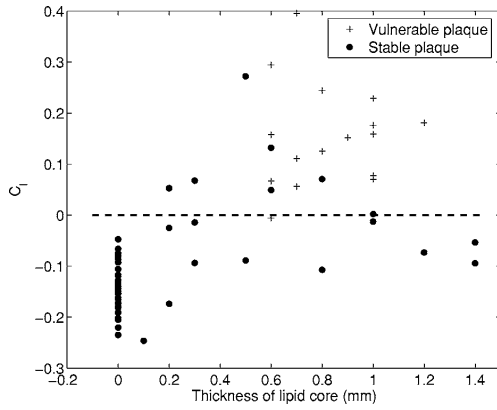


Fig. 12 Lipid index C_l versus thickness of lipid core, measured with the circular fiber probe.

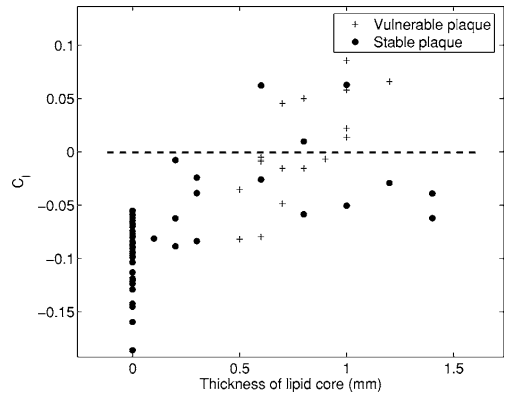


Fig. 14 Lipid index C_l versus thickness of lipid core, measured with the integrating sphere.

varies over the extent of the plaque. Any clinical implementation of this method will need to have a lateral resolution less than 1 mm, or vulnerable plaques might be incorrectly characterized as stable even though they have a very thin cap on the edge, where the mechanical forces are strongest.

The spectroscopic measurements are to a certain degree sensitive to the thickness of the cap, as can be seen in Figs. 12 through 15. Even though a plaque has a large lipid core, it gives a low value of C_l , since it is covered by a thick fibrous cap. However, in the literature a plaque with cap thickness less than $65 \mu\text{m}$ is defined as a vulnerable plaque, and this is not detectable with the current instrumentation.³ The definition used in this work is partially based on the discrimination that could be expected, given the geometry of the probes that were used, and partially warranted by the definition given in one of the references.⁴ If the minimum cap thickness of $65 \mu\text{m}$ had been used, many points in the upper right quadrant of Figs. 12 through 15 would be considered stable instead

of vulnerable. If plaques with lipid cores less than $500 \mu\text{m}$ had been considered vulnerable if the cap was thin enough, many points in the lower left quadrant of Figs. 12 through 15 would be vulnerable instead of stable. The definition used was chosen to show that the method detects the presence of lipid and is also partially sensitive to the thickness, but that probably an additional method with high resolution is needed to measure the cap, e.g., optical coherence tomography, confocal microscopy, or multiphoton microscopy. An array of very small fibers ($\sim 10 \mu\text{m}$) with very small fiber separation could also achieve this. There are also lipid absorption peaks higher up in the infrared spectrum where the penetration depth is small due to the high water absorption. Using several wavelengths with different penetration depths, it could be possible to calculate approximately at what depth the lipid core is. A tomographic method that can also detect the lumen surface is probably best, since the precise positioning of a probe inside a coronary artery is difficult. A sensor using reflection spectroscopy could be used to scan the artery. If the presence of lipid

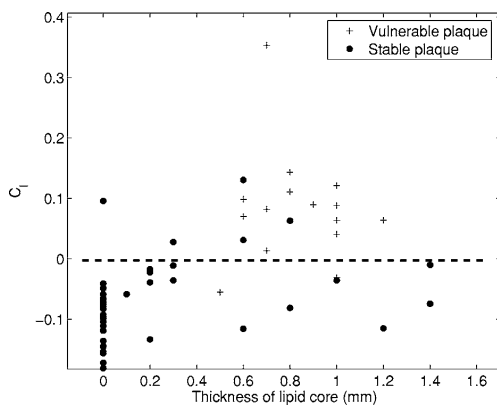


Fig. 13 Lipid index C_l versus thickness of lipid core, measured with the linear fiber probe, using the fiber nearest to the excitation fiber as the collection fiber. Using the other fibers as collection fibers gave poorer correlation with the thickness of the lipid core.

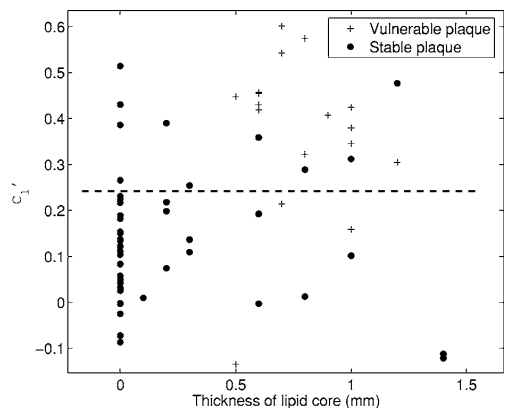


Fig. 15 Lipid index C_l for the visible region versus thickness of the lipid core, measured with the circular fiber probe.

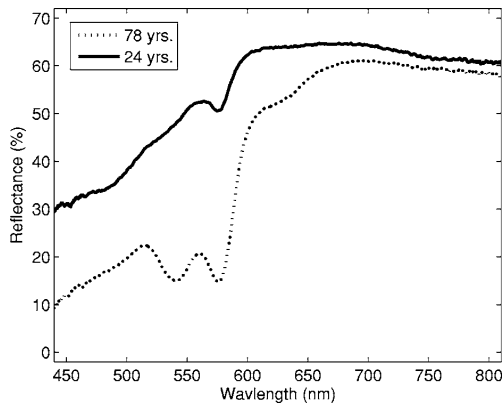


Fig. 16 Variation in reflection spectra in the visible region from normal aorta. In general, the absorption of hemoglobin was stronger the older the person was, and the redder the vessel appeared.

is detected, a high resolution method could be used to make an accurate measurement of the cap thickness.

The aorta is about a factor of 5 larger than the coronary arteries. It must be determined if the method is still sensitive when all sizes are scaled down. Light will penetrate deeper into vessel structures, so a method that only collects light scattered from the plaque will be important.

6 Conclusion

It is shown that NIRS can detect the presence of lipid in plaque in the aorta with good sensitivity. It cannot, however, determine accurately the thickness of the cap. Some other high resolution tomographic method would probably have to be used to determine this. Reflection spectra in the visible region seem to be able to provide some information about lipid content, but yield poorer correlation than the NIR spectral region. Lateral resolution of at least 1 mm is necessary, as the cap thickness can vary throughout the plaque area.

7 Future Studies

It remains to be determined if this detection modality is still possible through a varying layer of blood, or if it is necessary

Table 1 Sensitivities and specificities of the various measurements.

	Circular probe (NIR)	Linear probe (NIR)	Integrating sphere (NIR)	Circular probe (VIS)
Sensitivity	88%	88%	44%	83%
Specificity	94%	81%	91%	79%

in some way to press the sensor against the vessel wall. The additional imaging modality that needs to be added must also be determined from viewpoints of resolution, contrast, size, and complexity. It must be determined if the methods are also sensitive in the smaller coronary arteries.

Acknowledgments

We would like to thank Unn Granli for the preparation of the histological sections, and all the people that have given constructive feedback on this article: Lise Lyngsnes Randeberg, Eivind La Puebla Larsen, and Dag Roar Hjelme. This work was part of a project funded by the Norwegian Research Council.

References

1. C. Felton, D. Crook, M. Davies, and M. Oliver, "Relation of plaque lipid composition and morphology to the stability of human aortic plaques," *Arterioscler., Thromb., Vasc. Biol.* **17**, 1337–1345 (1997).
2. D. H. Blankenhorn, D. G. Freiman, and H. C. Knowles, "Carotenoids in man: the distribution of epiphasic carotenoids in atherosclerotic lesions," *J. Clin. Invest.* **35**, 1243–1247 (1956).
3. R. Virmani, F. D. Kolodgie, A. P. Burke, A. Farb, and S. M. Schwartz, "Lessons from sudden coronary death: a comprehensive morphological classification scheme for atherosclerotic lesions," *Arterioscler., Thromb., Vasc. Biol.* **17**, 1337–1345 (1997).
4. K. S. Prediman, "Mechanisms of plaque vulnerability and rupture," *J. Am. Coll. Cardiol.* **41**, 15S–22S (2003).
5. W. Jaross, V. Neumeister, P. Lattke, and D. Schuh, "Determination of cholesterol in atherosclerotic plaques using near infrared diffuse reflection spectroscopy," *Atherosclerosis* **47**, 327–337 (1999).
6. P. R. Moreno, R. A. Lodder, R. Purushotaman, W. E. Charash, W. N. O'Connor, and J. E. Muller, "Detection of lipid pool, thin fibrous cap and inflammatory cells in human aortic atherosclerotic plaques by near-infrared spectroscopy," *Circulation* **105**, 923–927 (2002).
7. A. M. K. Nilsson, D. Heinrich, J. Olajos, and S. Andersson-Engels, "Near infrared diffuse reflection and laser-induced fluorescence spectroscopy for myocardial tissue characterisation," *Spectrochim. Acta, Part A* **53**, 1901–1912 (1997).
8. J. Wang, Y. Geng, B. Guo, T. Klima, B. N. Lai, J. T. Willerson, and W. Casscells, "Near-infrared spectroscopic characterization of human advanced atherosclerotic plaque," *Atherosclerosis* **39**, 1305–1313 (2002).
9. M. B. Lilledahl, O. A. Haugen, L. L. Randeberg, and L. O. Svaasand, "Characterization of atherosclerotic plaque by reflection spectroscopy and thermography: A comparison," *Proc. SPIE* **5686**, 415–425 (2005).
10. B. Osborne and T. Fearn, *Near Infrared Spectroscopy in Food Analysis*, Longman Scientific and Technical (1988).
11. H. Du, R. A. Fuh, J. Li, A. Corkan, and J. S. Lindsey, "Photochemcad: A computer-aided design and research tool in photochemistry," *Photochem. Photobiol.* **68**, 141–142 (1998).
12. A. Savitzky and M. J. E. Golay, "Smoothing and differentiation of data by simplified least squares procedures," *Anal. Chem.* **36**, 1627–1639 (1964).
13. M. McCall, C. J. Harkrider, V. Deramo, S. F. Bailey, K. P. Winter, B. A. Rockwell, D. J. Stolarski, and C. A. Toth, "Using optical coherence tomography to elucidate the impact of fixation on retinal laser pathology," *Proc. SPIE* **4257**, 142–148 (2001).
14. M. R. Prince, M. L. Glenn, and E. F. MacNichol, Jr., "Increased preferential absorption in human atherosclerotic plaque with oral beta carotene," *Circulation* **78**, 338–344 (1988).

Paper IV

An analytic and numerical study of intravascular thermography of vulnerable plaque

Magnus B. Lilledahl, Eivind L. P. Larsen and Lars O. Svaasand. *Physics in medicine and biology*. *In press*.
To be published january 2007.

An analytic and numerical study of intravascular thermography of vulnerable plaque

M B Lilledahl, E L P Larsen and L O Svaasand

Norwegian University of Science and Technology, 7018 Trondheim, Norway

E-mail: lilledahl@iet.ntnu.no

Received 30 August 2006, in final form 12 December 2006

Published 24 January 2007

Online at stacks.iop.org/PMB/52/961

Abstract

Intravascular thermography has been proposed as a method for detecting vulnerable plaque. A marker of vulnerability in a plaque is inflammation, which is believed to reduce its mechanical stability. It has been hypothesized that this inflammation leads to a higher metabolic rate and therefore higher heat generation, causing increased temperature in the vicinity of the plaque. This temperature increase could be measured intravascularly using a temperature sensor, e.g., a thermistor or a thermocouple. The aim of this study is to present a thorough mathematical and physical analysis of the thermal distribution that can be expected in the plaque under various physiological conditions. To get reasonable predictions on the expected temperature distributions, idealized models with simple geometries are solved analytically. More realistic models, with more complex geometries, are solved numerically using the finite element method (FEM). Based on this analysis, the maximum temperature increase that can be expected in a plaque due to increased metabolism is less than 0.1 K.

(Some figures in this article are in colour only in the electronic version)

1. Introduction

Cardiovascular disease is the most prevalent cause of death in the US and most of these deaths are due to myocardial infarction (Thom *et al* 2006). These are usually caused by an occlusive thrombosis in the coronary arteries, induced by the rupture or erosion of so-called vulnerable atherosclerotic plaques (Davies and Thomas 1985).

Vulnerable plaques have several characteristic properties that are relevant for their detection: a large lipid core covered by a thin fibrous cap and inflammation marked by the presence of macrophages (Felton *et al* 1997). Inflammation decreases plaque stability by the release of metalloproteinases which degrade the fibrous cap. It is hypothesized that this inflammation increases the temperature at the plaque surface (Casscells *et al* 1996). Detecting

inflamed plaques could yield important clinical information about which plaques are likely to develop quickly and cause a coronary thrombosis.

The use of temperature measurements for detecting plaques was first proposed by Casscells *et al* (1996). They investigated the temperature variation on the surface of carotid plaques, excised during endarterectomy. The surface temperature was measured with a thermistor. They measured temperature differences up to 2.2 K on the surface. In one instance, temperature differences of 0.6 K were measured at two sites only 1 mm apart. It was shown that temperature difference correlated positively with cell density in the plaque and negatively with the cap thickness. These measurements were conducted at room temperature. Larger temperature differences (0–5 K) were reported on measurements performed in an incubator at 37 °C, but no further details were provided. Temperature was also measured with an infrared camera, but no results were presented.

Several *in vivo* measurements have shown temperature heterogeneity in coronary arteries. For a review of experimental results of thermography, see Madjid *et al* (2006). Some of these have correlated temperature heterogeneity with the type of coronary disease (Stefanadis *et al* 1999) and shown that it serves as a predictor for clinical outcome (Stefanadis 2001, Schmermund *et al* 2003). Temperature heterogeneity has also been correlated with biomarkers, e.g., C-reactive protein (Stefanadis *et al* 2000). A recent study by Rzeszutko *et al* (2006) found that the maximal temperature difference between blood and vessel wall was found in the culprit segment in 57.5% of the patients examined.

Two FEM studies on temperature distribution due to an atherosclerotic plaque have been published (ten Have *et al* 2004, 2005). In the first study they investigated the effect of plaque geometry and of blood flow on the measured temperature. The heat generation they used in the plaques ranged from $0.1 \times 10^9 \text{ W m}^{-3}$ to $0.4 \times 10^9 \text{ W m}^{-3}$. These values were determined by requiring that the resulting temperatures fit published experimental values. Perfusion of the surrounding tissue was not included in their modelling of the temperature distribution. The second study investigated how the probe geometry and sensor material affect the temperature measurements.

There is a large discrepancy amongst the measured values published in the literature. The aim of this study is to present a thorough mathematical and physical analysis of the thermal distribution that can be expected in plaques under various conditions. This framework can then be used to analyse experimental results. Since the published values vary so much, estimates of metabolic rates are derived by indirect consideration instead of requiring a fit to experimental values. Analytical models were investigated for geometries that are simple enough to be solved analytically. This gives reasonable predictions on the temperature variations that can be expected and physical insight into how various parameters affect the measurements. Numerical calculations of more realistic models were computed with the finite element method (FEM)

2. Physics

2.1. Physical model

The temperature distribution in the vessel wall is calculated assuming that the heat generated in the tissue is transported by conduction, convection by the flowing blood in the lumen, and perfusion in the surrounding tissue. The perfusion is modelled by the so-called bioheat equation:

$$\kappa \nabla^2 T - \rho_t c_t \frac{\partial T}{\partial t} = -q + \rho_b c_b \omega (T - T_0). \quad (1)$$

This equation was first presented by Pennes (1948) and has been further analysed in many works, e.g., Chen and Holmes (1980). The assumption in this equation is that constant tissue temperature is maintained by the colder arterial blood removing heat from the tissue when passing through the capillary network. The heat generated in the body's core must be transported to the lungs and skin via the blood. If the heat transport was via conduction alone, very high temperatures would result in the centre of the body. For the blood to transport heat away from the tissue, the temperature in the arterial network must necessarily be lower than the venous network (this is not valid in the skin where the heat is dissipated and the blood is cooler on the venous side). The last term in (1) models the removal of the heat due to perfusion. ω is the volume of perfused blood per volume of tissue per unit time (see appendix A). T is the temperature of the tissue, and T_0 is the temperature of the arterial blood. q represents the heat per unit volume per unit time (Q will be used for the total heat generated in a volume per unit time). ρ_t and ρ_b are the densities of tissue and blood respectively, c_t and c_b are the specific heats of tissue and blood respectively. κ is the thermal conductivity of tissue.

The total heat distribution in a system is the result of all the heat sources in the system. We will assume that the temperature in the system can be divided into the temperature T_1 due to the heat generation from the plaque q , and T_2 due to the heat q_s generated by the rest of the system. We thus write equation (1) as

$$\kappa \nabla^2(T_1 + T_2) - \rho_t c_t \frac{\partial(T_1 + T_2)}{\partial t} = -(q_s + q) + \rho_b c_b \omega(T_1 + T_2 - T_0). \quad (2)$$

This equation can be divided into two separate equations:

$$\kappa \nabla^2 T_1 - \rho_t c_t \frac{\partial T_1}{\partial t} = -q + \rho_b c_b \omega(T_1) \quad (3)$$

and

$$\kappa \nabla^2 T_2 - \rho_t c_t \frac{\partial T_2}{\partial t} = -q_s + \rho_b c_b \omega(T_2 - T_0). \quad (4)$$

By adding these two equations, the solution for the total temperature distribution results. Only (3) will be solved since T_1 represents the deviation from normal temperature due to the heat generation in the plaque, and this is the desired quantity. From now on T_1 will be referred to as T . The thermal gradients from (4) due to normal metabolism q_s are relevant in the measurement process. This is discussed in section 6.3. For a steady state, (3) becomes

$$\nabla^2 T = -\frac{q - PT}{\kappa}. \quad (5)$$

Here $PT = c_b \rho_b \omega T$ is the amount of heat removed per unit volume and time due to perfusion of the tissue. (5) is the equation solved in the analytic models. Radiation has been proposed as a thermal transport mechanism but can have no significant effect in this system. This is discussed in appendix B.

In the numerical models the convection by the blood flowing in the lumen is included. For the blood it is assumed that the heat is transported by convection and conduction so that the equation to be solved is

$$\kappa_b \nabla^2 T - \rho_b c_b \frac{\partial T}{\partial t} = \rho_b c_b \vec{v}_b \cdot \nabla T, \quad (6)$$

where the last term represents the heat transport due to convection and \vec{v}_b is the velocity of the blood.

To determine the velocity profile of the blood stream, the steady-state Navier–Stokes equation for an incompressible fluid,

$$\rho_b (\vec{v} \cdot \nabla) \vec{v} = -\nabla p + \eta \nabla^2 \vec{v}, \quad (7)$$

Table 1. Thermal properties used in the models. Diffusivity $\chi = \frac{\kappa}{\rho c_p}$. For a definition of the perfusion parameters, see appendix A.

Material	Density ρ (kg m ⁻³) ^a	Specific heat c_p ($\times 10^3$ J kg ⁻¹ K ⁻¹) ^b	Thermal conductivity κ (W m ⁻¹ K ⁻¹) ^c	Diffusivity χ ($\times 10^{-7}$ m ² s ⁻¹)	Perfusion F (ml min ⁻¹ g ⁻¹) ^d	Perfusion factor P (W K ⁻¹ m ⁻³)
Blood	1055	3.66	0.505	1.30	–	–
Intima	1010	3.72	0.476	1.27	–	–
Plaque	1010	3.72	0.484	1.25	–	–
Media	1040	3.72	0.476	1.23	–	–
Muscle	–	–	0.460	–	0.02	3.3×10^3
Fat	920	2.3	0.210	0.99	0.001	0.16×10^3

^a Gandhi *et al* (1996).^b ten Have *et al* (2006).^c Dumas and Barozzi (1984), Valvano and Chitsabesan (1987) and Cohen (1977).^d Svaasand (1982).

was solved, where p is the pressure and η the dynamic viscosity. Blood is not a Newtonian fluid (which is required for the validity of the Navier–Stokes equation, even though there are ways to incorporate a non-Newtonian fluid), but we assume it is Newtonian for the velocities and diameters in question.

2.2. Thermal and fluidic properties

The average fluid velocity (averaged in both space and time) is about 0.3 m s⁻¹ in medium-sized arteries (Marsden 1998). The velocity is dependent on pressure gradients, so 120/80 blood pressure will result in a variation in the velocity of the blood between systole and diastole of about 30%. The numerical simulations were performed with a parabolic input velocity with 0.3 m s⁻¹ average velocity except for the simulations in section 5.2.4, where the blood flow was varied from 0 to 5 m s⁻¹.

The dynamic viscosity of blood ranges from 1.5×10^{-3} to 4×10^{-3} Pa s for hematocrits from 20 to 65% (not linearly) (Burton 2000). We used a value of 2.5×10^{-3} Pa s in all the simulations. This corresponds to a hematocrit of 45%, which is in the normal range for adults.

The thermal properties of various tissue types are summarized in table 1. No perfusion values were found for the media or adventitia, so values from skeletal muscle and fatty tissue were used as upper and lower limits. As the perfusion in the myocardium is higher than in skeletal muscle, the perfusion around the coronary arteries might be even higher (Svaasand 1982).

2.3. Heat generation

Several mechanisms for increased heat generation in plaques have been proposed (ten Have *et al* 2005). These are higher metabolism of inflammatory cells, presence of uncoupling proteins, lipid endocytosis and matrix metalloproteinase degrading the extracellular matrix. Another proposed source of increased heat generation is the uncoupling protein thermogenin (Diamantopoulos 2003, ten Have *et al* 2005), as this protein causes the energy that would be converted to mechanical energy to be released as thermal heat instead. However, no quantitative value of the metabolism in plaque exists for use in the models. Therefore, an order of magnitude estimate of the likely temperature increase was derived from the following considerations.

The basal metabolic rate for a 70 kg man ranges from 5000–9000 kJ/day (Burton 2000). This is equivalent to 58–104 W. Assuming that the density of a man is about 800 kg m^{-3} and 70% of the weight is living tissue gives a heat generation per volume of 663–1189 W m^{-3} . Under strong exercise there can be up to a 20-fold increase in the metabolism (Tortora and Grabowski 2003), giving a maximal heat generation of about $2 \times 10^4 \text{ W m}^{-3}$.

In a study of alveolar macrophages the metabolism of a single cell was found to be 20 pW/cell (Thoren *et al* 1990). Assuming a tissue dense with macrophages of average size $10^3 \mu\text{m}^3$ gives a heat generation of $2 \times 10^4 \text{ W m}^{-3}$ (Lilledahl *et al* 2005).

In the work of Casscells *et al* (1996), thin samples excised during endarterectomy were taken out and placed on a table in room temperature. Since the samples were thin (thickness not specified in paper) most of the heat will be lost to the air and the table and not so much along the tissue. The conductivity of air is $0.025 \text{ W K}^{-1} \text{ m}^{-1}$. Modelling the plaque as a sphere with radius $a = 2 \text{ mm}$ completely surrounded by air and assuming a temperature difference of 1 K at the surface, (9) yields a heat generation of $18\,750 \text{ W m}^{-3}$. Because few experimental details were disclosed in the paper, this simplistic model is uncertain. The calculation should be considered in the sense that the results of Casscells *could* be explained by the heat generation we have used, rather than as an argument for a likely *in-vivo* value.

Bjørnheden and Bondjers (1987) found that for early lesions the oxygen consumption increases, but decreases below normal levels for more developed lesions. The initial increase was of the order of 50–100%. Whether these plaques had macrophage infiltration was not specified. A reduction in metabolism in highly developed plaques will reduce the effect of the higher metabolism due the macrophage infiltration.

Heinle (1987) reported a decreasing content of glucose, glycerol and ATP, and increasing amounts of lactate with increasing distance into the vessel. This indicates an ineffective, anaerobic metabolism, which will counteract the increased heat generation due to the macrophages. This was in pre-necrotic core plaques, and it seems likely that the metabolism would fall even further when a non-metabolizing necrotic core is present. Whether more heat is generated under anaerobic conditions since more energy is converted into heat instead of adenosine triphosphate (ATP), or less heat is generated since the overall energy turnover is less, is unknown. Under aerobic conditions 60% of the metabolized energy is converted to heat (Tortora and Grabowski 2003), so the heat generation cannot increase by more than 40% under anaerobic conditions due to ineffective ATP production.

Based on these considerations we have used the metabolic rate of $2 \times 10^4 \text{ W m}^{-3}$ in our models (a 20-fold increase over normal metabolism). This value is comparable to the heat generated in a maximally working body or a tissue dense with macrophages. Based on the results of Heinle (1987) and Bjørnheden and Bondjers (1987), where metabolic changes were of the order of 50–100%, this order of magnitude estimate seems to represent an upper limit on the metabolic rate that can be expected in a plaque. Since Bjørnheden and Bondjers (1987) found oxygen consumption changes around 100%, $2 \times 10^3 \text{ W m}^{-3}$ seems like a likely value of the increased metabolism (a doubling of normal metabolism.)

3. Analytical models

Analytical models gives physical insight and order of magnitude estimates that can be used to validate numerical models, even though simplified geometries must be used. They are also useful in providing estimates on expected experimental results. The only model which is somewhat mathematically tractable and still realistic is a system with spherical symmetry (see appendix C).

A sphere with heat generation q and radius a can model the plaque when the blood flow has been obstructed and the perfusion in the surrounding media neglected (or stopped by the obstructed blood flow). Assuming that the sphere has thermal conductivity κ_1 , and is surrounded by an infinite medium with no heat generation and thermal conductivity κ_2 , the solutions as a function of the radial distance r of the steady-state heat equation (5) with $P = 0$ are

$$T_1(r) = \frac{q}{6\kappa_1}(a^2 - r^2) + \frac{qa^2}{3\kappa_2}, \quad (8)$$

$$T_2(r) = \frac{qa^3}{3\kappa_2 r}, \quad (9)$$

for the sphere and the surroundings, respectively.

Adding perfusion in the surrounding medium gives a more realistic model of a plaque in a vessel with obstructed blood flow, but with intact perfusion in the surrounding tissue. Assuming perfusion P in the surrounding medium (equivalent to a heat sink of PT), and thermal conductivity κ in both regions, the solutions are given by

$$T_1(r) = -\frac{qr^2}{6\kappa} + \frac{qa^2}{6\kappa} \left(\frac{2}{a\sqrt{P/\kappa} + 1} + 1 \right), \quad (10)$$

$$T_2(r) = \frac{qa^3 \exp(-\sqrt{P/\kappa}(r-a))}{3\kappa(a\sqrt{P} + 1)r}, \quad (11)$$

for the region of the heat generating sphere and the surroundings, respectively. From (11) one can define a thermal penetration depth (where the temperature has dropped by e^{-1}) in a perfused media to be

$$d = \sqrt{\frac{\kappa}{P}}. \quad (12)$$

This was used to determine the necessary size of the geometries in the numerical models so that the effects of the finite boundaries could be minimized.

If the heat producing region is embedded in a region of lower conductivity, this could produce a higher temperature in the centre of the heat producing region, due to the insulating effect of the lower conductivity material (e.g. fatty deposits). This situation can be modelled by a heat producing sphere of radius a , with thermal conductivity κ_1 , surrounded by a shell of radius $b > a$ with thermal conductivity $\kappa_2 < \kappa_1$, which again is surrounded by an infinite medium with thermal conductivity κ_1 . The solutions to this model for the three regions are from centre and out,

$$T_1(r) = -\frac{q}{6\kappa_1} \left(r^2 - a^2 \frac{b(2\kappa_1 + \kappa_2) - 2a(\kappa_1 - \kappa_2)}{\kappa_2 b} \right), \quad (13)$$

$$T_2(r) = -\frac{q}{6\kappa_2} \left(\frac{2\kappa_1 a^3}{\kappa_2 r} - \frac{2a^3(\kappa_1 + \kappa_2)}{b\kappa_2} \right), \quad (14)$$

$$T_3(r) = \frac{qa^3}{3\kappa_1 r}. \quad (15)$$

To find the increase in temperature at the centre of the plaque due to the insulating material, we can take the ratio

$$f = \frac{T_0(0)}{T_{\text{ins}}(0)} = \frac{1}{3} \left(\frac{2\kappa_1}{\kappa_2} + 1 \right) + \frac{2a}{3b} \left(\frac{\kappa_1}{\kappa_2} - 1 \right), \quad (16)$$

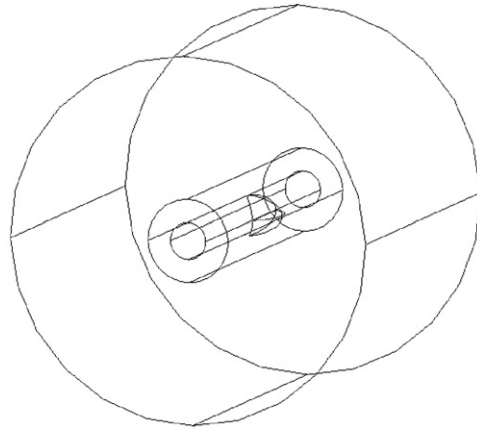


Figure 1. The geometry of the eccentric plaque. The outer cylinder has a diameter of 40 mm. The crescent shaped plaque is embedded in the middle cylinder which represents the media.

where T_0 is the solution from (8) and T_{ins} is the solution with the insulating layer from (13). Thus, the increase in temperature is proportional to the ratio κ_1/κ_2 .

4. Numerical models

Numerical models are necessary to investigate more realistic geometries, as they cannot be solved analytically. The commercial software Comsol Multiphysics (Comsol, Sweden) was used to perform the simulations. Default values for mesh densities and numerical solvers were used.

4.1. Geometry

The basic geometry of the models used in the numerical analysis consisted of a cylinder of radius 2 mm and length 40 mm, representing the lumen. Surrounding the lumen was another cylinder with thickness 3 mm and length 40 mm, representing the tunica media. Heat generating plaques with two different shapes were embedded in this region, centred along the length of the cylinder. One plaque was crescent shaped with an eccentric location. The other was shaped like a hollow cylinder placed concentrically with the vessel axis (see figures 1 and 2). The sizes of the plaques were varied in the simulations. Heat was only generated in the plaque, so the solution of the temperature T only represents the deviation from a normal temperature distribution. Outside the region representing the tunica media was a 40 mm long cylinder with radius 20 mm, which represented perfused tissue surrounding the vessel. The tunica media is large compared to real values but was chosen to facilitate the drawing of the plaque within the media for the FEM models. The effect on the calculated temperatures should be small. The size of the outer cylinder was chosen to be about two thermal penetration depths (according to (12)) to minimize the effect of the finite boundaries.

4.2. Thermal boundary conditions

The temperature deviation was fixed at $T = 0$ for all outer boundaries except at the outlet of the vessel, where the temperature flux was set to convective flow. At all other boundaries, continuous temperature and heat flux was imposed.

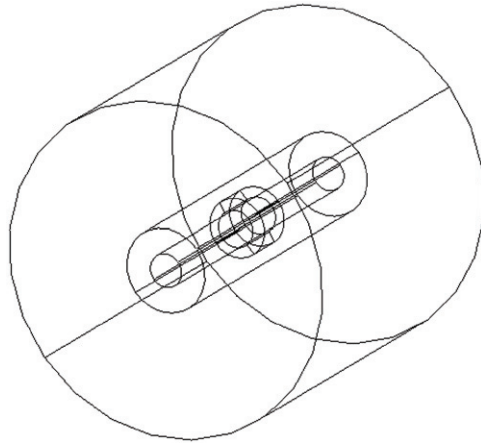


Figure 2. The geometry for the concentric plaque model. The outer cylinder has a diameter of 40 mm. The plaque is the short cylinder and is embedded in the middle cylinder which represents the media.

Numerical models must have a finite size, so boundary conditions cannot be at infinity. Applying fixed temperature boundary conditions can lead to spurious results as unlikely high heat fluxes are generated at the boundaries. To minimize the error of the boundaries, an upper limit on the acceptable flux at the boundary is that $\oint \vec{j} \cdot d\vec{A}/Q = Q_j/Q \ll 1$, where \vec{j} is the heat flux, Q is the heat generated in the system and the integration is performed over the outer surface of the model, except the outlet of the vessel. This condition states that most of the generated heat is accounted for in the system that is analysed. In all systems that were analysed (except for simulations with very low blood flow) the heat lost through the outer boundary of the system was less than 10% of the energy generated in the system, indicating that the finite boundaries will have little effect on the calculated temperatures. Furthermore, the radius of the outer cylinder (20 mm) was chosen to be larger than the penetration depth in the perfused tissue which was calculated to be $d = 12$ mm from (12).

Simulations of very low or no blood flow had higher thermal gradients at the surfaces. To determine if this would have a large impact on the solution, a numerical solution of a sphere of radius 1 mm in a perfused medium with radius 20 mm was compared to an analytic solution of a sphere in a perfused medium extending to infinity. This models the situation with no blood flow. The result is shown in figure 3. The flux through the outer boundary was $Q_j = 6.6 \times 10^{-5}$ W in the numerical calculations, and the total heat generation in the system was $Q = 8.3 \times 10^{-5}$ W. Even though the flux through the boundary accounts for a large part of the generated energy, the numerical solutions are very close to the analytic solution.

4.3. Fluid boundary conditions

The average blood velocity is about $v = 0.3$ m s⁻¹ in coronary arteries, which is fairly low compared to the dynamic viscosity ($\eta = 2.5 \times 10^{-3}$ Pa s). The Reynolds number is given by

$$Re = \frac{\rho v l}{\eta}. \quad (17)$$

Here, l is a characteristic length of the system and ρ is the density of the fluid. With $l = 2$ mm and using the density of blood from table 1 gives $Re = 500$. Usually, $Re = 2300$

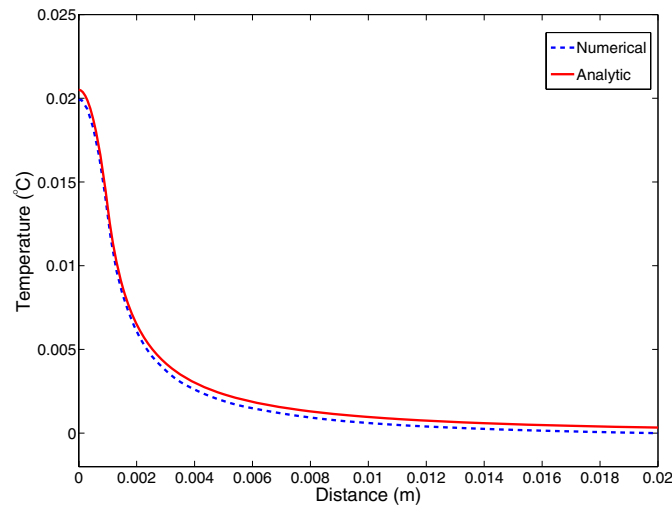


Figure 3. Difference between analytic and numerical models of a heat generating sphere. For the analytic model the surrounding medium was infinite and for the numerical model the sphere was embedded in another sphere with radius 20 mm. The graph shows the temperature as a function of distance from the plaque centre. The heat generating sphere had a radius of 1 mm. The temperature calculated by the numerical model is slightly lower due to the imposed zero temperature at the boundary (see section 4.2), but the effect of the finite boundary on the temperature is small.

is given as a limit of laminar flow. Blood was therefore modelled with a parabolic velocity profile (Poiseuille flow) with an average velocity of $v = 0.3 \text{ m s}^{-1}$ at the input and output as it would be in laminar flow. At the surfaces of the vessel the boundary condition was set to $\vec{v} = 0$ (*no slip* condition).

5. Results

5.1. Analytic models

Assume a spheroidal plaque with radius $a = 1 \text{ mm}$, with heat generation $q = 2 \times 10^4 \text{ W m}^{-3}$, embedded in an infinite medium representing the media. Using the physical properties from table 1, (8) yields a $0.025 \text{ }^\circ\text{C}$ temperature increase at the centre of the plaque.

If we now include a perfusion of $P = 3.3 \times 10^3 \text{ W K}^{-1} \text{ m}^{-3}$ in the infinite medium surrounding the plaque, the resulting temperature increase at the centre of the plaque becomes $0.020 \text{ }^\circ\text{C}$.

An insulating layer could increase the temperature in the centre of the plaque, but notice that the insulating region has no effect on the temperature distribution in the surrounding medium (compare (9) and (15)). Using a sphere with radius $a = 1 \text{ mm}$ embedded in a 1 mm thick insulating layer of fatty tissue with lower conductivity (see table 1) yields a value of $0.030 \text{ }^\circ\text{C}$ at the centre of the sphere.

5.2. Numerical models

5.2.1. Eccentric plaque. A crescent shaped, eccentric plaque, with positive remodelling into the media (no stenosis), was simulated. The geometry is shown in figure 1. Figure 4 shows variation in the highest recorded temperature in the plaque as a function of the plaque volume

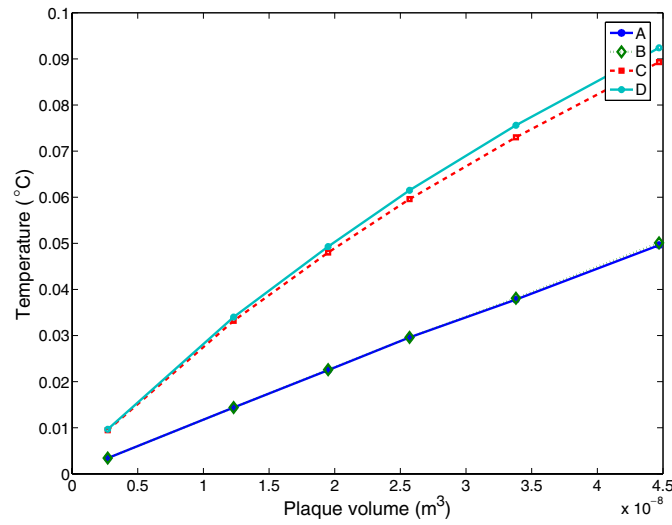


Figure 4. The highest recorded temperature in the plaque as a function of plaque volume. A: high perfusion with blood flow; B: low perfusion with blood flow; C: high perfusion with no blood flow; D: low perfusion with no blood flow. It can be seen that the blood flow in the vessel is the most important factor for the temperature in the plaque

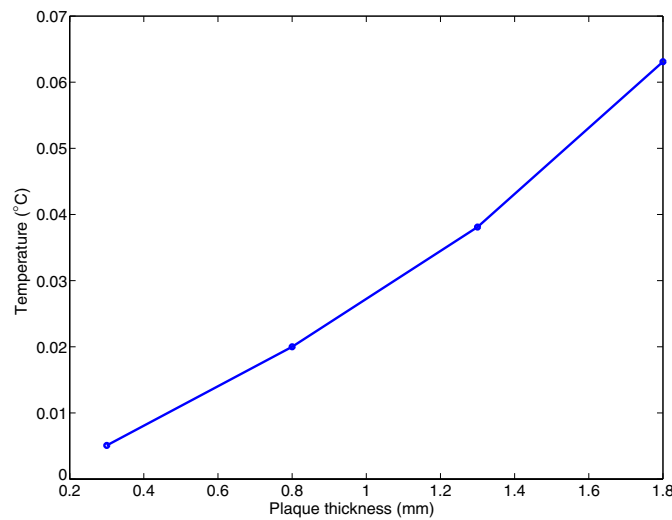


Figure 5. The highest temperature in plaque for varying thickness of a concentric plaque. The plaque thickness is the thickness of the cylinder walls that represent the plaque.

both with blood flow (0.3 m s^{-1}) and without, and with low and high perfusion ($P = 0.16 \times 10^3 \text{ W K}^{-1} \text{ m}^{-3}$ and $P = 3.3 \times 10^3 \text{ W K}^{-1} \text{ m}^{-3}$).

5.2.2. Concentric plaque. Some plaques have a concentric shape, although these are less commonly of the vulnerable type. The geometry is shown in figure 2, where the plaque is represented by the cylinder embedded in the media. Figure 5 shows the temperature in the plaque for varying thickness of the plaque. The length of the plaque was 5.5 mm.

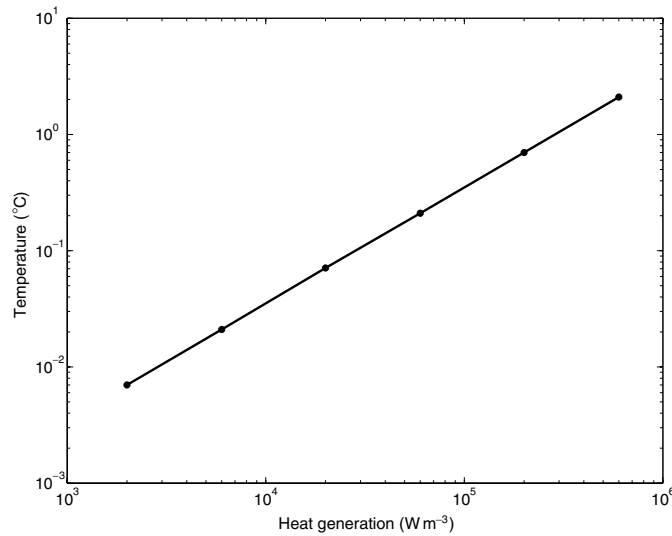


Figure 6. A log–log plot of the temperature in the centre of an eccentric plaque for varying values of heat generation in the plaque. We can see the dependence on the heat generation is linear as predicted by equation (8). The slope of the plot is $3.5 \times 10^{-6} \text{ K m}^3 \text{ W}^{-1}$.

5.2.3. Variation in heat generation. To investigate how the temperature at the centre of the plaque changes with varying metabolic rates, the heat generation in the plaque was varied between $2 \times 10^3 \text{ W m}^{-3}$ and $6 \times 10^5 \text{ W m}^{-3}$. A large eccentric plaque with volume equal to the largest plaque in section 5.2.1 was used for this simulation. The results are shown in figure 6.

5.2.4. Variation in blood flow. The average blood flow in medium sized arteries (such as the coronary arteries) is about 0.3 m s^{-1} . Due to pressure variations during diastole and systole, the velocity will vary up to 30%. The pulsation of the blood was not modelled but the upper and lower limits of the velocity were modelled and the resulting effect of the pulsating blood must necessarily lie between these upper and lower limits. In figure 7 are plots of the temperature at the surface and in the centre of the plaque for varying blood flows. Figures 8 and 9 show cross sections of the temperature distribution with and without flow in the lumen, respectively.

5.2.5. Variation in perfusion. To get the functional dependence of the perfusion, this quantity was varied from $F = 0.012 \text{ ml min}^{-1} \text{ g}^{-1}$ for fatty tissue to $F = 0.02 \text{ ml min}^{-1} \text{ g}^{-1}$ for cardiac muscle (Svaasand 1982). Using (A.1) and (A.2) we find that this corresponds to heat sinks of $q = 3.3 \times 10^3 T \text{ W K}^{-1} \text{ m}^{-3}$ and $q = 0.16 \times 10^3 T \text{ W K}^{-1} \text{ m}^{-3}$, respectively.

Arteries in the coronary tree can be surrounded either by thick adipose tissue or by cardiac muscle. These tissue types have different perfusion rates (see table 1). To see how this affects the temperature of the plaque, a large eccentric plaque was simulated with perfusion from 0 to $15\,000 \text{ W K}^{-1} \text{ m}^{-3}$. The results are shown in figure 10.

6. Discussion

It was found that the temperature change in the centre of a plaque due to increased heat generation was less than 0.1 K. We have used what we consider as an upper limit of the heat

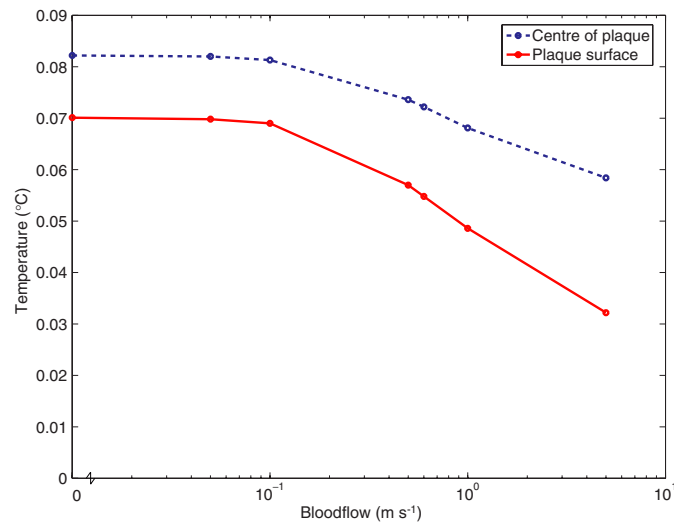


Figure 7. The variation in the temperature in the centre and at the surface of the plaque for varying blood flows from 0 to 5 m s⁻¹. The curve indicates that there is a certain threshold before the blood flow has any significant effect and that the temperature decreases linearly at high flow rates. The plaque surface is naturally more affected by the blood flow.

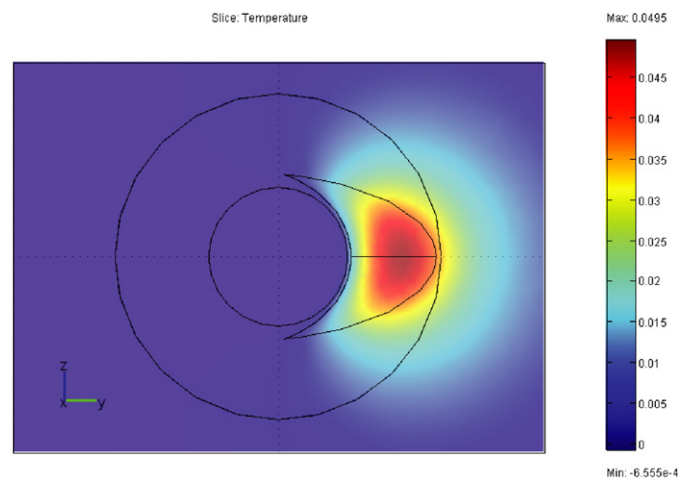


Figure 8. Thermal distribution in a vessel with flow. The temperature in the lumen is basically unaffected by the heat generation in the plaque.

generation and reported temperature values at the centre of the plaque. The temperature values at the surface of the plaque will therefore be significantly lower. This temperature seems too small to be measured accurately in the experimentally difficult environment of an artery.

6.1. Comparison of analytic and numerical results

According to (10), the temperature dependence for a sphere in a perfused medium follows an a^2 dependence on the radius of the sphere, a $1/\sqrt{P}$ dependence on perfusion, and is linear

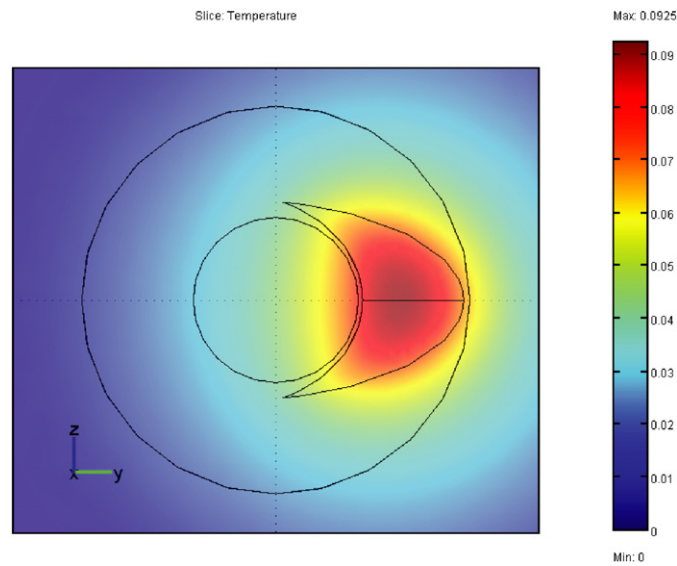


Figure 9. Thermal distribution in a vessel with no flow.

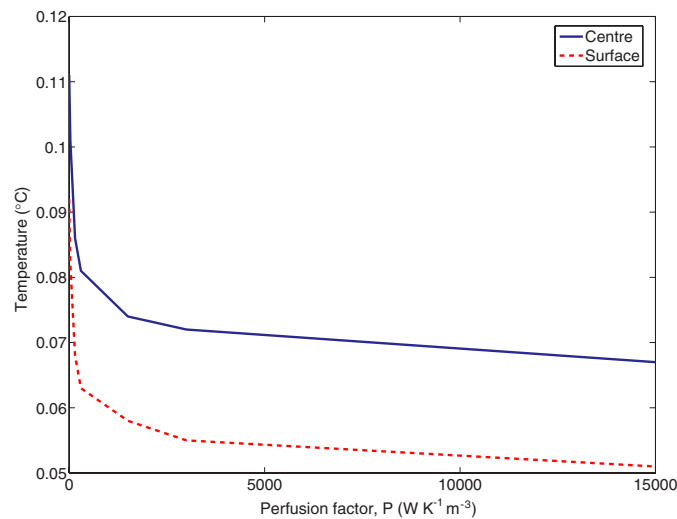


Figure 10. The plot shows the temperature in the plaque for varying degrees of perfusion in the surrounding medium. Physiological realistic values are between 160 and 3330 K⁻¹. The top graph is the highest recorded value in a plaque, and the bottom is at the plaque surface, facing the lumen.

with the heat generation q . The a^2 dependence on the radius is a $V^{2/3}$ dependence in terms of volume. In figure 4 we see that for the no-flow case, the temperature calculated from the numerical model follows a trend that is similar to the $V^{2/3}$ dependence that was expected from the analytic model. This is similar to what was reported by ten Have *et al* (2004). The differences between flow and no-flow conditions varied between 78–180%. This is higher than the values reported by Stefanadis *et al* (2003). The presence of the catheter, reducing the maximal flow compared to an empty artery, is the probable cause for this discrepancy. For

the concentric model the T -dependence in figure 5 is in terms of plaque thickness instead of volume, and it can be seen that the graph seems to follow the a^2 dependence that was expected from the analytic model.

Figure 10 shows that the temperature in the numerical results follows the $1/\sqrt{P}$ dependence as predicted by the analytic model. It can be seen in figure 6 that T is linear with q which was also predicted by the analytic model. The same dependence was also reported by ten Have *et al* (2004).

In figure 7 we can see that the nearly linear shape of the logarithmic plot above a certain threshold indicates that $T \propto \log v$, which is the same that was reported by Diamantopoulos *et al* (2003). The loss of dependence at high velocities that Diamantopoulos *et al* (2003) reported was not observed within the values simulated. However, at some point the reduction in temperature with increased velocity must necessarily decrease. Diamantopoulos *et al* (2003) found no temperature variations due to oscillations in the blood flow. This is in agreement with figure 7 from which it can be determined that a 30% variation of blood flow only changes the steady-state temperature by less than 0.01 K. The transient effect will be even smaller.

Since the analytic models compare well with the numerical models, the former are useful for easily predicting the effect that changing various parameters will have on the resulting temperature.

6.2. Heat generation

In the estimate of the heat generation in the plaque, a tissue that was assumed to be dense with macrophages was used. Since the plaque is by no means dense with macrophages, the value used in this work represents an upper bound on the heat generation. We have in this paper placed the heat generation in the plaque centre, not the cap where the macrophage infiltration usually resides. Even though the heat source will be closer to the lumen, possibly making the heat generated there easier to measure, the volume they usually occupy is smaller than the ones used in this study. The values reported in this study are of the highest temperature in the plaque, not at the surface of the vessel. The temperatures reported here thus represent an upper limit on the value that can be measured.

Using the article by Casscells *et al* (1996) to determine heat generation is very uncertain. How *ex vivo* metabolism compares to *in vivo* metabolism is unknown. It could increase due to increased oxygen supply, or decrease due to the lower availability of nutrients. In the analysis, free or forced convection was not taken into account; the article by Casscells *et al* (1996) did not contain enough information to determine these. These factors would increase the heat loss to the air, and would increase the calculated metabolic rate. Despite these uncertainties, equation (16) shows that a heat generation which can yield a temperature increase of 1 K in air will yield about 0.05 K when embedded in a tissue since the thermal conductivity is about 20-fold higher.

6.3. Causes of published values

Several studies have reported temperatures higher than the values predicted in this paper. Casscells *et al* (1996) found temperature variations above 1 °C, but as discussed in section 6.2, the low thermal conductivity of air will give higher temperatures than if the same heat generating region was surrounded by tissue.

Since it is the blood that transports heat away from the tissue and dissipates the heat through the lungs and skin, a thermal gradient must necessarily exist between the blood and tissue. The heart pumps about 5 l min⁻¹ in an adult, resting person, and can rise to about

20 l min^{-1} during heavy exercise (Tortora and Grabowski 2003). Based on the physical model of the bioheat equation (1), the blood is heated to normal tissue temperature during its pass through the capillaries. Thus, for the blood to transport away the heat Q generated by the normal metabolism, a thermal gradient must exist between the blood and the tissue. The magnitude of this can be calculated by the equation

$$\Delta T c_b \rho_b V_b = Q. \quad (18)$$

V_b is the volume of blood passing through the capillaries per unit time. Letting $V_b = 5 \text{ l min}^{-1}$ and $Q = 100 \text{ W}$ gives a temperature difference of $\Delta T = 0.3 \text{ K}$, which is the same as reported experimental values (Nybo *et al* 2002). This means that for the blood to remove the heat generated in the body, the arterial blood must have a temperature about 0.3 K below tissue temperature. Because of this thermal gradient, the thermal contact between the tissue and the temperature probe and how it is exposed to the cooler blood could have a large impact on the measured values. This could for example explain the values measured by Schmermund *et al* (2003) using a catheter from Volcano Therapeutics yielding temperatures from $0.14\text{--}0.36 \text{ K}$. The increased thermal heterogeneity that was reported for patients with stable angina, compared to a healthy vessel, could be attributed to the rough surface of a heavily atherosclerotic vessel. However, as Stefanadis *et al* (1999) points out, patients with stable and unstable angina and with acute myocardial infarction have the same degree of vessel remodelling. Thus, the effect due to probe contact should be similar in all of these, but thermal heterogeneity was still different in these patient groups. Positioning a temperature sensor in the vessel lumen will affect the measured temperatures, both through conduction along the catheter and disruption of normal blood flow. This has been investigated in detail for various catheter designs by ten Have *et al* (2006).

Another question that needs an answer is whether temperature differences in surrounding organs can affect the temperature measurements. Thermal penetration depth is defined by equation (12). Using $P = 3.3 \times 10^3 \text{ W K}^{-1} \text{ m}^{-3}$ gives a thermal penetration depth of 12 mm . Clearly, if there is temperature heterogeneity in the myocardium, this will affect the temperature along a vessel. This is not unlikely as an established diagnosis, determined from positron emission tomography, is that stenotic coronary arteries can lead to regions of the myocardium with increased metabolism but reduced perfusion. Increased metabolism and reduced perfusion will lead to increased temperature. Likewise, if the lungs, which are exposed to the much cooler ambient air, are within 12 mm of the coronary arteries, this would affect the temperature measurements. Some thermography studies have been performed on the aorta and this vessel passes diverse organs as liver, bowels and lungs which will affect the temperature.

One study has reported temperature variations that are closer to the values predicted in this paper (Toutouzias *et al* 2006).

6.4. Heat source location

We have in these studies modelled the heat generation in a plaque a certain distance below the surface. However, the macrophages in a plaque are usually reported to be in the cap and not in the lipid core. This could bring the location of the highest temperature in the plaque closer to the surface, making it easier to measure. However, since the values in the numerical studies are reported as the highest temperature in the plaque, not the temperature measured at the surface, this value will not increase. Closer to the surface the plaque could to some degree be insulated more from the perfusion but would be more strongly influenced by the blood flow. It has been reported that there is increased vasculature in the media of large plaques

which would indicate a higher perfusion rate (Davies and Thomas 1985) and more efficient removal of heat from the plaque. When flow is present in the vessel, it accounts for the largest part of the heat loss, but if the vessel is occluded, the perfusion is important for the resulting temperature.

7. Conclusions

Based on the simulations and physical parameters in this study, the temperature increase that can be expected in the centre of a plaque is less than 0.1 °C. All the reported temperatures in this study are of the highest recorded temperature in the plaque. The temperature a sensor could measure would be lower than this. The results depend on the estimated heat generation in the plaque. A value significantly larger than estimated values was chosen, so that the resultant temperatures gives an upper bound on the temperature increase that that can be expected. Temperature differences of the order of 0.5 K and higher that are reported in the literature could be due to normal temperature gradients in the body, but seem unlikely to be explained by increased metabolism in the plaque.

Acknowledgments

This work was funded by the Norwegian Research Council. The help by Dag Roar Hjelme and Andreas Meyer Winnem in preparing the manuscript is greatly appreciated.

Appendix A. Perfusion

When deriving the heat equation for a perfused medium (5) it is assumed that q_p is the energy that leaves a unit volume per unit time through perfusion. If ω is the volume of blood leaving a unit volume of tissue per unit time, then

$$q_p = \omega c_b \rho_b \Delta T, \quad (\text{A.1})$$

where ΔT is the temperature difference between the tissue and the arterial blood. The perfusion factor P is thus $P = \omega c_b \rho_b$. ω is related to other measures of blood perfusion by

$$\omega = F \rho_t = W / \rho_b, \quad (\text{A.2})$$

where F is the volume of perfused blood per unit mass of tissue per unit time and W is the mass of perfused blood per unit volume of tissue per unit time (Svaasand 1982).

Appendix B. Heat transfer by radiation

There has been some dispute on whether radiation is an important heat transfer mechanism *in vivo*. The Stefan–Boltzman law gives the transfer of energy by radiation between two objects separated by a *non-absorbing medium*. Wien's law gives the wavelength of maximum emission for a given temperature. For 37 °C, this wavelength is 9.35 μm . At this wavelength the optical penetration depth is about 17 μm (Hale and Querry 1973). Thus, if radiation is a contributing factor, one must in the Stefan–Boltzman law enter the temperature difference of objects which are of the order of 17 μm apart, which is on average how far a photon can travel without being absorbed. Using (9), we find that the temperature gradient is 13 K m^{-1} at the plaque surface of a 1 mm^3 plaque. This gives a temperature difference of two objects separated 10 μm of 1.3×10^{-5} K. Using the Stefan–Boltzman law with this temperature difference gives a heat flux due to radiation of 9×10^{-5} W m^{-2} . Using (9) to find the thermal

flux due to thermal conduction gives a value of 6.7 W m^{-2} . This is a difference of five orders of magnitude, showing that radiation is negligible.

Furthermore, in all measurements of thermal conductivity of a material the effect of heat transport by radiation will be incorporated in the measurement, so that the effect of radiation in an IR-absorbing medium is incorporated in the value of the thermal conductivity.

Appendix C. Dimensionality

Reducing dimensionality requires a symmetry plane or axis. This in effect requires an infinite plane or axis or a symmetry plane/axis so large/long that edge effects are negligible. For example, to use a polar, two-dimensional (2D) coordinate system would require that the plaque extended infinitely far along the vessel axis. This is not in general the case, and a full three-dimensional model should be used. In this study, the only geometry that could be reduced in dimension was the concentric plaque where a 2D model of a longitudinal cross section (but not the transverse) of the vessel could be used.

An example can illustrate the erroneous results that can be generated. Consider a heat generating sphere (representing the plaque) with a diameter of 1 mm embedded in an infinite medium (representing the tissue). Assume that the heat generation in the sphere is 10^4 W m^{-3} and that both regions have a thermal conductivity of $0.4 \text{ W K}^{-1} \text{ m}^{-1}$. The temperature in the centre is then, by (8), 0.0125 K in the centre of the sphere. An (incorrectly) simplified one-dimensional (1D) model of this sphere could be a 2 mm region with heat generation 10^4 W m^{-1} surrounded by a thermally conductive medium from $x = -\infty$ to $x = \infty$.

The 1D model does not even have a finite solution when the boundary condition is zero at infinity so the temperature must be set to zero at finite position. To choose this position the sphere model was used to find where the temperature had dropped by one order of magnitude. This gives 0.02 m by (9). The solution to the 1D model with heat generation from $x = -c_1$ to $x = c_1$ and zero temperature at $\pm c_2$ is

$$T_1 = \frac{q}{\kappa}(c_1^2 - x) + \frac{2q}{\kappa}c_1(c_2 - c_1), \quad (\text{C.1})$$

$$T_2 = \frac{2q}{\kappa}c_1(c_2 - x). \quad (\text{C.2})$$

The temperature at the centre of the heat generating region (the plaque) is then from (C.1) 0.97 K. We see that the answer changes by two orders of magnitude following a simplification (reduction of dimensionality) which at first sight might seem reasonable. The physical explanation is that heat flux along one or two dimensions is suppressed.

Nor does a 2D model have a steady-state solution with zero temperature at infinity. The solution in cylindrical coordinates for a disc with radius a embedded in a larger disc with radius b and using zero temperature as the boundary condition is for the inner disc,

$$T(r) = -\frac{qr^2}{4\kappa} + \frac{qa^2}{2\kappa} \left(\ln\left(\frac{b}{a}\right) + \frac{1}{2} \right). \quad (\text{C.3})$$

Setting $a = 1 \text{ mm}$, $b = 20 \text{ mm}$ and $q = 10^4 \text{ W m}^{-2}$ gives $T = 0.087 \text{ K}$, about eight times higher than the 3D model.

References

- Bjørnheden T and Bondjers G 1987 Oxygen consumption in aortic tissue from rabbits with diet-induced atherosclerosis *Arteriosclerosis* **7** 238–47

- Burton R F 2000 *Physiology by Numbers: An Encouragement to Quantitative Thinking* (Cambridge: Cambridge University Press)
- Casscells W, David M H, Krabach T, Vaughn W K, McAllister H A, Bearman G and Willerson J T 1996 Thermal detection of cellular infiltrates in living atherosclerotic plaques: possible implications for plaque rupture and thrombosis *Lancet* **347** 1447–9
- Chen M M and Holmes K R 1980 Microvascular contribution in tissue heat transfer *Ann. New York Acad. Sci.* **335** 137–50
- Cohen M L 1977 Measurement of thermal properties of human skin—a review *J. Invest. Dermatol.* **69** 333–8
- Davies M J and Thomas A C 1985 Plaque fissuring—the cause of acute myocardial infarction, sudden ischaemic death, and crescendo angina *Br. Heart J.* **53** 363–73
- Diamantopoulos L 2003 Arterial wall thermography *J. Int. Cardiol.* **16** 261–6
- Diamantopoulos L, Liu X, De Scheerder I, Krams R, Li S, Van Cleemput J, Desmet W and Serruys P W 2003 The effect of reduced blood-flow on the coronary wall temperature: are significant lesions suitable for intravascular thermography? *Eur. Heart J.* **24** 1788–95
- Dumas A and Barozzi G S 1984 Laminar heat transfer to blood flowing in a circular duct *Int. J. Heat Mass Transfer* **27** 391–8
- Felton C V, Crook D, Davies M J and Oliver M F 1997 Relation of plaque lipid composition and morphology to the stability of human aortic plaques *Arterioscler. Thromb. Vasc. Biol.* **17** 1337–45
- Gandhi O P, Lazzi G and Furse C M 1996 Electromagnetic absorption in the human head and neck for mobile telephones at 835 and 1900 mhz *IEEE Trans. Microw. Theory Tech.* **44** 1884–97
- Hale G M and Querry M R 1973 Optical constants of water in the 200 nm to 200 micron wavelength region *Appl. Opt.* **12** 555–63
- Heinle H 1987 Metabolite concentration gradients in the arterial wall of experimental atherosclerosis *Exp. Mol. Pathol.* **46** 312–20
- Lilledahl M B, Haugen O A, Randeberg L L and Svaasand L O 2005 Characterization of atherosclerotic plaque by reflection spectroscopy and thermography: a comparison *Proc. SPIE* **5686** 415–25
- Madjid M, Willerson J T and Casscells S W 2006 Intracoronary thermography for detection of high-risk vulnerable plaques *J. Am. Coll. Cardiol.* **47** C80–5
- Marsden J E 1998 *Mathematical Physiology* (New York: Springer)
- Nybo L, Secher N H and Nielsen B 2002 Inadequate heat release from the human brain during prolonged exercise with hyperthermia *J. Physiol.* **545** 697–704
- Pennes H H 1948 Analysis of tissue and arterial blood temperatures in the resting human forearm *Appl. Physiol.* **1** 93–122
- Rzeszutko L, Legutko J, Kaluza G L, Wizimirski M, Richter A, Chyrchel M, Heba G, Dubiel J S and Dudek D 2006 Assessment of culprit plaque temperature by intracoronary thermography appears inconclusive in patients with acute coronary syndromes *Arterioscler. Thromb. Vasc. Biol.* **26** 1889–94
- Schmermund A, Rodermann J and Erbel R 2003 Intracoronary thermography *Herz* **28** 505–12
- Stefanadis C 2001 Increased local temperature in human coronary atherosclerotic plaques: an independent predictor of clinical outcome in patients undergoing a percutaneous coronary intervention *J. Am. Coll. Cardiol.* **37** 1277–83
- Stefanadis C, Diamantopoulos L, Dernellis J, Economou E, Tsiamis E, Toutouzas K, Vlachopoulos C and Toutouzas P 2000 Heat production of atherosclerotic plaques and inflammation assessed by the acute phase proteins in acute coronary syndromes *J. Mol. Cell. Cardiol.* **32** 43–52
- Stefanadis C, Diamantopoulos L, Vlachopoulos C, Tsiamis E, Dernellis J, Toutouzas K, Stefanadi E and Toutouzas P 1999 Thermal heterogeneity within human atherosclerotic coronary arteries detected *in vivo*: a new method of detection by application of a special thermography catheter *Circulation* **99** 1965–71
- Stefanadis C, Toutouzas K, Tsiamis E, Mitropoulos I, Tsioufis C, Kallikazaros I, Pitsavos C and Toutouzas P 2003 Thermal heterogeneity in stable human coronary atherosclerotic plaques is underestimated *in vivo*: the ‘cooling effect’ of blood flow *J. Am. Coll. Cardiol.* **41** 403–8
- Svaasand L O 1982 Properties of thermal waves in vascular media; application to blood flow measurements *Med. Phys.* **9** 711–4
- ten Have A G, Gijssen F J H, Wentzel J J, Slager C J and van der Steen A F W 2004 Temperature distribution in atherosclerotic coronary arteries: influence of plaque geometry and flow (a numerical study) *Phys. Med. Biol.* **49** 4447–62
- ten Have A G, Gijssen F J H, Wentzel J J, Slager C J, Serruys P W and van der Steen A F W 2005 Intracoronary thermography, heat generation, transfer and detection *Eurointervention* **1** 105–14
- ten Have A G, Gijssen F J H, Wentzel J J, Slager C J, Serruys P W and van der Steen A F W 2006 A numerical study on the influence of vulnerable plaque composition on intravascular thermography measurements *Phys. Med. Biol.* **51** 5875–87

- Thom T *et al* 2006 Heart disease and stroke statistics–2006 update: a report from the american heart association statistics committee and stroke statistics subcommittee *Circulation* **113** e85–151
- Thoren S A, Monti M and Holma B 1990 Heat conduction microcalorimetry of overall metabolism in rabbit alveolar macrophages in monolayer and in suspensions *Biochim. Biophys. Acta* **1033** 305–10
- Tortora G J and Grabowski S R 2003 *Principles of Anatomy and Physiology* (New York: Wiley)
- Toutouzas K, Drakopoulou M, Mitropoulos J, Tsiamis E, Vaina S, Vavuranakis M, Markou V, Bosinakou E and Stefanadis C 2006 Elevated plaque temperature in non-culprit de novo atheromatous lesions of patients with acute coronary syndromes *J. Am. Coll. Cardiol.* **47** 301–6
- Valvano J W and Chitsabesan H F 1987 Thermal conductivity and diffusivity of arterial wall and atherosclerotic plaque *Lasers Life Sci.* **1** 219–29

Paper V

Characterization of vulnerable plaques by multiphoton microscopy

Magnus B. Lilledahl, Olav A. Haugen, Catharina Davies and Lars O. Svaasand. *Journal of biomedical optics*. *Conditionally accepted*.

Characterization of vulnerable plaques by multiphoton microscopy

Magnus Borstad Lilledahl*

Norwegian University of Science and Technology
Department of Electronics and Telecommunications
O.S. Bragstads plass 2A
7491 Trondheim
Norway
tel. +47 73591471
fax. +47 73591441
magnus.b.lilledahl@iet.ntnu.no

Olav Anton Haugen

1. St. Olavs Hospital
Department of Pathology and Medical Genetics
2. Norwegian University of Science and Technology
Department of Laboratory Medicine, Children's and Women's Health

Catharina de Lange Davies

Norwegian University of Science and Technology
Department of Physics

Lars Othar Svaasand

Norwegian University of Science and Technology
Department of Electronics and Telecommunications

Keywords: Multiphoton microscopy, atherosclerosis, vulnerable plaque.

Abstract

Cardiovascular disease is the primary cause of death in the United States, the majority of these caused by the rupture of vulnerable plaques. An important feature of vulnerable plaques is the thickness of the fibrous cap that covers the necrotic core. A thickness of less than $65\ \mu\text{m}$ has been proposed as a value that renders the plaque prone to rupture. This work shows that multiphoton microscopy can image the plaque with μm resolution to a depth deeper than $65\ \mu\text{m}$. The fibrous cap emits primarily second harmonic generation due to collagen in contrast to the necrotic core and healthy artery which emits primarily two-photon excited fluorescence from elastin. This gives a good demarcation of the fibrous cap from underlying layers, facilitating the measurement of the fibrous cap thickness. Based on a measure of the collagen/elastin ratio, plaques were detected with a sensitivity of 65% and specificity of 81%. Furthermore the technique gives detailed information on the structure of the collagen network in the fibrous cap which gives a direct measure of its mechanical strength and thus also the vulnerability to rupture.

1 Introduction

Coronary heart disease is the cause of the majority of deaths in the United States[1]. Most of these deaths are caused by coronary thrombosis occurring at an atherosclerotic plaque, leading to myocardial infarction[2]. Plaques prone to atherosclerotic thrombosis are denoted as vulnerable plaques[3]. These plaques can lead to thrombosis either by rupture of a thin fibrous cap covering a lipid core, or by erosion of the endothelium. Plaques prone to rupture are characterized by a large, lipid-rich necrotic core, covered by a thin, fibrous cap, and by infiltration of numerous macrophages[4]. The plaque cap consists mainly of collagen and a cap thickness of $<65 \mu\text{m}$ has been proposed as a value that renders the plaque unstable[5]. There is currently no clinically accepted method for detecting vulnerable plaque, but numerous detection modalities are being investigated, e.g. optical coherence tomography (OCT), magnetic resonance imaging, intravascular ultrasound (IVUS), near infrared spectroscopy and computed tomography[3].

Autopsy studies have shown that there exist several vulnerable plaques in the coronary tree in addition to the culprit lesion[5]. This has led to the hypothesis that perhaps a more detailed stratification of plaque vulnerability is necessary to determine which plaque is the most likely to rupture. For example, polarization sensitive OCT has been proposed as an improvement over conventional OCT[6]. The birefringence of collagen in the fibrous cap will affect the polarization of the light, which can be used to infer properties about the fiber structure. Another way to collect additional information, is to improve the resolution of the imaging modality. In the same way that OCT improves the resolution by an order of magnitude compared to IVUS[7] ($100 \mu\text{m} \rightarrow 10 \mu\text{m}$), multiphoton microscopy (MPM) can improve the resolution by another order of magnitude ($10 \mu\text{m} \rightarrow 1 \mu\text{m}$). The increase in resolution with MPM compared to OCT is accompanied by a decrease in penetration depth, usually reported to be a few $100 \mu\text{m}$ in biological tissue even though one study reported a penetration depth of 1mm [8].

Multiphoton microscopy uses the nonlinear optical properties of tissue and can achieve three dimensional microscopy. Second order nonlinear optical phenomena depend quadratically on the intensity of the light, so that for a focused beam the signal is only generated in a small volume around the focus. The longer wavelength of the light used in MPM also gives increased penetration depth and reduced out-of-focus photobleaching compared to conventional laser scanning microscopy.

In biomedical application, the most common nonlinear effects used for microscopy are second harmonic generation (SHG) and two-photon excited fluorescence (TPEF). SHG is generated by noncentrosymmetric molecules such as collagen, and autofluorescence generated by two-photon excitation is seen from collagen, elastin and cellular components[9]. Elastin is abundant in the media of the aorta and collagen is the primary component in the cap of atherosclerotic plaques. MPM may thus be used to study the formation and progression of atherosclerotic plaques. In addition, it could have other applications in the management of cardiovascular disease, e.g. to monitor restenosis after stenting, and assess the effect of medication.

An advantage of MPM over regular histology is that it can be performed on intact tissue, and carries the promise of in-vivo monitoring of atherosclerotic plaques which is of great clinical value. A catheter-based intravascular

microscopy probe could be developed along the lines of existing intravascular OCT probes, but with additional scanning optics[10]. Several miniaturized, intra-vital microscopes for MPM have been tested[11, 12, 13, 14, 15]. However, for intravascular applications, further minaturization is necessary, which could be realized by microoptical devices.

The goal of this study is thus to investigate the physiological information of the vascular structure that can be detected by MPM, and to what degree healthy vessels and atherosclerotic lesions can be classified compared to histological classification[16, 17, 18]. The spectral response of various tissue structures is reported and penetration depths in tissue in various pathological states are found. Photobleaching and photodamage can be incurred in tissue during laser irradiation, and these processes are investigated as their understanding is necessary to develop a safe in-vivo imaging modality.

2 Materials and Methods

2.1 Materials

Eight specimens of human aortas were excised during autopsy from 8 different patients (54.5 ± 10.9 years, 5 male, 3 female). The samples were put in closed containers, with some tissue paper soaked in phosphate buffered saline (the tissue samples were not in contact with the paper tissue) and stored at 4°C . Measurements were performed 1.45 ± 1.75 days after autopsy.

After microscopy the samples were fixed in formalin and embedded in paraffin. Thin sections were cut and stained with Hematoxylin-Eosin-Saffron (HES), Elastica and Van Gieson. HES stains cell nuclei black, cytoplasm pink, and connective fibers yellow. Elastica stains elastic fibers dark purple. Van Gieson stains muscle cells yellow and connective fibers red.

2.2 Instrumentation

The samples were investigated using a laser scanning inverted microscope (Zeiss LSM 510 Meta). Excitation was provided by a Ti:Sapphire laser (Coherent Mira, model 900 F), pumped by a 5W solid state laser (Coherent Verdi). The output of the Ti:Sapphire laser was about 750 mW, mode-locked at 800 nm. All the measurements were performed at 800 nm except the measurements described in section 2.3.3 where the wavelength was tuned from 800 nm to 840 nm in 10 nm increments. A plan-apochromat 40x 1.2 NA water immersion objective was used in all the measurements. An acusto-optic modulator (AOM) was used to regulate the power output. A setting of the AOM at 80%, which was used in all the measurements unless otherwise noted, gave about 20 mW at the objective. Laser power was measured by a Coherent LM-10 laser meter. The microscope was equipped with a Zeiss metadector, which uses a grating to disperse the generated light to 32 different channels in the spectral range from 377 nm to 710 nm at about 10 nm intervals. For all the measurements SHG was collected at 387-409 nm and TPEF at 473-505 nm, except for the measurements in section 2.3.3 where the signals were collected separately in each of the 32 channels. All measurements were performed in the reflection mode (epi-collection).

The emitted fluorescence of a solution of fluorescein (280 μM) was measured in the microscope and compared with the one-photon fluorescence of the same solution, measured in a spectrofluorimeter (Fluorolog 3 Jobin Yvon, The Horiba Group). Since the normalized spectra overlapped well with mean deviation of 5%, no further spectral calibration of the emission signals was performed.

The transmission in the system was measured by comparing the power at the laser output and at the objective for wavelengths from 800-840 nm to give the relative transmission,

$$T_r(\lambda) = \frac{P_{obj}(\lambda)}{P_{las}(\lambda)} . \quad (1)$$

This was used to calibrate the spectral measurements (see section 2.3.3 for details).

2.3 Study protocol

2.3.1 Sample preparation

The aorta samples were cut into pieces of about 5 x 5 mm for microscopic investigation. Out of the 8 aorta specimens, a total of 24 smaller samples were obtained. The samples were placed in a glass well with the lumen side of the vessel facing the coverglass. In the following, x and y will refer to the axes parallel to the lumen, and z to the axis perpendicular to the lumen.

2.3.2 Image collection

Selection of measurement sites

The sample holder was placed in the microscope and a scan over an area covering 2.3 mm x 2.3 mm was carried out. Based on these images, three primary measurement sites were defined as well as three reference sites. The measurements in the remainder of this section and section 2.3.3 were then performed on each of the primary measurement sites. The images collected at each site covered an area of 230 x 230 μm . The reference sites were shifted 115 μm from the primary sites, thereby covering half of the primary measurement sites, and thus served as an indication of whether any changes had occurred in the tissue during the study protocol. Images of the reference sites were collected at the beginning and end of the protocol.

Z-stack of images

At each of the primary measurement sites, a z-stack of images was collected. Each image covered 230 x 230 μm , and frames were collected at 4 μm intervals in the z -direction. The average SHG and TPEF intensities, $I_s(z)$ and $I_t(z)$, were calculated for each frame to determine how the generated signals varied as a function of z . $I_s(z)$ and $I_t(z)$ were normalized by dividing by their maximum value, $I_{s,max}$ and $I_{t,max}(z)$, respectively,

$$I_{s,norm}(z) = \frac{I_s(z)}{I_{s,max}} \quad I_{t,norm}(z) = \frac{I_t(z)}{I_{t,max}} . \quad (2)$$

The depth z where $I_{s,norm}(z)$ and $I_{t,norm}(z)$ had dropped to e^{-1} was determined.

At structures within the stack that were deemed interesting, single plane images were collected at higher resolution and longer acquisition times.

At a slice approximately 25 μm below the surface, the number of pixels covered by fibrous structure was counted. This depth was chosen so that no surface would be present in the images due to tilted image plane or surface irregularities, and to ensure that the signal was still strong. A few images were manually investigated to determine the background signal. The background signal was defined as the signal level in regions of the images where no fibrillar structure could be perceived, and determined to be 30 (out of 255) in the SHG images and 50 (out of 255) in the TPEF images. These values were then used as cut-off values for thresholding the images into regions containing fibrous structure, and regions defined as background. The ratio of SHG to TPEF was used as a measure of a collagen-to-elastin ratio $R_{c/e}$, and was computed as the ratio of the number of pixels N with values above threshold.

$$R_{c/e} = \frac{N_{SHG}}{N_{TPEF}} \quad . \quad (3)$$

Cross-sectional images

Cross sectional images in the x, z and y, z planes were collected. Each line parallel to the surface was 230 μm and each line was collected with a z interval of 0.46 μm . The gain of the detectors was increased through the scan to improve signals from deeper layers without saturating the signal at the surface.

2.3.3 Spectral response

At each primary site, the signal from one image frame was collected in each of the 32 channels of the spectral detector. The excitation light was tuned from 800 to 840 nm in 10 nm intervals. The excitation power, $P_l(\lambda_{ex})$, was measured at the output of the laser for each wavelength and the resulting spectra were calibrated by dividing by $(P_l(\lambda_{ex})T_r(\lambda_{ex}))^2$. The images were 230 x 230 μm . The adjustment of gain and offset were kept constant for all the spectral measurements of the samples.

2.3.4 Photobleaching and photodamage

To investigate the response of the tissue to long illumination times at various excitation powers, an area of 115 x 115 μm was scanned 200 times and the image was stored for each scan. Each scan took 1.97 s. The imaging plane was placed 10-20 μm under the surface. The laser power was varied from 50-100% in increments of 10%, which corresponded to about 10-35 mW at the objective. If structural tissue changes were severe, the imaging series was halted before the 200 scans were completed. After the procedure had been completed a z-stack of images through the damage was collected. These images were collected with a frame size of 230 x 230 μm to assess the lateral and transversal extent of the photodamage.

Finite element analysis (FEM) of the thermal distribution in the tissue was performed to determine whether thermal changes in the tissue were incurred due to 1-photon or 2-photon absorption. Details of the analysis are given in appendix A.

3 Results

3.1 General features

SHG and TPEF images demonstrated different structures and distributions of connective fibers. The SHG in the images is due to collagen, and fibrous structures with TPEF, but without SHG, was interpreted as elastin. SHG is shown in red and TPEF in green in all the images. All the presented images have been processed to enhance contrast, so signal levels between SHG and TPEF can therefore not be compared directly.

Normal arteries were defined by no intimal changes observed in the histological images (see Fig. 1d-f). Thus, atherosclerotic lesions of type I - III according to the American Heart Association (AHA) classification are included in this group[17]. These early lesions are recognized by increased lipid content but without intimal disruptions.

In the MPM images of normal arteries, individual elastin fibers could be seen clearly down to a size of about $1\ \mu\text{m}$. The structure of the fibrous network varied but some general features were observed. On the surface a thin layer of elastic fibers over a layer of collagen was observed (Fig. 1a). Below one or more of these layers was a layer of thicker, ordered elastic fibers with some scattered thicker collagen fibers (Fig. 1b). Next, a layer of thin, ordered elastic fibers was found, where the fibers were oriented at 90 degrees to the above layer (Fig. 1c). In the cross sectional images, layers of elastic laminae could clearly be distinguished (Fig. 2a). The large scale images ($2.3 \times 2.3\ \text{mm}$) had lower resolution than the other images, but yielded structure information about the connective fibers at a different size scale (Fig. 3a).

Atherosclerotic plaques were classified macroscopically by being clearly raised from the surrounding lumen surface and where the histological images showed the presence of a collagen cap over a lipid core (Fig. 4d-f). This corresponds to type V plaque in the AHA classification (fibroatheroma).

In the MPM images of the cap of an atherosclerotic plaque, the collagen appeared in thick bundles, in a non-directional structure (Fig. 4a), and were different from the collagen fibers seen in the normal vessel. There was significantly more collagen in the plaque cap than in the normal aorta. Small, round, fluorescent objects of various sizes could be seen clustered in the spaces between the collagen fibers. Plaques with a macroscopically yellow color seemed to have more of these fluorescent objects, though this was not confirmed quantitatively. In one instance the fibrous cap of a highly developed plaque was dissected, exposing the lipid core. The inside of the plaque was placed against the coverglass and the resulting image is shown in Fig. 4b. Many fluorescent objects with various sizes and shapes can be seen. The large scale images also showed such fluorescent objects and in this image their location relative to the collagen fibers can be seen (Fig. 3b). The fibers seem to have some directional orientation at this scale.

Calcified plaques (type Vb) were recognized macroscopically by very hard areas and in the histological images by an empty area surrounded by a dark purple color in the HES stained images. An MPM image of a calcification can be seen in Fig. 4c. These areas exhibited very strong TPEF and only a non-fibrillar structure could be seen. Some SHG could be seen within the calcification.

3.2 Spectral response

The spectrum of collagen was obtained from an image rich in collagen, seen by strong SHG. The image obtained with 800 nm excitation was used to define regions in the image as collagen. Pixels where the SHG was greater than half of the SHG from the pixel with the maximum value were defined as collagen. The same pixels were used to obtain the spectra at all excitation wavelengths (Fig. 5a).

The spectra of elastin were found by defining a region of interest (ROI) in an image where fibers exhibiting TPEF could be seen, but where there was no fibrillar structure in the SHG (i.e. only background). The spectra were extracted from the pixels within this ROI (Fig. 5b).

A ROI that only contained the non-fibrillar structure related to calcifications were used to extract the spectra of the calcification (Fig. 5c). The TPEF signal from the calcification was very strong so excitation power was reduced by setting the AOM to 70% when measuring the spectra to avoid saturation.

The autofluorescence from the objects seen in the lipid core were strong compared to the signal from the connective tissue (Fig. 4b). A spectrum of one of the fluorescent objects within the fibrous cap was extracted by defining a ROI that only contained one of these objects and is shown in Fig. 5d. This is markedly different from the autofluorescence from the connective fibers.

3.3 Penetration depth

The depth where maximum signal was found, and the depth where the normalized signal had fallen to e^{-1} were determined as described in section 2.3.2. The samples were classified into normal vessel and fibroatheromas based on histology, according to the description in section 3.1. For each of these classes, the mean values of the depth of the maximum signal and the depth where the normalized signal had fallen to e^{-1} were determined. These values are plotted in Fig. 6.

3.4 Collagen-elastin ratio

By defining that the presence of a fibrous cap is detected by a collagen-elastin ratio $R_{c/e}$ of greater than one, the MPM images could be used to detect the presence of a plaque with a sensitivity of 65% and a specificity of 81% with histology as the reference (14 plaques and 9 normal samples. Calcified plaques were excluded). Sensitivity was defined as the number of detected plaques minus the number of false negatives divided by the total number of plaques. The specificity was defined as the number of plaques detected minus the number of false positives divided by the total number of plaques. The average value of $R_{c/e}$ for samples classified as normal was 0.44, and 16.5 for plaques.

3.5 Photobleaching and photodamage

The reference sites were displaced 115 μm from the primary measurement sites, thereby containing half of the primary measurement sites (which were 230 x 230 μm). No changes could be seen in these images at the end of the study protocol.

During the measurements described in section 2.3.4 significant bleaching and tissue changes were incurred. After some time bubbles appeared in the images

and increased in size with time (Fig. 7a). The higher the incident powers, the earlier the bubbles appeared (within a few seconds), and the faster they grew. The z-stacks of images collected about 30 minutes after the bleaching/heating procedure indicated that the bubbles caused irreversible damage (Fig. 7b). They also showed that damage was confined closely to the illuminated area and that damage could only be seen in a layer 15-20 μm thick.

A finite element model of the temperature distribution in the tissue was developed (see appendix A). Based on this model, it was shown that the temperature is close to the steady state temperature within one second (Fig. 8b). Since the equation of heat (Eq. (4)) is linear, the shape of the time development is independent of the amount of heat generated as long as it is similarly distributed. Increasing the heat generation will only raise the graph vertically. The bubbles, however, appeared as late as after 30-40 s for low excitation powers. The spatial distribution of the temperature around the focus for linear absorption and second order absorption can be seen in Fig. 8a.

Such a system, where there is a process with a given rate (defined as the inverse of the time of the appearance of bubbles) which is a function of temperature (defined to be proportional to the square of the incident power) can be described by an Arrhenius type equation. An Arrhenius plot of the inverse of the time of bubble formation versus the inverse of the incident power squared, is plotted in Fig. 8d.

4 Discussion

4.1 Tissue characterization

MPM can detect caps of atherosclerotic plaques without exogenous staining, and with good contrast compared to healthy vessels. Images can be collected down to a depth of $>65 \mu\text{m}$, providing a measure of one of the key features of vulnerable plaques. Three dimensional images with μm resolution of the structural protein network can be generated without having to cut numerous histological sections, yielding important information on the mechanical strength of the cap.

SHG is only generated by fibrillar collagen in biological tissue[19]. The strong SHG from the plaque cap, known to be rich in collagen I and III, confirms this (Fig. 2b)[18]. We have therefore assumed fibrillar structure producing SHG to be collagen. The SHG that can be seen in the spectra other than collagen could be background signal generated at various surfaces within the optical system as SHG is known to be generated at interfaces (Fig. 5b-c).

TPEF on the other hand are seen from many biological structures. The autofluorescence spectra of elastin and collagen are very similar (Figs. 5a and 5b). This is in agreement with another study that found significant spectral overlap in the autofluorescence from collagen and elastin[20]. This study reported that elastin had a fluorescent peak at 495 nm and cellular components at 510 nm[20]. These peaks can be seen in our spectra but are present in both collagen and elastin spectra, rather than directly related specifically to elastin or cellular components (Fig. 5). Based on the abundance of autofluorescent fibers in healthy elastic artery (Fig. 1) and previous studies on cardiovascular structures[20, 21], fibrous structures without SHG but with TPEF were classified as elastin. An-

other study on atherosclerotic mice found that collagen had autofluorescence in the blue part of the spectrum whereas elastin gave autofluorescence covering a wider spectral range, which does not agree with our results[21]. Some TPEF without SHG were seen from fibers in the plaque cap (Fig. 4a). This autofluorescence seemed to come from the surface of the collagen fiber bundles. Whether this is due to elastin fibers or collagen not generating SHG has not been determined.

The thin, disorganized elastic fibers seen at the surface of the healthy vessels probably belong to the subendothelial connective tissue, while the thicker ordered layers are the elastic laminas (Fig. 1a-c). Scattered collagen fibers can be seen, apparent in Fig. 3a.

The structure of the fibrous cap could be imaged at several levels of detail (compare Fig. 4a and Fig. 3b). This fibrous structure is directly related to the mechanical strength of the plaques, and might yield some insight into why some plaques rupture and others do not. The structure of the collagen fibers can perhaps also be used to better understand the nature of the signals collected by polarization sensitive OCT.

The origin of the fluorescent objects seen in the fibrous caps and lipid cores have not been determined but could arise from several sources. In the plaques the objects seem to be clustered in small groups between the collagen fibers (Fig. 4a). This could be foam cells (macrophages with intracellular lipid droplets). The lipid core is mainly necrotic and the fluorescent objects seen here appear in different sizes which could be related to extracellular lipid droplets (Fig. 4b). The abundance of the fluorescent objects within the yellow plaque and within the plaque core supports the hypothesis that these objects are related to lipid-related substances. Blankenhorn reported strong, green one-photon autofluorescence from the lipid core of atherosclerotic plaques and related this to carotenoids which are known to be lipophilic[22]. Another study found one-photon autofluorescence from various biochemical components known to be present in atherosclerotic plaques, e.g. oxidized lipoproteins and cholesterol esters, further supporting the hypothesis that that TPEF signal is related to lipid-rich substances in the plaques[23]. The autofluorescence from some of the unidentified objects that were observed in the plaque caps had a fluorescent peak at 575 nm (Fig. 5d). Since the images collected in this study, except the spectral measurements, measured the fluorescence in the interval from 473 nm to 505 nm, the objects with a fluorescent peak at 575 were probably not detected. The strong TPEF from the lipid core could further enhance the demarcation between the fibrous cap and the lipid core. However, all the plaques imaged in this study had plaques thicker than the penetration depth of the system, so this was not confirmed.

The spectral calibration of the metadetector with fluorescein was limited by low signals below 475 nm and above 625 nm, so that inaccuracies might exist in these parts of the spectra. Furthermore since the spectra were generated at different depths and the excitation power decreases with depth, the intensity of the measured spectra can not directly be compared.

The technique was able to differentiate normal vessels from atherosclerotic plaques based on the collagen/elastin ratio with fairly good sensitivity and specificity (65% and 81% respectively). The erroneous classifications were due to some samples with high collagen content in the intima even though they appeared normal in the histological sections. In one instance the fibrous cap was

only visible down to a depth of 20 μm in the MPM images, even though a thick cap was seen in the histology. This also generated an erroneous classification. A limitation of these values is that the same observer performed both classifications and was only blinded to the histological results and not vice versa. Another limitation of the study is that the position of the MPM measurements and histological sections are not necessarily colocalized in the samples.

The collagen/elastin ratio, $R_{c/e}$, could be calculated for each layer in the vessel wall yielding an image of the fibrous cap since this type of tissue has a much higher value of $R_{c/e}$ compared to the normal vessel. An important feature $R_{c/e}$ is the large difference in its value between the vessels classified as normal and those classified as plaque, mean values of 0.44 and 16.5, respectively. This is more than an order of magnitude difference in the signal and could yield improvements over methods like OCT and ultrasound where contrast in the signal between different tissue types is often a limiting factor.

Imaging was achieved down to a depth of about 100 μm which represents the upper layers of the relatively thick aorta (2-3 mm) (Fig. 6). The coronary arteries are much thinner so that more of the vessel anatomy could be imaged. The penetration depth in tissue is determined by scattering, which reduces the power at the focus, and dispersion which degrades the pulse shape at the focus. The effect of scattering can be reduced by using an objective with a smaller numerical aperture, albeit at a loss in resolution. However, the generated signal will be lower since a less tight focusing will reduce field intensities, resulting in less second order processes. The best trade off will thus depend on the resolution necessary for the application at hand.

Since scattered photons do not affect the collected signal (as they do in OCT), the loss due to scattering can to some degree be compensated for by increasing the excitation power. Of course, availability of laser sources and heating due to linear absorption will limit this approach. However, as was observed in this study, the heat damage seems to arise from a second order process, so the reduction in light at the focus due to scattering can be compensated for by increasing the incident power without creating tissue damage.

The penetration depths reported in this study do not necessarily compare to in-vivo values. As described by Zoumi et al. the fiber structure changes significantly under physiological pressures and thereby also the scattering[20]. Also, the present study investigated the aorta, and values for the coronary arteries could be different. One feature of vulnerable plaques is a fibrous cap thinner than 65 μm , so this feature of vulnerable plaques can be detected with MPM.

4.2 Photobleaching and photodamage

Significant photobleaching was observed during the procedure described in section 2.3.4. Photobleaching was seen to strongly affect the TPEF signal. The SHG signal also decayed during the procedure, albeit at a slower rate. After a certain time, dependent on the incident power, bubbles appeared in the images. The photodamage was incurred in a very narrow region, only 15-20 μm deep, indicating that the damage arises from second order absorption. This can be appreciated from the spatial dependence of the temperature determined from the finite element model (Fig. 8b), where the assumption of second order absorption better describes the extent of the photodamage. Using reported values

of linear absorption in the aorta yielded a maximum temperature increase of 2.3 K after 200 s. In this case we assumed that convection at the upper surfaces kept the surface temperature close to the temperature of the surrounding air, so that fixed temperature was used as the boundary condition. We also used thermal insulation as the boundary condition for all the surfaces, resulting in a temperature increase of 8.8 K after 200 s. These temperatures seem too small to generate the observed bubble formation, further indicating that nonlinear absorption is the primary source of the damage.

The bubble formation could be due to gas release of absorbed gases in the tissue due to the reduction in the amount of gas that can be dissolved in the tissue with increasing temperature. This process must be well understood before a clinical tool can be developed, so that excitation powers can be kept well within safe levels.

5 Conclusion

MPM can assess tissue structure at a resolution not achievable by other imaging modalities for atherosclerotic plaque. Fibrous cap can be imaged to a depth of $>65 \mu\text{m}$ with good contrast compared to underlying layers, thereby measuring one of the key characteristics of vulnerable plaque. The mechanical stability of a vulnerable plaque is directly related to the likelihood of rupture. The network of collagen fibers is what determines the mechanical stability and this can be imaged by MPM.

Several characteristic physiological features of vessels can be seen with MPM, e.g. elastic laminae and collagen fibers in the plaque cap. All images in this study were collected in the reflection mode and the technique can therefore be transferred to an in-vivo intravascular imaging modality. The information could have important applications, both clinically, and in pathophysiological research.

A Finite element model

A FEM model was used to find the temperature distribution in the samples during irradiation. A commercial software (Comsol multiphysics, Comsol AB, Sweden) was used to perform the analysis. Default settings for mesh densities and solvers were used.

The equation to be solved to find the temperature T is the heat equation,

$$\nabla^2 T - \frac{1}{\chi} \frac{\partial T}{\partial t} = -\frac{q}{\kappa} \quad , \quad (4)$$

where $\chi = \frac{\kappa}{\rho c_p}$ is the diffusivity. κ is the thermal conductivity, ρ the density and c_p the specific heat. See table 1 for the values used in the model. q is the heat generation per unit volume per unit time, see below for values used.

A water immersion objective with $\text{NA} = 1.2$ was used in the measurements and this yields a cone of illumination with angle to the illumination axis of about 60 degrees. We will assume that the shape of the beam is a perfect cone so that the radius of the cone is given by $r = \sqrt{3}\Delta z$ where Δz is the distance from the focus. This geometrical optics approximation to the light distribution is not valid near the focus, but since we are scanning the beam over a large area,

and only looking for approximate solutions, the details of the light distribution near the focus is not important. Since the beam is scanned over an area with sides $a = 115 \mu\text{m}$ the total area illuminated by the beam a distance Δz from the focus is $A_t = \pi(\sqrt{3}\Delta z)^2 + a^2 + 4\sqrt{3}\Delta za$. The area of a cross-section of the cone perpendicular to the illumination axis is $A_c = \pi(\sqrt{3}\Delta z + 0.25\mu\text{m})^2$. The term $0.25 \mu\text{m}$ is added for the finite waist size of the beam at the focus.

The change in intensity due to absorption in a layer Δz (i.e the heat generated per area per time) is given by $\Delta I = \mu_a^{(1)} I \Delta z$, where $\mu_a^{(1)}$ is the linear absorption coefficient. Since $I = \frac{P}{A_c}$, the heat generated per unit volume per unit time is then

$$q = \frac{\Delta I A_c}{A_t \Delta z} = \frac{\mu_a I \Delta z A_c}{A_t \Delta z} = \frac{\mu P(z)}{A_t}. \quad (5)$$

For two-photon absorption the absorption is quadratic in the intensity so that $\Delta I = \mu_a^{(2)} I^2 \Delta z$, where $\mu_a^{(2)}$ is a nonlinear absorption coefficient. The heat generated per unit volume per unit time is then,

$$q = \frac{\mu^{(2)} P(z)^2}{A_c A_t}. \quad (6)$$

Eq. (5) and (6) were used for the heat generation in the FEM models. Since the beams are focused and not collimated the absorption coefficients should include a factor between 1 and 2 due to the increased pathlength but this was not taken into account. The reported values should be interpreted with this in mind. Linear absorption and scattering coefficients of human aorta tissue are $\mu_a = 80 \text{ m}^{-1}$ and $\mu_s = 250 \text{ m}^{-1}$ [24]. Values reported in the literature vary but we have used the highest value found. The power as a function of distance from glass/tissue interface z was thus described by $P = P \exp(-(\mu_a + \mu_s)z)$.

The geometry (see Fig. 8c) consisted of a disc with radius 5 mm, thickness $170 \mu\text{m}$, made of glass, representing the coverglass. The tissue was modeled as box with sides $4 \times 4 \times 2 \text{ mm}$, with the light cone inscribed. The boundary condition at the bottom of the glass was set to thermal insulation while all other boundaries were set to constant temperature.

Using the reported value of the linear absorption coefficient yielded a maximum temperature increase of 2.3 K after 200 s. The nonlinear absorption coefficient is not known but the normalized temperature distribution near the focus is shown in Fig. 8a. The temperature as a function of time is shown in Fig. 8b. The structure was also simulated with all boundaries set to thermal insulation which resulted in a temperature increase of 8.8 K after 200 s.

Acknowledgments

The authors would like to thank the following people for invaluable assistance: Edrun Andrea Schnell, Thor Bernt Melø, Arne Eriksson, Unn Granli, Lise Lynsnes Randeberg and Eivind La Puebla Larsen. This work was funded by the Norwegian Research Council.

References

- [1] T. Thom, N. Haase, W. Rosamond, V. J. Howard, J. Rumsfeld, T. Manolio, Z.-J. Zheng, K. Flegal, C. O'Donnell, S. Kittner, D. Lloyd-Jones, D. C. Goff Jr., Y. Hong, R. Adams, G. Friday, K. Furie, P. Gorelick, B. Kissela, J. Marler, J. Meigs, V. Roger, S. Sidney, P. Sorlie, J. Steinberger, S. Wasserthiel-Smoller, M. Wilson, and P. Wolf, "Heart disease and stroke statistics—2006 update: A report from the american heart association statistics committee and stroke statistics subcommittee", *Circulation* **113**(6), pp. e85–151, (2006).
- [2] M. J. Davies and A. C. Thomas, "Plaque fissuring—the cause of acute myocardial infarction, sudden ischaemic death, and crescendo angina", *British Heart Journal* **53**(4), pp. 363–73, (1985).
- [3] R. Waksman and P. W. Serruys, eds., *Handbook of the vulnerable plaque*, Taylor and Francis, London, (2004).
- [4] C. V. Felton, D. Crook, M. J. Davies, and M. F. Oliver, "Relation of plaque lipid composition and morphology to the stability of human aortic plaques", *Arterioscler. Thromb. Vasc. Biol.* **17**, pp. 1337–1345, (1997).
- [5] A. P. Burke, A. Farb, G. T. Malcom, Y.-H. Liang, J. Smialek, and R. Virmani, "Coronary risk factors and plaque morphology in men with coronary disease who died suddenly", *N. Engl. J. Med.* **336**(18), pp. 1276–1282, (1997).
- [6] S. D. Giattina, B. K. Courtney, P. R. Herz, M. Harman, S. Shortkroff, D. L. Stamper, B. Liu, J. G. Fujimoto, and M. E. Brezinski, "Assessment of coronary plaque collagen with polarization sensitive optical coherence tomography (PS-OCT)", *International Journal of Cardiology* **107**(3), pp. 400–409, (2006).
- [7] M. E. Brezinski, G. J. Tearney, B. E. Bouma, J. A. Izatt, M. R. Hee, E. A. Swanson, J. F. Southern, and J. G. Fujimoto, "Optical coherence tomography for optical biopsy: Properties and demonstration of vascular pathology", *Circulation* **93**(6), pp. 1206–1213, (1996).
- [8] P. Theer, M. T. Hasan, and W. Denk, "Two-photon imaging to a depth of 1000 micrometers in living brains by use of a Ti:Al₂O₃ regenerative amplifier", *Opt. Lett.* **28**(12), pp. 1022–1024, (2003).
- [9] E. Brown, T. McKee, E. diTomaso, A. Pluen, B. Seed, Y. Boucher, and R. K. Jain, "Dynamic imaging of collagen and its modulation in tumors in vivo using second-harmonic generation", *Nature Medicine* **9**(6), pp. 796–800, (2003).
- [10] J. G. Fujimoto, S. A. Boppart, G. J. Tearney, B. E. Bouma, C. Pitris, and M. E. Brezinski, "High resolution in vivo intra-arterial imaging with optical coherence tomography", *Heart* **82**(2), pp. 128–133, (1999).
- [11] F. Helmchen, M. S. Fee, D. W. Tank, and W. Denk, "A miniature head-mounted two-photon microscope: High-resolution brain imaging in freely moving animals", *Neuron* **31**(6), pp. 903–912, (2001).

- [12] D. Bird and M. Gu, “Compact two-photon fluorescence microscope based on a single-mode fiber coupler”, *Opt. Lett.* **27**(12), pp. 1031–1033, (2002).
- [13] F. Helmchen, “Miniaturization of fluorescence microscopes using fiber optics”, *Experimental Physiology* **87**(6), pp. 737–745, (2002).
- [14] J. C. Jung and M. J. Schnitzer, “Multiphoton endoscopy”, *Opt. Lett.* **28**(11), pp. 902–904, (2003).
- [15] W. Göbel, J. N. D. Kerr, A. Nimmerjahn, and F. Helmchen, “Miniaturized two-photon microscope based on a flexible coherent fiber bundle and a gradient-index lens objective”, *Opt. Lett.* **29**(21), pp. 2521–2523, (2004).
- [16] H. C. Stary, D. H. Blankenhorn, A. B. Chandler, S. Glagov, W. I. Jr., M. Richardson, M. E. Rosenfeld, S. A. Schaffer, C. J. Schwartz, W. D. Wagner, and R. W. Wissler, “A definition of the intima of human arteries and of its atherosclerosis-prone regions”, *Circulation* **85**(1), pp. 391–405, (1992).
- [17] H. C. Stary, A. B. Chandler, S. Glagov, J. R. Guyton, W. Insull, M. E. Rosenfeld, S. A. Schaffer, C. J. Schwartz, W. D. Wagner, and R. W. Wissler, “A definition of initial, fatty streak, and intermediate lesions of atherosclerosis”, *Arteriosclerosis and Thrombosis* **14**(5), pp. 840–856, (1994).
- [18] H. C. Stary, A. B. Chandler, R. E. Dinsmore, V. Fuster, S. Glagov, W. I. Jr., M. E. Rosenfeld, C. J. Schwartz, W. D. Wagner, and R. W. Wissler, “A definition of advanced types of atherosclerotic lesions and a histological classification of atherosclerosis”, *Circulation* **92**, pp. 1355–1374, (1995).
- [19] W. R. Zipfel, R. M. Williams, R. Christie, A. Y. Nikitin, B. T. Hyman, and W. W. Webb, “Live tissue intrinsic emission microscopy using multiphoton-excited native fluorescence and second harmonic generation”, *PNAS* **100**(12), pp. 7075–7080, (2003).
- [20] A. Zoumi, X. Lu, G. S. Kassab, and B. J. Tromberg, “Imaging coronary artery microstructure using second-harmonic and two-photon fluorescence microscopy”, *Biophysical journal* **87**(4), pp. 2778–2786, (2004).
- [21] M. van Zandvoort, W. Engels, K. Douma, L. Beckers, M. oude Egbrink, M. Daemen, and D. W. Slaaf, “Two-photon microscopy for imaging of the (atherosclerotic) vascular wall: A proof of concept study”, *Journal of Vascular Research* **41**(1), pp. 54–63, (2004).
- [22] D. H. Blankenhorn and H. Braunstein, “Carotenoids in man. iii. the microscopic pattern of fluorescence in atheromas and its relation to their growth”, *Journal of Clinical Investigation* **37**, pp. 160–165, (1958).
- [23] K. Arakawa, K. Isoda, I. Toshimitu, K. Nakajima, T. Shibuya, and F. Ohsuzu, “Fluorescence analysis of biochemical constituents identifies atherosclerotic plaque with a thin fibrous cap”, *Arterioscler. Thromb. Vasc. Biol.* **1**, pp. 1–71, (2002).
- [24] M. Keijzer, R. Richards-Kortum, S. L. Jacques, and M. S. Feld, “Fluorescence spectroscopy of turbid media: Autofluorescence of the human aorta”, *Appl. Opt.* **28**, pp. 4286–4292, (1989).

Material	Thermal conductivity, κ (W/m·K)	Specific heat, c_p (J/kg·K)	Density, ρ (kg/m ³)
Tissue	0.4	4000	1000
Glass	0.8	800	2600

Table 1: Thermal properties used in the FEM model

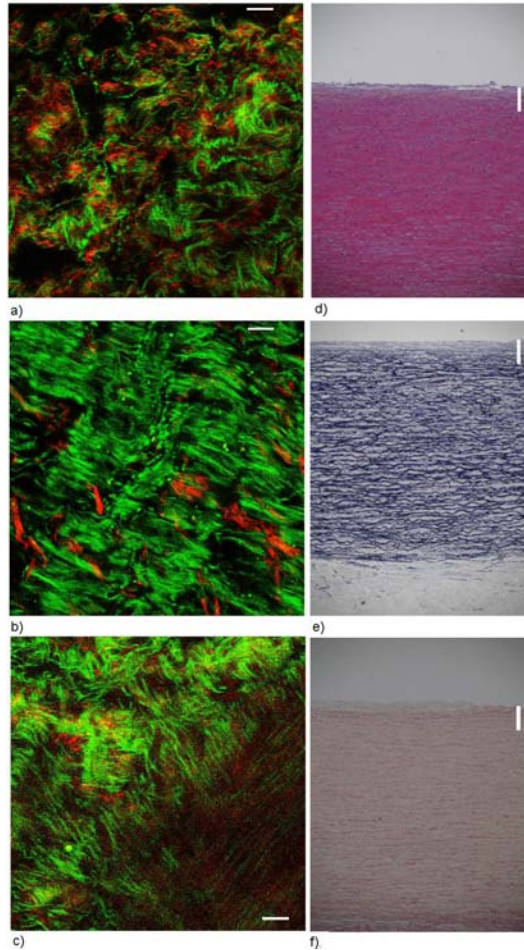


Figure 1: MPM images of normal vessel in the x, y plane (green is TPEF and red SHG) and corresponding histological images in the x, z plane. a) Normal vessel at the surface. There is a thin layer of elastic fibers over a layer of thin, wavy collagen fibers. The dark areas are regions where the wavy surface is below the image plane. b) A dense layer of relatively thick, ordered elastic fibers, was usually seen below the layers of thinner elastic fibers at the surface. Thick, randomly oriented collagen fibers can be seen in between. c) Image taken about 20 microns below the surface. Several layers can be seen since they are at an angle to the image plane. The deepest structure is oriented 90° to the layer above. Figures d-f show histological sections of normal aorta at 10x. d) HES stain. e) Elastica stain where the elastica laminae can clearly be seen. f) Van Gieson stain. Connective fibers are stained red. Bars are $20 \mu\text{m}$ in the MPM images and $200 \mu\text{m}$ in the histology images.

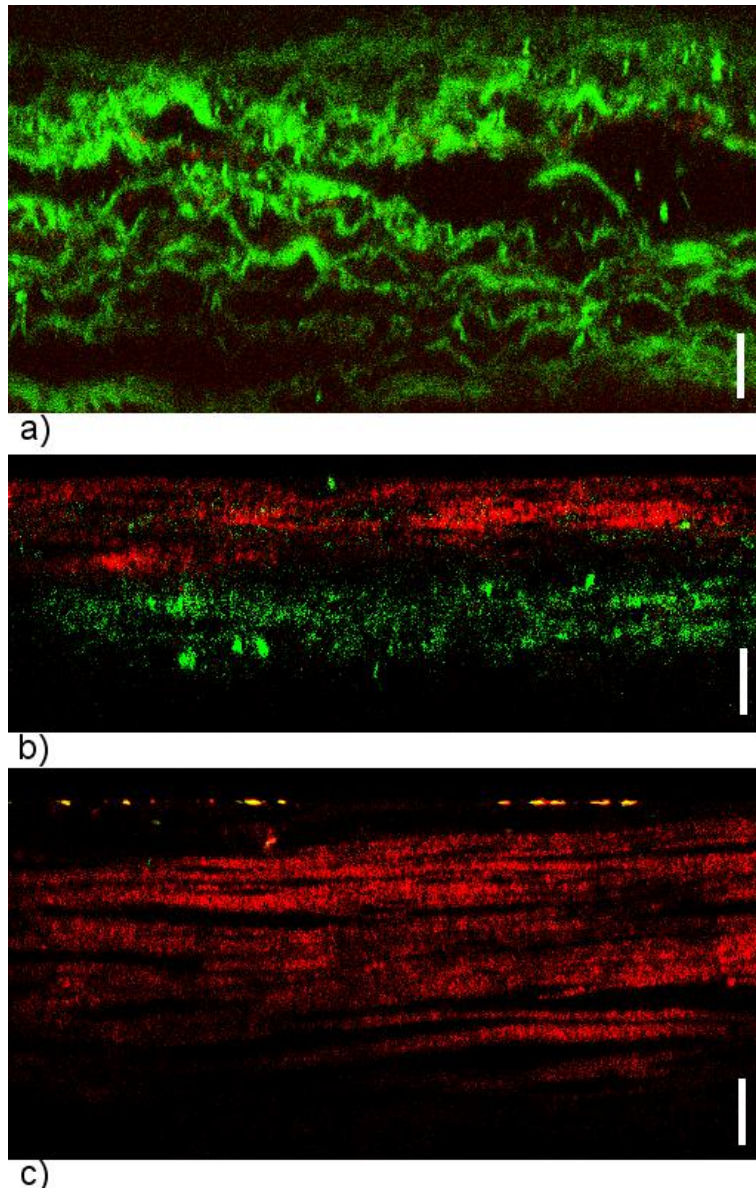
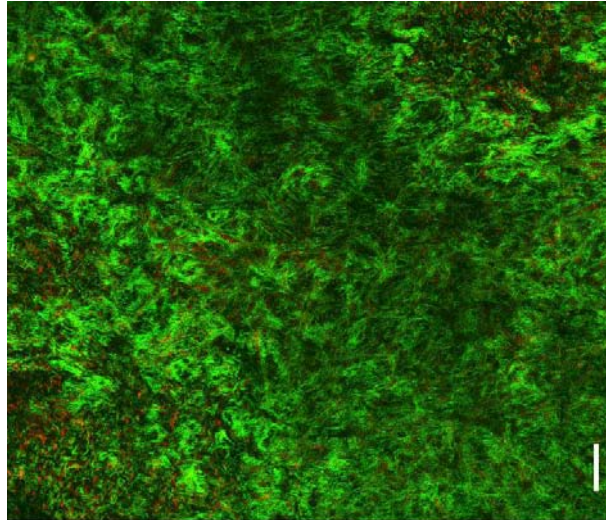
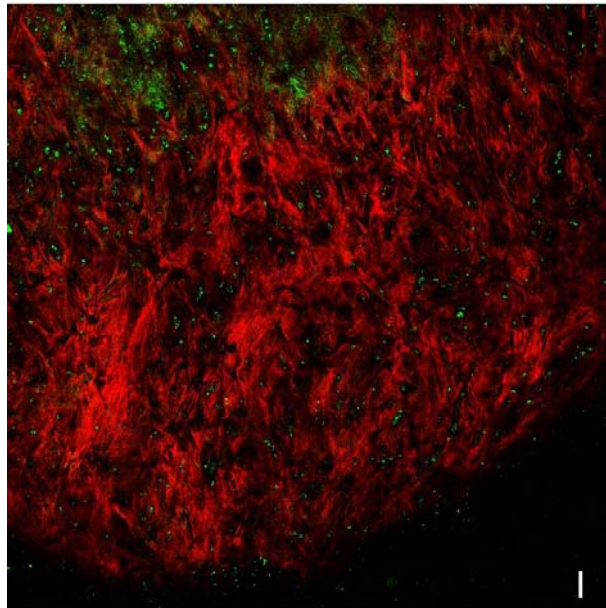


Figure 2: Cross sectional images (x, z plane). Green is TPEF and red is SHG. a) The elastic laminae of a normal aorta can clearly be seen. b) An early lesion. Layers of collagen about $20 \mu\text{m}$ thick over elastic laminae. c) Cross section of a thick fibrous cap. The horizontal fluorescent points in the top is at the surface of the coverglass. Collagen layers can be seen down to a depth of about $60 \mu\text{m}$. Bars are $20 \mu\text{m}$.



a)



b)

Figure 3: These images show the structure of the fibrous networks at a larger scale than the previous images, covering an area of 2.3 x 2.3 mm. Green is TPEF and red is SHG a) Normal aorta. Notice the scattered collagen fibers in the dense elastin network. b) Atherosclerotic plaque. Notice the clusters of small fluorescent objects, clustered in the spaces between the fibers. Bars are 100 μm .

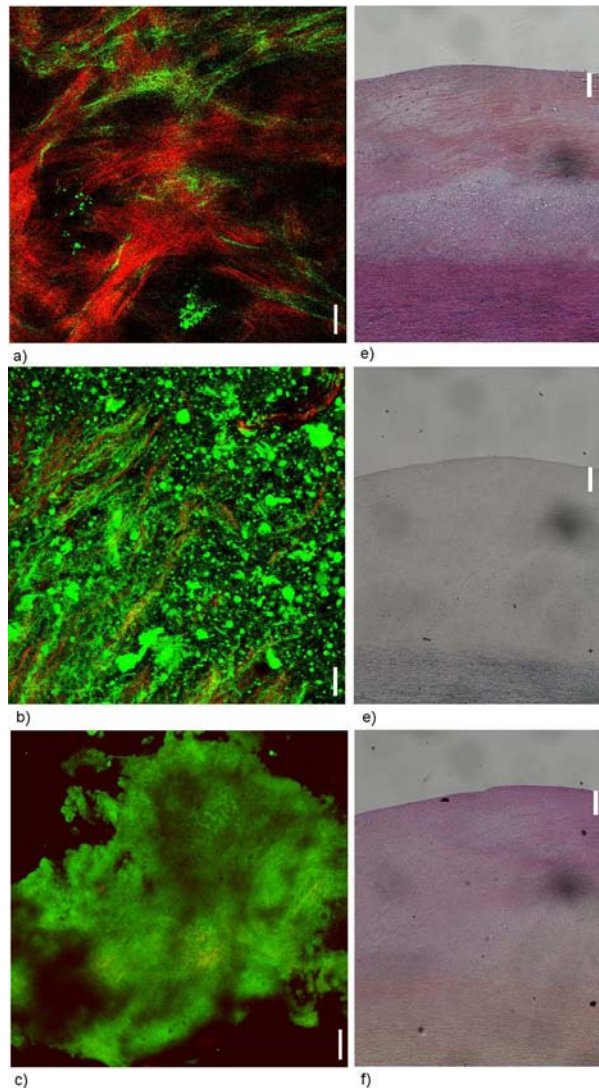


Figure 4: a) The cap of a thick fibroatheroma showing bundles of collagen fibers. Also notice the small fluorescent objects of unknown origin that might be autofluorescence from lipid deposits or cellular structures. b) The inside of an atherosclerotic plaque. A large amount of fluorescent objects was seen that might be attributable to lipid droplets within the necrotic core. Also, some collagen fibers can be seen. The gain could not be adjusted separately for the SHG and TPEF signals, so that to get adequate SHG signal, some of the autofluorescens saturated. c) Calcified plaques showed strong non-fibrillar autofluorescence. Some SHG can be seen that seems to emanate from within the calcification. d-e) Histology of a fibroatheroma. d) HES stain. e) Elastica stain, showing no elastic fibers within the plaque. f) Van Gieson stain, where the red indicates the connective tissue within the cap. Bar is 20 μm in the MPM images and 200 μm in the histology images.

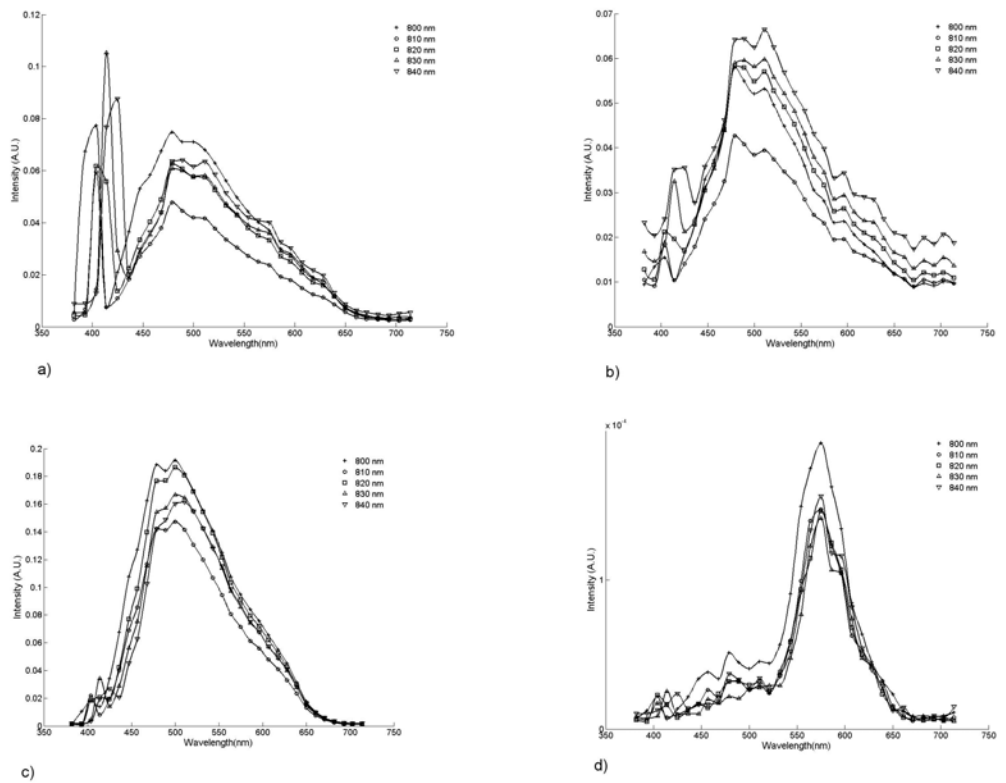


Figure 5: Emission spectra for various tissue components, measured with different excitation wavelengths. a) Collagen. b) Elastin. c) Calcification. d) Fluorescent object within the fibrous cap of a plaque.

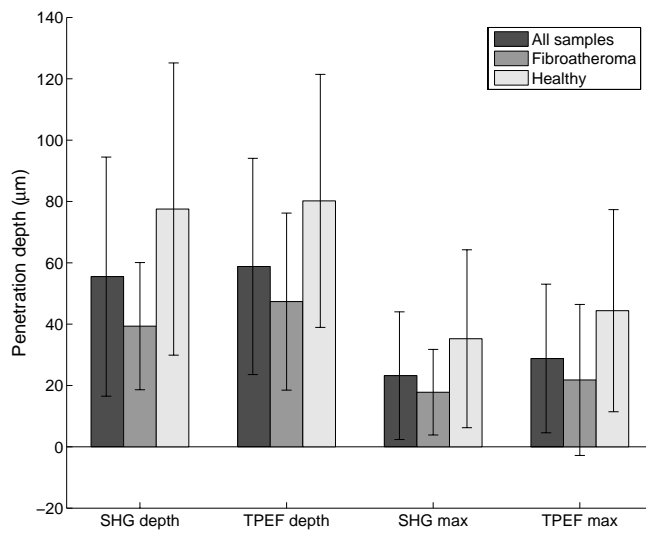
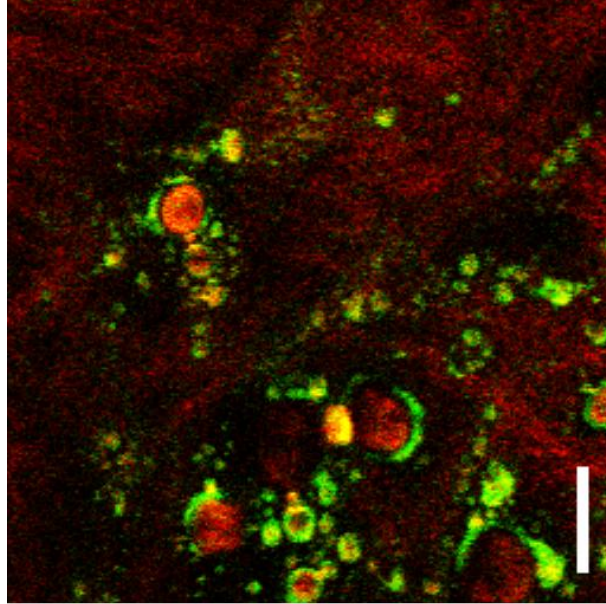
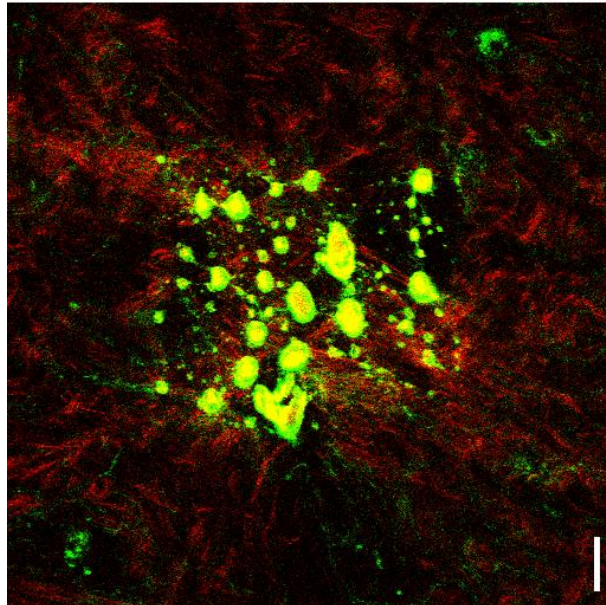


Figure 6: The mean of the penetration depth defined as the point where the signal had fallen to e^{-1} of the maximum value, and the mean of the depth where the maximum signal was found, for various vessel states. It is the difference between these two that defines the penetration depth in the sense of signal decay due to scattering and absorption. The first value indicates how deep we were able to see structures with the current experimental setup. The error bars represent the standard deviation.



a)



b)

Figure 7: a) Bubble formation in the tissue during the bleaching/heating procedure. Image is $115 \times 115 \mu\text{m}$ b) Image taken 30 minutes after heating of tissue, indicating that the damage incurred is irreversible and confined to the illuminated region. Image is $230 \times 230 \mu\text{m}$.

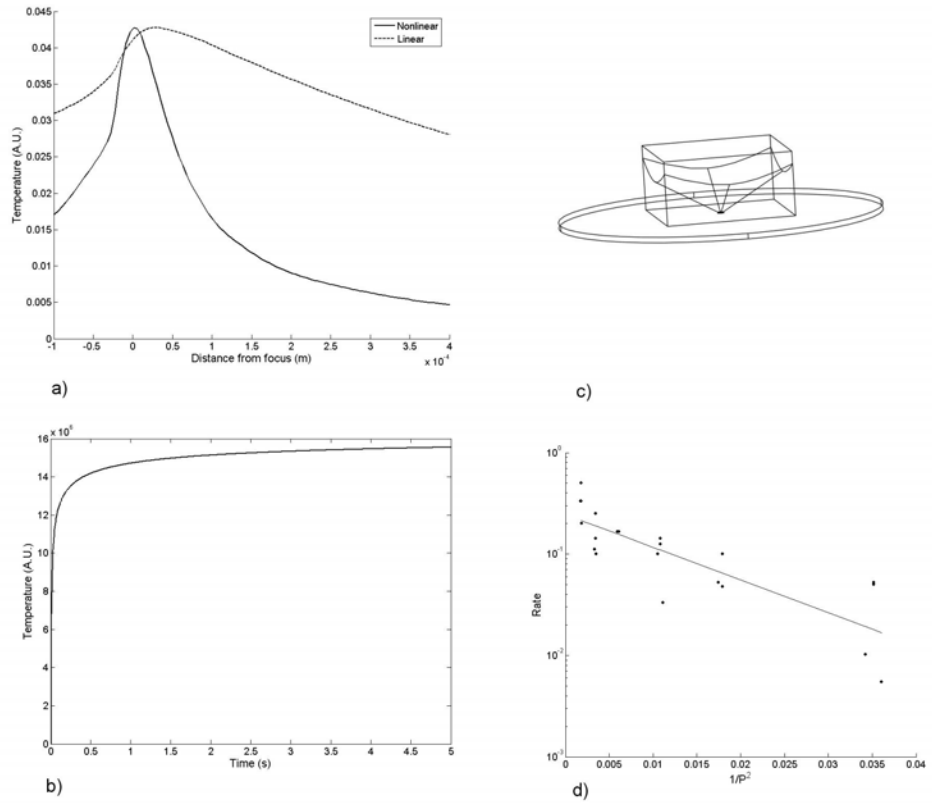


Figure 8: a) Temperature close to focus calculated by finite element method. Since the thermal changes in the tissue were localized to about 15-20 μm the thermal shape of the nonlinear absorption better describes this observed effect. Also notice the maximum for the linear absorption is displaced from the focus. Since the beam is scanned over an area that is much larger than the focus, the area scanned by the beam only increases significantly after the cone of the beam has become on the order of the scanned area. b) Time dependence of the temperature at the focus, calculated with the finite element model, with nonlinear absorption causing the heating. It is clear that the temperature is very close to the steady state value after only one second. However, bubble formation was at low excitation power first observed at times of around 40 s. This indicates that there is a significant time delay between the observed phenomena (bubbles) and the onset of steady state temperature. c) Geometry used in the FEM simulation. The disk represents the coverglass, the box is the tissue sample and the cone inscribed in the box defines the area with heat generation. d) An Arrhenius plot where the rate is defined as the inverse of the time of bubble formation and the temperature is assumed to be proportional to the square of the excitation power.

